Submolecular imaging with single particle atomic force sensors

Georgy Kichin

JÜLICH
FORSCHUNGSZENTRUM

Submolecular imaging with single particle atomic force sensors

Von der Fakultät für Mathematik, Informatik und Naturwissenschaften der
RWTH Aachen University zur Erlangung des akademischen Grades eines
Doktors der Naturwissenschaften genehmigte Dissertation

vorgelegt von
Master of Science in angewandten Mathematik und Physik

Kichin Georgy

aus Moskau, Russland

Berichter: Universitätsprofessor Dr. F. S. Tautz
Universitätsprofessor Dr. A. Gross

Tag der mündlichen Prüfung: 2. Juni 2014

Diese Dissertation ist auf den Internetseiten der Hochschulbibliothek online
verfügbar.

Submolecular imaging with single particle atomic force sensors

Georgy Kichin

Abstract

Scanning probe methods with decorated tips is a new trend in surface study. An application of complex probe like a tip with an attached single molecule or single atom allows to get new details about the surface properties. It has been shown that the scanning tunnelling hydrogen microscopy (STHM) approach can reach atomic scale resolution and reveals intermolecular interactions. Because of the complexity, this new rapidly developing area is not yet fully understood.

In this work systematic studies of tips decorated with Xe, H_2, D_2, CO, CH_4 was carried out. The tip with a single atom or a single molecule creates a single particle sensor that simultaneously performs the function of an atomic-scale force sensor and a signal transducer, which couples the short-range force acting on the tip to the tunnelling conductance of the junction. In some cases the sensor-transducer function of the decorated STM tips can be quantitatively calibrated. Differences in the performance of the studied sensors suggest that the sensor functionality can be modified by tuning the interaction between the sensor particle and the STM tip. Based on force-field calculations, theoretical analysis of the single particle sensor shows an interrelation between the relative movement of the particle on the tip and contrast structure of the surface images.

Kurzfassung

Der Einsatz von Rastersondenmethoden mit funktionalisierten Spitzen ist ein neuer Trend in der Oberflächen Physik. Eine Anwendung der komplexen Sonde aus einer Spitze mit einem einzelnen adsorbierten Molekül oder Atom erlaubt es, neue Details über die Oberflächeneigenschaften zu erhalten. Es wurde gezeigt, dass mit dem Rastertunnelwasserstoffmikroskopie (STHM) Ansatz eine Auflösung auf atomarer Skala erzielt werden und intermolekularen Wechselwirkungen sichtbar gemacht werden können. Auf Grund der hohen Komplexität ist dieses neue, sich rasch entwickelnde Gebiet noch nicht vollständig verstanden.

In dieser Arbeit wurden systematische Untersuchungen von mit Xe, H_2, D_2, CO und CH_4 besetzten Spitzen durchgeführt. Die Spitze mit einem einzelnen Atom oder Molekül stellt einen Einteilchen-Sensor dar, der gleichzeitig als atomarer Kraftsensor und Signalwandler fungiert und so die kurzreichweitigen Kräfte, die an der Spitze wirken, mit der Tunnelleitfähigkeit des Kontaktes koppelt. In einigen Fällen kann die Sensor-Signalwandlerfunktion der dekorierten STM-Spitzen für eine quantitative Kalibration genutzt werden. Die Unterschiede im Verhalten der untersuchten Sensoren zeigen, dass die Sensorfunktionalität durch die Wechselwirkung zwischen Sensorteilchen und STM-Spitze modifiziert werden kann. Auf der Grundlage von Kraftfeldberechnungen zeigt eine theoretische Analyse der einzelnen Sensorteilchen eine Wechselbeziehung zwischen der relativen Bewegung des Teilchens auf der Spitze und Kontraststruktur der Oberflächenbilder.

Contents

List of Acronyms

AFM – Atomic force microscopy

CFM - chemical force microscopy

CuPc - copper phthalocyanine

DFT – Density functional theory

DOS – Density of states

DSP – Digital signal processor

ECSTM - electrochemical scanning tunnelling microscope

EELS – Electron energy loss spectroscopy

EFM - electrostatic force microscopy

FM-AFM – Frequency modulated atomic force microscopy

GXPS – X-ray photoelectron spectroscopy

GIXD - Grazing Incidence X-ray Diffraction

GIXRD - Grazing Incidence X-ray Diffraction

IETS – Inelastic electron tunnelling spectroscopy

KPFM - Kelvin probe force microscopy

LDA – Local density approximation

LDOS – Local density of states

LEED – Low energy electron diffraction

LEEM – Low energy electron microscopy

MFM - magnetic force microscopy

ML - monolayer

NC-AFM – Non-contact atomic force microscopy

NSOM (or SNOM) - near-field scanning optical microscopy

OLED - organic light emitting diode

OTFT - organic thin-film transistor

OPV - organic photovoltaic device

PEEM – Photo electron energy microscopy

PTCDA – 3,4,9,10 perylene tetracarboxylic dianhydride

RHEED – Reflection high energy electron diffraction

SEM – Scanning electron microscopy

SnPc – Tin-II-phthalocyanine

SPSM - spin polarized scanning tunnelling microscopy

STHM – Scanning tunnelling hydrogen microscopy

STM – Scanning tunnelling microscopy

STS – Scanning tunnelling spectroscopy

TED – Total electron density

TEM – Transmission electron microscopy

TLS - two levels system

TPD – Temperature dependent desorption

UHV – Ultra high vacuum

UPS – Ultraviolet photoelectron spectroscopy

XPS – X-ray photoelectron spectroscopy

XSW – X-ray standing wave

Introduction

The interest to the study of interfaces has increased significantly in recent years. This happens thanks to the successes in organic electronics that demonstrates the great potential for constructing electronic devices, such as high-efficiency organic light emitting diodes (OLEDs) [1–9], organic photovoltaic devices (OPVs) [10–12], biosensors [13, 14], solar cells [15, 16], cheap thin-film transistors (OTFTs) [17–24]. It starts to become possible to produce in a cheap, compact way electronic devices based on thin organic films. Organic electronics deals with carbon based semiconductors in a form of small organic molecules and conjugated polymers. Carbon based π-conjugated electronic systems are able to access the full range of electric properties, from insulators to metals [25], and can be widely used in electronics along with traditional copper and silicon [26]. In such case analysis methods of interfaces and individual organic molecules are highly important for both the further advances in device design, usability and also for fundamental research.

In general, methods of surface analysis can be divided in two large groups [27]. The first group contains diffraction methods. This set of methods is used for surface analysis in reciprocal space. Methods like low electron energy diffraction (LEED) [28–31], X-ray diffraction (XRD) [32, 33] and grazing incidence X-ray diffraction (GIXD or GIXRD) [34–39] are widely used for structural analysis and crystal growth control. These methods are especially successful for studying of ordered structures, but are not useful for an analysis of local features like defects or contacts.

Another large group includes methods of real space structure study. There are great of variety of different techniques that can be classified as one of three basic types: optical, charged particle (electron and ion) and scanning probe microscopy.

Optical methods are mainly used in biology because they are safe for biological objects and do not destroy them during the measurements. The

resolution of optical methods is quite low. For profound surface analysis it is usually not enough.

Much higher resolution can be obtained employing electrons instead photons. It is possible since an electron has wave-like properties and its wavelength is about several orders of magnitude shorter than visible light wavelength. Photoelectron emission microscopy (PEEM or PEM) is employed to study thin film growth in a real time [40, 41]. PEEM is usually combined with Low Energy Electron Microscope (LEEM). LEEM belongs to the electron method of surface analysis where the image is formed by elastically backscattered electrons from the surface. Pair PEEM/LEEM is used usually for studying dynamic processes on the surfaces, such as film grows, adsorption or phase transition [42–44].

Scanning Electron Microscopy (SEM) and Transmission electron microscopy (TEM) are widely used for studying the physical properties of the thin films. SEM is mainly used for analysis of a surface topography and composition [45, 46]. TEM is used for studying the interfaces [47, 48], and the structural and dynamic properties of the thin films [49, 50]. SEM resolution is $1 - 20$ nm, and TEM resolution reaches 0.05 nm [51]. An advantage of TEM is, that it is capable to get not only an image of the surface, but also diffraction patterns for the same region of the surface. TEM images reflect the periodicity of the crystal lattice since the lattice acts as a phase grating. The interpretation of the images obtained with TEM can be complicated, because it depends on the sample thickness, objective lens defocus and interference effects. However, none of these methods can be used for organic thin film study because high energy electrons are capable to destroy the organic samples. TEM and SEM are widely used in industrial application, where the resolution of tens and hundreds nm is usually required.

The last large group of surface analysis methods includes scanning probe microscopy (SPM) techniques. SPM methods are based on the interaction between a probe and a surface of a sample. With the probe that is usually sharp tip, it is possible not only to investigate the electronic structure with a subangstrom precision but also measure forces [52], surface conductivity [53, 54], static charge distribution [55–57], local magnetic fields [58, 59] and friction [60] or modulus of elasticity [61–63]. A big advantage of SPM is the additional possibility to manipulate the molecules on the surfaces [64–67].

The two most widely used SPM methods are the scanning tunnelling microscopy (STM) and the atomic force microscopy (AFM). Historically STM was first. AFM was built shortly after, applying underlying principles of STM for force measuring. Due to the simple construction and ability to

resolve single atoms, SPM is used in a wide variety of disciplines.

SPM group grows quite fast and new methods arise continuously. Scanning probe techniques are graded and named after the type of interaction detection of probe: force detection (chemical force microscopy (CFM) [68], electrostatic force microscopy (EFM) [69], magnetic force microscopy (MFM) [70]), tunnelling current detection (ECSTM electrochemical scanning tunnelling microscope [71], KPFM, kelvin probe force microscopy [72], SPSM spin polarized scanning tunnelling microscopy [73]), photon detection (near-field scanning optical microscopy (NSOM or SNOM) [74, 75]). And this is not the full list.

No SPM technology can define the type and the structure of an atom or a molecule without any additional information. Chemical analysis of the molecules is based on spectroscopic studies or on increasing the STM resolution to enable direct determination of the chemical structure. Spectroscopy methods are used for probing electronic states (inelastic electron tunnelling spectroscopy (IEST) [76], tip-enhanced Raman spectroscopy (TERS) [77], or electro-luminescence spectroscopy (ELS) [78]). Information to restore the structure of molecules is obtained from the combination of the information obtained from images and spectra. However, the analysis is complicated because spectra are strongly affected by a local interaction with a surface.

The steps to improve SPM resolution has been made recently. They included application of tip decorated with a single molecule. AFM sensor terminated with CO showed a map associated with the chemical structure of complex organic molecules. Pentacene, placed on a dielectric layer to decouple it from the metal surface, was used for experiment [79].

Another research has shown that the resolution can be improved using the STM tip terminated with H_2 or D_2. The resulting image contrast resemble the structure formula of the molecules [80]. This approach was called scanning tunnelling hydrogen microscopy (STHM). The mechanism that is behind the contrast formation is still studied. The advantage of this method is the ability to observe submolecular structural form of large organic molecules with very little effort.

The thesis is organized as follows:

In **chapter 1** a brief overview of some theoretical principles of STM and AFM techniques used in this study is given.

In **chapter 2** experiment preparation procedure is given.

In **chapter 3** is discussed what gases other than hydrogen or deuterium

can be used to achieve the STHM-like resolution. Discussion is based on results of the experiment. The results of this chapter have been published in paper: G. Kichin, C. Weiss, C. Wagner, F. S. Tautz, R. Temirov. Single Molecule and Single Atom Sensors for Atomic Resolution Imaging of Chemically Complex Surfaces. *Journal of the American chemical society*, 133:16847-16851, 2011.

In **chapter 4** the experiment where force and conductance are measured simultaneously is described. Discussion shows possible relation between force and conductance of the tip junction with atom or molecule. The results of this chapter have been published in paper: G. Kichin, C. Wagner, F. S. Tautz, R.Temirov. Calibrating atomic-scale force sensors installed at the tip apex of a scanning tunneling microscope. *Physical review B*, 87:081408, 2013.

In **chapter 5** is described the experiment about excitation of D_2 from the junction. The experiment results are compared with force field calculations. The mechanism of STHM image formation is discussed.

Chapter 1

Theory of measurements

1.1 STM

The STM is one of the main instruments for the surface analysis with subangstrom resolution. It was invented by Binnig and Rohrer in 1981 [81]. Due to the relative simplicity of the STM equipment, it is one of the main tool for studies of the conductive surfaces with a subangstrom resolution under different experimental conditions, e.g. in solutions [82–84] at high pressures [85, 86], high vacuum [87] in a wide temperature range from hundreds of Kelvins [85] down to millikelvin [88].

Despite a large variety of STM applications, the basic principles of the technique remain the same and are based on the concept of quantum tunnelling. Electron moves from one classically allowed region to another one through a potential barrier, a region where the electron is classically forbidden to exists. One allowed region is in the tip, other one is in the surface. A barrier in the STM junction is due to a small gap between the tip and the surface in the electric circuit. Electrons flowing through the junction tunnel through the barrier (see Fig. 1.1).

Tunnelling of the electrons is a quantum mechanical phenomenon that cannot be described with a classical mechanics. Electrons behave as a particle and a wave and their motion can be described with Schrödinger equation. In the presence of potential $U(z)$, assuming 1D case, the energy levels of the electrons are given by the single-particle Schrödinger equation,

$$-\frac{\hbar^2}{2m}\frac{\partial^2\psi(z)}{\partial z^2} + U(z)\psi(z) = E\psi(z). \qquad (1.1)$$
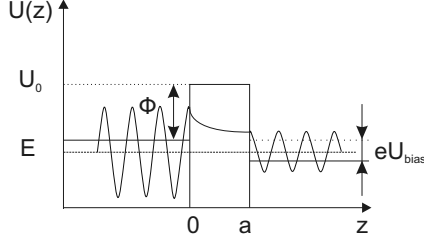
Figure 1.1: Quantum tunnelling through a 1D rectangular potential barrier.

The solution of the Schrödinger equation has a form

$$\psi(z) = \psi(0)e^{\pm ikz}, \tag{1.2}$$

where

$$k = \frac{\sqrt{2m(E - U(z))}}{\hbar}, \tag{1.3}$$

$\hbar$ is the Planck's constant, E is the energy of the electron, m is the mass of electron. For tunnelling through the simple rectangular potential barrier with parameters $U(x) = U_0$ and a (see Fig.1.1) the solution has a form

$$
\begin{aligned}
\psi_I &= A_1 \exp(i\kappa z) + B_1 \exp(-i\kappa z), \text{ for } z < 0, \\
\psi_{II} &= A_2 \exp(-\chi z) + B_2 \exp(\chi z), \text{ for } 0 < z < a, \\
\psi_{III} &= A_3 \exp(i\kappa(z - a)) + B_3 \exp(-i\kappa(z - a)), \text{ for } z > a, \quad (1.4)
\end{aligned}
$$

where

$$\chi = \frac{\sqrt{2m(U_0 - E)}}{\hbar} \text{ and } \kappa = \frac{\sqrt{2mE}}{\hbar}. \tag{1.5}$$

The coefficient B_3 is 0 for the tunnelling regime because the reflected wave is absent. The current is proportional to the particle flow j, which is described as

$$j = \frac{i\hbar}{2m}\left(\frac{\partial \psi^*}{\partial x}\psi - \frac{\partial \psi}{\partial x}\psi^*\right). \tag{1.6}$$

Equation (1.4) can be exactly solved. In the case of a large barrier $U >> E$ the transition coefficient is given by

$$D = \left|\frac{j_{III}}{j_I}\right| = \left|\frac{A_3}{A_1}\right|^2 \cong D_0 \exp\left(-\frac{2}{\hbar}\int\limits_0^a \sqrt{2m(U(z) - E)}dz\right). \tag{1.7}$$

In the 1D case the current I depends exponentially on the barrier thickness a:

$$I = I_0 e^{-2\chi a}. \tag{1.8}$$

Generally, χ is a function of the barrier height. The 1D case is valid only for planar electrodes but it shows an important result. An exponential behaviour is the key mechanism that produces high vertical resolution and allows imaging the surfaces. To solve the Schrödinger equation in 3D case, geometrical and electronic properties of the tip and the surface are required to be know.

1.1.1 Bardeen approach

The next important step in the tunnelling theory was made by Bardeen [89]. Instead of solving the Schrödinger equation for the complete system (two electrodes and junction), he suggested to divide the system into subsystems and solve the Schrödinger equation for each of the subsystems (the first and the second electrode) to find states in the different subsystems (different electrodes). In this case the tunnelling current will be a sum of tunnellings of the electrons from all the states of one electrode to the states of other electrode. The rate of the transferring electrons M can be calculated using the time-depending perturbation theory. Bardeen showed that the amplitude of the electron transfer is determined by the overlap of the wave functions of the two subsystems of the two separated electrode surfaces:

$$M = \frac{\hbar}{2m} \int_{z=z_0} \left(\chi^* \frac{\partial \psi}{\partial z} - \psi \frac{\partial \chi^*}{\partial z} \right) dS, \tag{1.9}$$

where ψ and χ are the wave functions of the two surface-electrodes. The integral is over the separating surface between the two electrodes. The rate of electron transfer is determined by the Fermi golden Rule

$$w = \frac{2\pi}{\hbar} |M|^2 \delta(E_\psi - E_\chi), \tag{1.10}$$

where E_ϕ and E_χ are eigenenergies for the states ψ and χ. Then the tunnelling current can be evaluated as

$$\begin{aligned} I &= \frac{4\pi e}{\hbar} \int_{-\infty}^{\infty} [f(E_f - eV + \epsilon) - f(E_f + \epsilon)] \times \\ &\quad \rho_s(E_f - eV + \epsilon)\rho_t(E_f + \epsilon)|M|^2 d\epsilon, \end{aligned} \tag{1.11}$$

$f(E)^{-1} = 1 + \exp[(E - E_f)/k_B T]$ is the Fermi distribution function and ρ_s and ρ_t are the density of states (DOS) of two electrodes.

If $k_\mathrm{B}T$ is smaller than the energy resolution required in the experiment, then the integration limits can be substituted $\int\limits_{-\infty}^{\infty} \to \int\limits_{eV_\mathrm{bias}}^{0}$. Bardeen assumed that $|M|$ does not change in interval (0, eV_bias) and thus,

$$I \propto \int_0^{eV} \rho_\mathrm{s}(E_\mathrm{f} - eV + \varepsilon)\rho_\mathrm{t}(E_\mathrm{f} + \varepsilon)d\varepsilon. \qquad (1.12)$$

The tunnelling current is proportional to the overlapping of DOSs of two electrodes.

1.1.2 Tersoff-Hamann theory
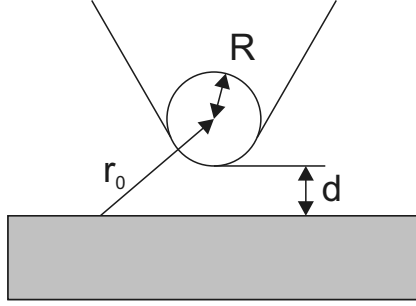
Figure 1.2: STM junction geometry in the Tersoff–Hamann model.

Tersoff and Hamann made the next step in the theory of STM [90, 91]. Taking into account Bardeen's approach, they developed a simple tunnelling theory for a 3D junction. The tip was assumed locally spherical and the electronic wavefunctions of the tip are modelled radially symmetric (see Fig. 1.2). The spherical geometry refers to the s-orbital and, therefore, Tersoff-Hamann theory is called often s-wave model. If the applied bias is much smaller than the work function of an electron in the sample and the temperature is low then the current can be represented as

$$I \sim U\rho_t(E_\mathrm{f})\rho_s(r_0, E_\mathrm{f})\exp(2\kappa R), \qquad (1.13)$$

where ρ_t is tip's DOS at the Fermi level, ρ_s is local DOS (LDOS) of the surface at the Fermi level in the position r_0 of the tip, R is radius of the tip. If the DOS of the tip does not depend on its position and the bias is kept constant, then the STM constant-current image reflects the properties

of the sample only, the LDOS. This model works well for the metallic and conducting samples.

The Tersoff-Hamann theory gives a simple interpretation of scanned images. The equation for current reproduces the Ohm's low on atomic level: $I \sim U$. The tunnelling current exponentially depends on the distance:

$$I \propto \int_0^{eV} \rho_{\mathrm{s}}(E_{\mathrm{f}} - eV + \varepsilon)\rho_{\mathrm{t}}(E_{\mathrm{f}} + \varepsilon)d\varepsilon, \qquad (1.14)$$

and

$$\rho_{\mathrm{s}}(E_{\mathrm{f}}, r_0) = \rho_{\mathrm{s}}(E_{\mathrm{f}}) \exp(-\chi(d + R)), \qquad (1.15)$$

for DOS of the sample

$$I \propto \int_0^{eV} \rho_{\mathrm{s}}(E_{\mathrm{f}} - eV + \varepsilon)\rho_{\mathrm{t}}(E_{\mathrm{f}} + \varepsilon)T(E_{\mathrm{f}} + \varepsilon, V)d\varepsilon, \qquad (1.16)$$

where $T(E, V) = \exp(-2d\chi)$ is a transmission coefficient. Not all electrons are involved equally in the tunnelling process.

However, Tersoff-Hamann approach is not universal. It does not work for semiconductors. For the study of semiconductors, high voltage is needed in a range of several volts, which is comparable to the work functions for the electrons. Thus, not only the electrons near Fermi level are involved in the tunnelling.

The tips used in experiments usually are made of tungsten and PtIr. These tips are not s-shaped. The tunnelling happens through the p-orbital. This problem was solved introducing the derivative rule [92] to take other than s-shaped orbitals into account [93].

1.1.3   Scanning Tunnelling Spectroscopy

Scanning Tunnelling Spectroscopy (STS) is an extension of the STM technique, which is used to provide information about the density of electrons in a sample as a function of their energy. The tip is placed at a certain position above the surface and the bias voltage is swept in a range of interest while the response current is measured. The usual goal of the STS experiments is to probe the DOS distribution of the sample surface.

Using the equation (1.16), the differential conductance has form

$$\frac{dI}{dV}(V) = \frac{2e^2}{\hbar} \left(\rho_{\text{t}}(0)\rho_{\text{s}}(eV)T(eV, E) + \int_0^{eV} \rho_{\text{t}}(-eV + E)\rho_{\text{s}}(E)\frac{dT(V, E)}{dV}dE \right).$$
(1.17)

The differential conductance is proportional to the LDOS but with an additional term. The second term in Eq. 1.17 represents a non-linear background. This term can be set equal to zero if the transmission coefficient, T(E,V), does not depend on the bias V. In this case the current will be described by Eq. 1.12 and $\frac{dI}{dV} \propto \rho_{\text{s}}(E_{\text{f}} - eV + \varepsilon)$. This equation is widely used in spectroscopy.

1.1.4   STM microscope

The base scheme of STM is shown in Fig. 1.3. Controlling the tip position above the surface, the tunnelling current can be changed. The position of the tip over the sample is controlled by piezocrystals. The piezocrystals working mechanism is based on the reverse piezoeffect. Voltage applied to the crystal brings to the change in length of the crystal in a subangstrom range. The tip can be moved over the sample surface with a very high precision. The electric tunnelling current in a range of pico- or nanoampers emerges when bias V is applied between the tip and the surface. The tunnelling current is amplified to make it easier handling by the electronic devices.
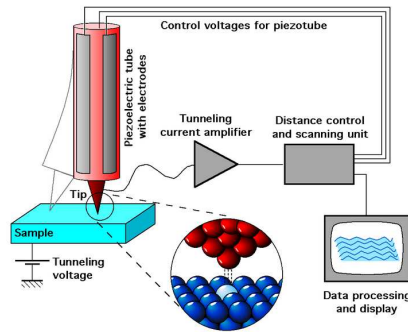

Figure 1.3: Schematic view of the STM setup. The picture is taken from Wikipedia.

STM can operate in two regimes: a constant current regime and a constant height regime. In the constant height regime the tip is moved above the surface at a constant distance and a variation of the current is recorded. In the constant-current regime the current is kept constant via variation of the tip-sample distance. In this case, the topography image is measured. The electric signal related to the z-displacement is recorded. The control over the tip movement is performed by the electronics and the computer.

1.2 IETS

Electrons passing the junction can interact with the media, e.g. molecule in the junction, the tip, the surface [94–96], and induce excitations of the localised vibrational modes [96]. If the energy of the electron eV is larger than $\hbar\omega$, where ω is the frequency of vibrational mode, then the electron can lose quantum of energy $E = \hbar\omega$ exciting this vibrational mode and tunnel into another empty state. This opens an additional inelastic tunnelling channel and changes the conductance σ of the junction. The usual change of the conductance $\Delta\sigma$ is quite small $\frac{\Delta\sigma}{\sigma} < 10\%$, what makes it hard to detect.
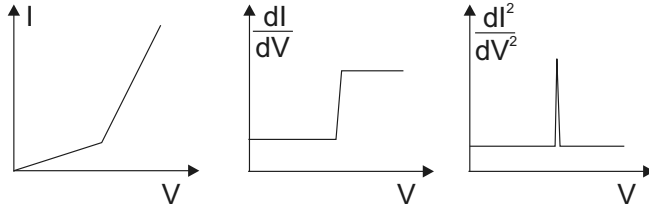
Figure 1.4: Opening of the inelastic tunnelling channel. A change of the slope is observed in the current I spectrum (a). A step is observed in the differentiate conductance dI/dV. The second derivative d^2I/dV^2 (c) has the peak-like feature.

For the passing electron energy below $\hbar\omega$, no inelastic tunnelling is possible. For the electron energy greater than $\hbar\omega$, an inelastic tunnelling channel opens. The current through the inelastic channel is proportional to the bias voltage. The current spectra show a change in the current curve slope after the channel is opened. In the conductance spectra, an opening of the inelastic tunnelling channel is observed like a step up (see Fig. 1.4). Consequently, in the d^2I/dV^2 spectra, a narrow peak is observed. The inelastic process is

independent to the polarity of applied bias and, therefore, is determined by
the excess of the electron energy only.
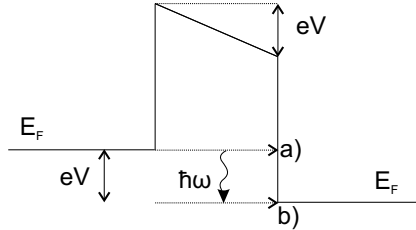
Figure 1.5: Two types of electron tunnelling. An elastic regime (a). The
energy of tunnelling electrons conserves. An inelastic regime (b), an inelastic
tunnelling with excitation of a vibrational level, $eV > \hbar\omega$. The energy of the
tunnelling electron changes.

The combined STM-IETS technique is used for an analysis of vibrational
properties of molecules with a atomic scale resolution. An advantage of the
STM-IETS over conventional IETS made in a planar junction is that this
technique allows performing vibrational spectroscopy on a single molecule.
The resonances are quite strong due to the good localization of the electron-
molecule interaction and the high current densities in the junction [97]. How-
ever, first experiments with the STM-IETS have demonstrated that the in-
terpretation of the obtained spectra is complicated. The selection rules are
different from rules of the traditional vibrational spectroscopy (IR, Raman,
HREELS). The theory of the single molecule vibrational spectroscopy devel-
oped by Lorente and Persson [98,99] have demonstrated that it is not possible
to extract the general set of STM-IETS selection rules. The opened inelastic
channel will always provide an additional tunnelling probability and increase
the conductance (see Fig. 1.5). But at the same time, the vibrational motion
of the molecule gets excited and the electronic orbitals participating in the
elastic tunnelling gets perturbed. This will strongly affect on the conduc-
tance. Unfortunately, these two processes cannot be separated.

1.3 AFM

AFM is another popular technique for studying the surfaces. It was in-
vented in 1986 by Gerd Binnig and Heinrich Rohrer [52]. AFM is based on
the design of STM. In AFM, the tip senses a force instead of the tunnelling

current. For the STM operation the surface should be conductive, while AFM measurements are tolerate to the surface conductance and, therefore, AFM starts to become so popular and widely used [100]. As well as the STM measurements, the AFM measurements can be performed under different experimental conditions, e.g. in various gases [52, 101], liquids [102–104], in vacuum [105], at low temperatures [106–109], at high temperatures [110, 111].

AFM can be used in several modes depending on tip-surface distance:

1. contact mode, AFM probe is in contact with the surface,

2. non-contact mode, AFM probe is not in contact with the surface,

3. mixed mode (or tapping mode).

Different forces act on the tip from the surface, e.g. long-range forces like electrostatic, magnetic, van der Waals, and short-range like chemical forces. The electrostatic forces can be compensated applying a potential to the tip. To avoid the magnetic force, a non-magnetic tip can be used. The main problem is that van der Waals forces cannot be avoided. To obtain atomic resolution, it is important to filter out long-range force contribution and to measure only force components that vary at the atomic scale.

The construction of the AFM sensor is complicated comparable to the STM sensor. The AFM sensor consists of a tip robustly glued to a cantilever. The tip interacts with the surface and transfers the interaction to the deformation of the cantilever. AFM can be operated either in a static or in a dynamic mode. In the static mode the cantilever is relaxed and the force is measured by monitoring the deflection of the cantilever. In this mode all forces contribute to the measured signal value. The dynamic mode is used to diminish the long-range force influence. In the dynamic mode the cantilever is oscillating above the surface with a fixed amplitude, while the frequency shift signal is monitored to obtain a surface image [112]. AFM that works in dynamic regime is called frequency-modulation AFM (FM-AFM). The resonant oscillation frequency is related to the force field between the tip and the sample and the corresponding frequency shift is related to the force gradient. The short-range forces have a stronger force gradient in the vicinity of the object of the study. Therefore, AFM is sensitive to the short-range forces in the dynamic mode at close tip-surface distances. When AFM is in the dynamic mode it gives better lateral resolution than in static mode, but can not measure force directly. Deconvolution methods are necessary to obtain the force.

The cantilever can be approximated as a harmonic oscillator. V_{ts} is the

potential between the tip and the surface. The tip-sample force will be given by $F_{\text{ts}}(z) = -dV_{\text{ts}}(z)/dz$ and the force gradient by $k_{\text{ts}}(z) = -dF_{\text{ts}}(z)/dz$. The actual resonance frequency, f, can be calculated from a equation of motion with an effective spring constant $k + k_{\text{ts}}$ and k is the spring constant of the cantilever,

$$f = \frac{1}{2\pi}\sqrt{\frac{k + k_{\text{ts}}}{m}}, \qquad (1.18)$$

where m is an effective mass. In case of $k_{\text{ts}} << k$, expanding the root, we will obtain

$$\frac{\Delta f}{f_0} = \frac{k_{\text{ts}}}{2k}, \qquad (1.19)$$

where $\Delta f = f - f_0$ is the frequency shift and f_0 is the eigenfrequency of the cantilever. Δf can be calculated using Hamilton-Jacobi approach if k_{ts} is not constant during a cycle:

$$\Delta f = \frac{f_0^2}{Ak}\int\limits_{1/f_0}^{0} F_{\text{ts}}[z(t), \dot{z}(t)]\cos(2\pi f_0 t)\,dt = -\frac{f_0}{kA^2}\langle F_{\text{ts}}z\rangle. \qquad (1.20)$$

The oscillation of the cantilever is described as $z(t) = A\cos(2\pi f_0 t)$, $\langle\rangle$ denotes time averaging over the period of the oscillation.

A good approximation for the force was proposed by Sader and Javis in [113]. Introducing $\Omega(t)$ as

$$\Omega(t) = \frac{\Delta f}{f_0} = -\frac{1}{\pi Ak}\int\limits_{1}^{-1} F(z + A(1+u))\frac{u}{\sqrt{1-u^2}}du, \qquad (1.21)$$

the relation between the force and the frequency shift will be

$$F(z) = 2k\int\limits_{\infty}^{z}\left(1 + \frac{A^{1/2}}{8\sqrt{\pi(t-z)}}\Omega(t)\right) - \frac{A^{3/2}}{\sqrt{2(t-z)}}\frac{d\Omega(t)}{dt}dt. \qquad (1.22)$$

This equation takes into account the magnitude of the oscillation amplitude and gives the force with an accuracy of 5%. For a small amplitude approximation the formula can be simplified to

$$F_{\text{ts,s}}(z) = 2\int_{z}^{\infty}d\tilde{z}\frac{k}{f_0}\Delta f(\tilde{z}) \qquad (1.23)$$

and for a large amplitude approximation

$$F_{\text{ts,l}}(z) = -\sqrt{2}kA^{3/2} \int\limits_{\infty}^{z} \frac{\Omega(t)}{dt} \frac{1}{\sqrt{t-z}} dt. \qquad (1.24)$$

The AFM sensor is sensible to the short-range forces in the dynamic mode if the amplitude of the cantilever oscillation is small. At the same time the long-range forces contribute little to the interaction. If the amplitude enlarges then the contribution of the long-range forces increases and can be greater than short-range force contribution. Thus, the resolution of the frequency shift measurements is limited by the large amplitude. The way how to get smaller and smaller resolution is to decrease the amplitude of the sensor. One of the ways to reduce the amplitude is to use a cantilever with a large stiffness ($k \approx 1$ kN/m).

1.4 AFM STM simultaneous measurements

The properties of AFM and STM are combined in a qPlus sensor [114–116]. With the qPlus sensor it is possible to measure simultaneously a tunnelling current and a change of a resonance frequency. From the frequency shift the value of the force gradient can be restored. The qPlus sensor construction is based on clock-quartz-type oscillator that has a fork-like shape. One prong is fixed to the holder, and the second is free. A tip is glued to the end of the free prong. Due to the high fork stiffness ≈ 1.8 kN/m, the fork oscillates with a high frequency $\approx 20 - 50$ kHz. The tuning fork is self sensing. It does not need additional equipment to measure the deflection of the cantilever. The deflection is proportional to the voltage difference between the prongs. This type of sensor is quite useful for low temperature measurements, where additional equipment can bring an unnecessary noise and heat into the system. Unfortunately, the fork oscillation affects the tunnelling current channel. To get the right values for force and current, Sader's approach can be applied [113, 117]. In small amplitude approximation the current coincide with the non-disturbed current.

1.5   Scanning tunnelling hydrogen microscopy

The scanning tunnelling hydrogen microscopy (STHM) was invented as a new method for the STM to obtain surface images with the "chemical" resolution. To get this resolution the molecular hydrogen is placed in the tunnelling junction. Then it is possible to determine directly the geometry structure of the surface by ultra-high resolution of the images. An example of an image with the STHM contrast of the PTCDA molecule is shown in Fig. 1.6(c). The hexagonal shape of the C_6 and C_5O rings is clearly visible. The image shows the conductance of the junction drops abruptly when the tip moves above the bonds. The imaginary lines that connect atoms are forming a pattern similar to the chemical formula of PTCDA Fig. 1.6(a). This type of contrast was named the geometrical contrast because it is related to the geometrical structure of the molecule. For the comparison, the high resolution image of a PTCDA molecule, scanned with a metal tip, shows LDOS-related contrast with no internal geometrical structure (Fig. 1.6(b)).
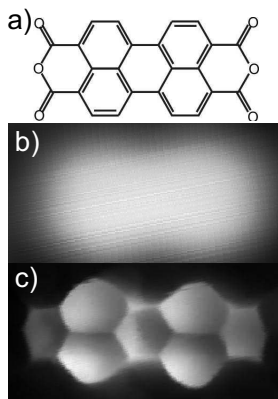
Figure 1.6: (a) Structural formula of the PTCDA molecule. (b) An STM image of PTCDA, the image is made with a clean tip. (c) An STM image of PTCDA. The image is made with a functionalized tip, geometrical structure of PTCDA is observed.

A first STHM experiment was described in paper of Temirov *et al.* [80]. The molecular hydrogen was dosed in the STM chamber at low pressure of $10^{-9} - 10^{-7}$ mbar. The STM working temperature was 5 K, what was below the condensation temperature of the molecular hydrogen. Molecular

hydrogen condenses on cold surfaces inside the STM chamber, including the crystal surface. To get the STHM contrast, the molecular hydrogen should be in the junction. The tip should move along the surface in the constant height regime. The STHM contrast is observed at a low bias voltage, of approximately from zero to tens of mV.

The precise amount of the hydrogen needed for experiment is unknown, because hydrogen is invisible with the STM. The amount of the hydrogen molecules on the surface was estimated indirectly by measuring the time of deposition. The STHM experiments show the unstable STHM contrast at low hydrogen coverage. Molecular hydrogen goes easily out of the junction and the initial STM contrast reestablishes [118]. At high coverage, the STHM-like image is no longer observed. The STHM contrast is observed at intermediate coverage [119].

The STM tip should be very close to the surface to become sensitive to the short-range forces like the Pauli repulsion to get the STHM contrast. The switching between the conventional STM contrast and the STHM contrast occurred at early stages of a hydrogen deposition when the coverage is presumably low. It is reasonable to assume, that the surface is covered only partially in the beginning of the gas deposition. Therefore, it was suggested that only one molecule plays role in contrast formation [118].

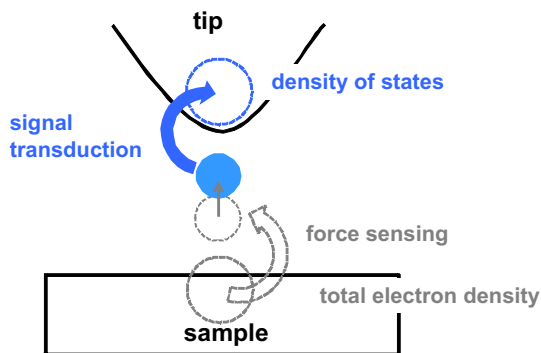Figure 1.7: A sketch describing the STHM image formation mechanism. A single hydrogen molecule is physisorbed in the STM junction. It is confined underneath the tip apex. The molecule sense the short-range Pauli repulsion from the surface and transforms this force signal into variations of the tunnelling conductance via Pauli repulsion.

The following model that describes the STHM contrast formation was

proposed (see sketch in Fig. 1.7) [80] that a single hydrogen molecule is physisorbed on the tip directly under its apex forming STHM sensor [118, 120]. A single hydrogen molecule in the tunnelling junction acts as a nanoscale force sensor and a signal transducer. When the tip approaches the surface, the hydrogen molecule is pressed into the tip what leads to the depletion of the tip DOS because of the Pauli repulsion. The tunnelling current varies nonexponentially with the distance between the tip with the hydrogen molecule and the surface. Therefore, it was suggested that the Pauli force and the conductance of the junction are coupled [80, 118].

The STHM image of a surface is formed with the tunnelling current as in case of STM. The variation of the tunnelling current is used for the image recording. STHM is intrinsically insensitive to the long-range interactions, which usually limiting the image resolution. With the molecular hydrogen attached to the tip, an STHM sensor is sensitive to a lateral variation of sample properties, other than the LDOS, like the short-range repulsion forces. The STHM ability to visualize directly the atomic structure of molecules adsorbed on the surface is valuable in the functional interfaces study. Therefore, STHM can be used as a method that reaches chemical sensitivity. It relies on the molecular properties that are characteristic of molecular species. With STHM the chemical resolution can be achieved with a little effort [80, 118].

However, the mechanism of the STHM contrast formation is not yet fully understood. The initial experiment was relied on molecular hydrogen or deuterium (H_2 or D_2) condensed in the junction of a low-temperature scanning tunnelling microscope (STM). An experiment that directly shows that only one particle plays role in the contrast formation is needed. The full explanation of the intermolecular geometrical contrast is lacking. A link between the Pauli repulsion and the junction conductance is not fully understood. Therefore, it cannot give a clear answer to the mechanism responsible for image contrast formation. Some of the questions are the issue of the current thesis.

Chapter 2

Experiment

2.1 PTCDA

The STHM experiments were performed with organic materials on metal substrates. The material of study was chosen a molecule of 3,4,9,10-perylene-tetracarboxylic-dianhydride (PTCDA). PTCDA is a well studied π-conjugated organic dye molecule [121–124], with a flat and symmetric structure. A single molecule consists of the perylene core with the anhydride functional groups at two sides. PTCDA can be easily synthesised and is stable under electron and photon bombardment. The high stability of the molecules of PTCDA allows depositing them on the surface without a sophisticated equipment, simply by the evaporation. On the metal surfaces, the PTCDA molecules form highly ordered films [125–129]. The structure of the films depends on the interactions between the molecules, as well as between the molecules and the surface. Due to the epitaxial growth and simple sample deposition procedure, the PTCDA interfaces are interesting objects for a study.

2.2 PTCDA/Au(111)

The main experiments were performed with the PTCDA molecules deposited on the $(22 \times \sqrt{3})$ reconstructed Au(111) surface. The gold reconstruction occurs due to the $\sim 4\%$ increasing of the atoms concentration on the surface and the nonuniform squeezing of the top gold layer along the $\langle 110 \rangle$ direction [130]. On the Au(111) surface, the PTCDA molecules produce lay-
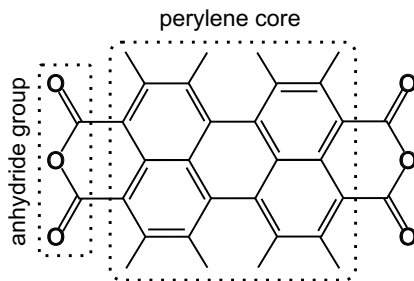
Figure 2.1: The chemical structure of the 3,4,9,10-perylene-tetracarboxylic-dianhydride (PTCDA) molecule with the marked perylene core and anhydride groups.

ers of two types: "herringbone" and "square" phase [131]. A domain of each structure type can be quite large. PTCDA is weakly bound to the Au(111) surface. At the room temperature, PTCDA molecules on Au(111) are quite mobile. They are able to create large ordered domains. At the liquid helium temperature, molecules do not move and the domains are stable.
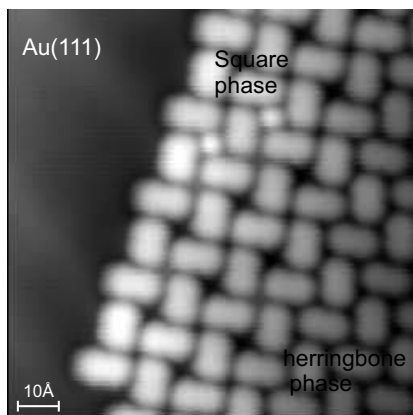
Figure 2.2: PTCDA/Au(111). Two different phases on the surface: "herringbone" phase and "square" phase. While blobs in the "square" phase are Xe atoms.

The "herringbone" phase is close to the [102] plane of the PTCDA bulk structure where the molecules are arranged in a similar way [132]. The unit cell of the "herringbone" phase is rectangular with the dimensions

$(19.2 \pm 1.0) \times (12.1 \pm 1.0)$ Å^2, [123, 124]. This arrangement is caused by the electrostatic forces between the negatively charged anhydride groups and the perylene core [133]. There are three different types of "herringbone" domains on Au(111) that are slightly different from each other. The existence of the different domains is caused by the reconstruction of the Au(111) surface. Each unit cell of "herringbone" phase has two flat-lying molecules of PTCDA that are not equivalent and have a different orientation. During the experiments we did not stick to the particular type of the domain. The experiments performed on the different domains showed no visual differences in results.

Another phase of the PTCDA layer that was observed was the "square" phase. The "square" phase consists of the PTCDA molecules arranged in a square pattern [131, 134]. The unit cell consists also of two molecules. The size of the unit cell is $(17.0 \pm 1.0) \times (17.0 \pm 1.0)$ Å^2. The density of the molecule package is less than in the "herringbone" phase. Each unit cell implies 6 mirror/rotation domains due to the symmetry of the substrate plane that has the hexagonal surface structure. Due to the large voids between the PTCDA molecules, a "square" phase demonstrates its suitability in storage of the Xe atoms.

The molecular orbitals of PTCDA change the energy because of the interaction with a substrate. For PTCDA/Au(111), the highest occupied molecular orbital (HOMO) and the lowest unoccupied molecular orbital (LUMO) are observed at -1.8 V and $+1$ V respectively to the Fermi energy level [121]. HOMO and LUMO are broadened due to the interaction with the Au $5d$-band. The shape of calculated HOMO and LUMO of the free PTCDA molecules in gas phase are shown in Fig. 2.3 [135].

2.3 Sample preparation

The sample preparation is crucial for the whole experiment because the quality of the sample directly affects the quality of results. The Au(111) sample was prepared using repeated sputtering the surface with Ar$^+$ ions at $0.8-1$ keV followed by a two-step annealing. The first step was annealing at $470°$ C for 15 minutes, is needed to restore the surface after the ion sputtering. During this step the large terraces of Au(111) (width > 100 nm) are forming. The second step of the annealing is at $180°$ C and lasts 1 hour. This step is necessary to obtain the $22 \times \sqrt{3}$ "herringbone" reconstruction of the surface. The quality of the sample was checked by LEED.
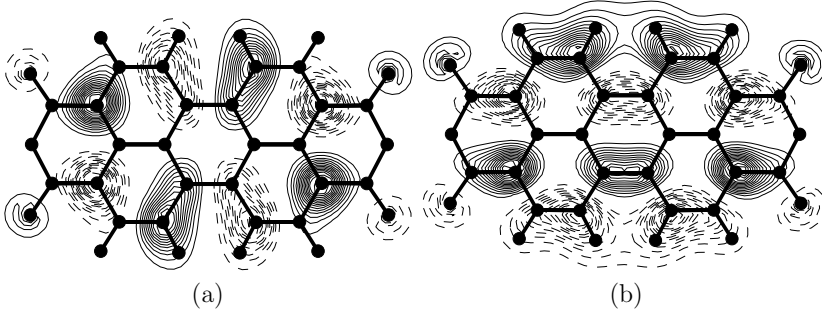
Figure 2.3: Calculated charge density of HOMO (a) and LUMO (b) of a free PTCDA molecule, taken from reference [135]. Dashed lines indicate negative values of the wave function.

2.4   PTCDA deposition

Before the deposition PTCDA molecules were kept in the oven close to the evaporation temperature, $T_{\text{dep}} = 300°\text{C}$, for 10 hours to remove possible contaminations before the deposition. The oven that was located at the distance of ≈ 5 cm far from sample. PTCDA was deposited on the sample which was hold close to the room temperature, $\approx 25°\text{C}$. The evaporation of PTCDA lasts 10 seconds with a very low flux rate to get the final coverage of PTCDA of ≈ 0.1 ML. After the deposition, the sample with the PTCDA layer is heated up to 200°C for 2 minutes. During this procedure PTCDA molecules form large islands owing to the high mobility of the molecules on Au(111). PTCDA/Au(111) form the "herringbone" phase and the "square" phase, which were important for the experiment.

2.5   Gas deposition

Gas molecules were deposited on the prepared PTCDA/Au(111) sample. The gases of H_2, D_2, Xe, CO, CH_4 are dosed in the inner cryostat where the scanning tunnelling microscope is located. The gas was introduced through a tube which points directly to the sample through a hole in a cryoshild. The hole is 0.5 cm in diameter and is covered with a shutter. In the normal state the shutter is closed to prevent the contamination of the STM tip and the sample surface. Gas pressure during the deposition was $10^{-8} - 10^{-7}$ mbar. The temperature of the STM was ≈ 5 K. At this temperature

gas condensation is possible. The gas was condensed on the cold surfaces, including the sample surface. The coverage of the gas particles was monitored by continuous scanning the surface of the crystal with the STM tip. The time of deposition was varied from half an hour up to several hours from experiment to experiment.

To estimate the coverage of the sample, a certain surface part was chosen to be scanned repeatedly. The amount of the gas particles of Xe and CO was monitored visually. Separate CO molecules and Xe atoms can be seen on the surface. The gas deposition stops as soon as the desirable amount of the coverage was reached. The molecules of Xe and CO sit stable on the surface at low temperature. Any single molecule of Xe or CO can be picked up in a reproducible way. The usual coverage of Xe and CO molecules was estimated less than <0.1 ML The tip with CO or Xe attached to its apex creates a molecular sensor that was used in experiments.

In the case of H_2, D_2, CH_4 the deposition procedure is sophisticated. The molecules of H_2 and D_2 are mobile and invisible with STM. The molecules of CH_4 are visible only if they are confined in the void of "square" phase of PTCDA/Au(111) where they spontaneously adsorb during the deposition. The coverage cannot be monitored as precise as in case of Xe or CO. Therefore, larger quantities of the molecules of H_2, D_2, CH_4 were deposited on the surface. The coverage is monitored via scanning the surface. During the scanning, switching between the STM-like contrast and the STHM-like contrast was observed. The STHM-like contrast occurs because of the spontaneous formation of the molecular sensor. Gas deposition was stopped as soon as the regular STHM-like contrast was observed. After the deposition the pressure drops back to the $1 - 10 \times 10^{-11}$ mbar. The coverage of H_2 or D_2 or CH_4 molecules was estimated less than <1 ML. The molecules of H_2, D_2, CH_4 cannot be picked up in a controllable and reproducible way. The sensor was formed spontaneous during the scanning, but after the sensor is formed it was stable enough for measurements.

2.6 Tip preparation

2.6.1 Tip for STM sensor

For the first STHM experiments the self-made tungsten tip was used. A piece of wire 0.4 mm in diameter was cut and placed afterwards in the tip holder. The wire was electrochemically etched in the hydroxide solution of

50 g NaOH in 50 ml H_2O. Next, it was rinsed in the distillate water and dried with N_2. To remove the rest water and the oxide cap, the tip was annealed in the preparation chamber simultaneously with the electron bombardment. The tip was placed inside the STM chamber in a working position. The tip was covered with molecules of gold by numerous dipping into the gold surface. For gentle tip forming, the approach distance was around $10 - 15$ Å while the initial tip-surface separation range was estimated $7 - 10$ Å, therefore the tip was dipped for $5 - 10$ Å in the surface. For tip in a bad quality, the depth of dipping was up to 50 Å. The PTCDA island was scanned to check the quality of the tip. Better contrast corrugation of the islands corresponds to the sharper tip geometry.

2.6.2   Tip for AFM sensor

For the combined STM/AFM measurements was used the qPlus sensor [114,115]. The sensor consists of the metal tip glued to the oscillating prong made from the quartz. The tip of the sensor was made from the PtIr wire of 0.15 μm in diameter which was cut and sharpened with a focused ion beam (FIB) (see Fig. 2.4). The eigenfrequency of the qPlus sensor was 30311 Hz and the spring constant 1800 N/m. During the experiments, the amplitude of the sensor was kept at 0.2 Å. Additional preparation of the sensor is not needed because PtIr does not oxidised. Before the experiments the tip apex was covered with gold by numerous gentle dipping into the gold surface (see previous subsection).
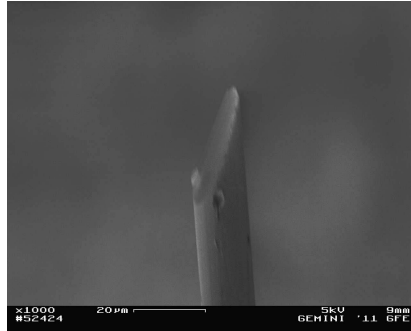

Figure 2.4: The apex of the PtIr tip of the qPlus sensor in scanning electron microscope.

Chapter 3

A single particle as a sensor

3.1 Introduction

An STM with the molecular hydrogen that is confined in the junction records the geometrical structure of the surfaces [80]. The surface scan images show that the contrast corrugation is due to the short-range Pauli repulsion. On the basis of that work it was suggested that STM tip with the molecular hydrogen in the junction acts as a microscopic force sensor that changes the tunnelling current in response to the forces acting from the surface. Such a sensor can resolve the inner structure of large organic molecules and show contrast pattern related to the geometrical structure of the molecule. The structure of junction in the case of hydrogen cannot be defined, until it is not clear how many hydrogen molecules are in the junction. The knowledge of the junction structure is important for understanding the physical phenomena responsible for image corrugation formation.

The current chapter shows that actually one single particle acts as a sensor. The proof that it is indeed a single particle was found in the set of experiments with gases other than H_2, such as CO, CH_4, Xe. These gases can also act as microscopic force sensors and can achieve geometrical resolution of the surface. Since the experiment shows that the gases behave similarly to H_2 in many ways, we can assume that in case of H_2 it is one particle that produce the contrast. The differences in the performance of these sensors suggest that the sensor functionality can be adjust by changing the sensor particle and, consequently, the interaction with the STM tip.

The results of this chapter have been published in paper: G. Kichin, C.

Weiss, C. Wagner, F. S. Tautz, R. Temirov. Single Molecule and Single
Atom Sensors for Atomic Resolution Imaging of Chemically Complex Sur-
faces. *Journal of the American chemical society*, 133:16847-16851, 2011.

3.2   Experiment

An STM experiment was performed under ultra high vacuum (UHV) con-
ditions. For the experiment the molecules of PTCDA were deposited onto the
clean Au(111) substrate using hand-made Knudsen cell as it was described
in section 2.4. The coverage of PTCDA was $\approx$0.1 ML. PTCDA formed both
the stable herringbone phases and the metastable square phase, (section 2.2).
The gases Xe, CO, CH_4 were chosen for experiments. The independent ex-
periments were performed with those gases. The molecules of gases were
deposited onto the sample with the tube pointing directly to the junction
through the hole in the cryoshild. The hole was 5 mm in diameter, covered
with a shutter. The pressure in the chamber during deposition was held
at the level of $\approx 5 \times 10^{-7}$ mbar. To monitor the deposition, the surface
was scanned; as soon as the gas particles were detected on the surface the
deposition was stopped. After the deposition, the pressure returned to the
$(1 - 5) \times 10^{-11}$ mbar.

The STM tip was 0.4 mm diameter tungsten wire, electrochemically etched
in NaOH solution. After the etching the tip was cleaned by electron bom-
bardment in UHV in the preparation chamber. Before the experiment the
apex of the tip was covered with gold by numerous gentle dips into the clean
Au(111) surface.

The distance of approach was varied, the initial tip-surface separation
range was estimated at $7 - 10$ Å, as for the tip to be gently dipped by
$5 - 7$ Å into the surface an approach of $10 - 15$ Å was needed. After the
tip preparation a PTCDA island was scanned to check the quality of the tip.
Better contrast in corrugation corresponds to sharper clean tip geometry.
Afterwards, the tip was functionalized with a particle of one of the three
following gases: xenon (Xe), carbon monoxide (CO), and methane (CH_4)
(see later). Such sensors (tip with the particle attached to its apex) were
used to scan the PTCDA/Au(111) in the constant height regime.

3.2.1 Xenon

The suggestion that the closed-shell noble gas particles should behave similarly to H_2 (D_2) was proposed earlier (see in ref. [80]). Therefore, Xe was used first as a gas with closed shell electron configuration ([Kr]$5s^2 4d^{10} 5p^6$). At low temperature Xe has low mobility on the surface and on the tip. Xe has large atomic mass and high melting point of 161.4 K, whereas H_2 (D_2) has melting point of 14.01 K and has high diffusion rate along the surface at low temperature. For the same reason the imaging of single H_2 (D_2) molecule with STM is also not possible.
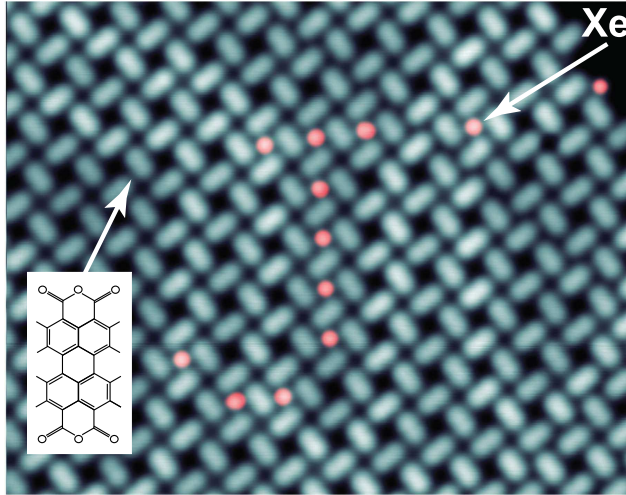
Figure 3.1: PTCDA/Au(111) metastable "square" phase. Atoms of Xe sit in the voids and at the edges of the island. Xe is marked with red dots. Picture is recorded in a constant height scanning regime.

Single Xe atoms can be easily identified on the surface with STM. Xe on Au(111) looks like a bright protrusion indicating higher conductance (see Fig. 3.1) [136, 137]. Calculations of tunnelling conductance, in which the electrodes were described within a jellium model, indicate that conductance of such structures depends strongly on the energy of the resonant state and its position relative to the Fermi energy. The unfilled $6s$ resonance level of Xe is located ≈ 4 V above Fermi level. Calculations show Xe $6s$ level is broadened and extends further out into the vacuum than the bare-surface

wave functions [138–140]. Modern calculations were made by Zotti *et al.* with *ab initio* transport methods [141]. The interaction between the tip and the surface was found to be screened with a dipole moment induced in a noble gas particle in the junction. In the junction, a particle of a light noble gas like He, Ne or Ar leads to the weakening of the metal-metal coupling and, consequently, to reduction of the tunnelling current. But for Xe and Kr model shows an existence of the additional tunnelling path that occur due to the valence p state. Tunnelling through the new path overcomes the screening effect what results in enhancement of the tunnelling current. No significant change of the LDOS of the tip was not found, what is in variance with model proposed by Lang [138].

Xe can jump from the surface to the tip and back under the applied bias. After the Xe atom jumps to the tip, to keep the initial tunnelling current the piezocrystal retracts the tip by 0.6 ± 0.1 Å (see Fig. 3.2).
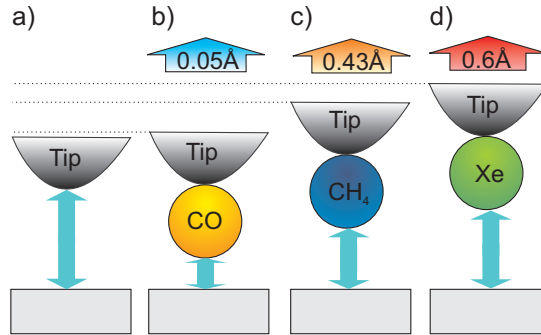
Figure 3.2: The change of the piezocrystal length in vertical direction to keep tunnelling parameters unchanged ($I = 0.1$ nA and $V = -10$ mV). The change in case of (a) clean tip, (b) CO-tip, (c) CH$_4$-tip, (d) Xe-tip.

Individual Xe atoms can be easily found on the surface. Usual places are the edges of the PTCDA islands (see Fig. 3.1) and the voids of the metastable "square" phase [142]. In the experiment the voids of the "square" phase were used to store single Xe atoms. At 5 K Xe can be stored in the voids for unlimited time and reproducibly picked up and put down again. The Xe molecules on the edges, sit rather loose, so they can move along the edges interacting with the tip. And it is still possible to pick single molecule up with the tip. For large coverages Xe tends to form the islands near the step-edges of the gold terraces.
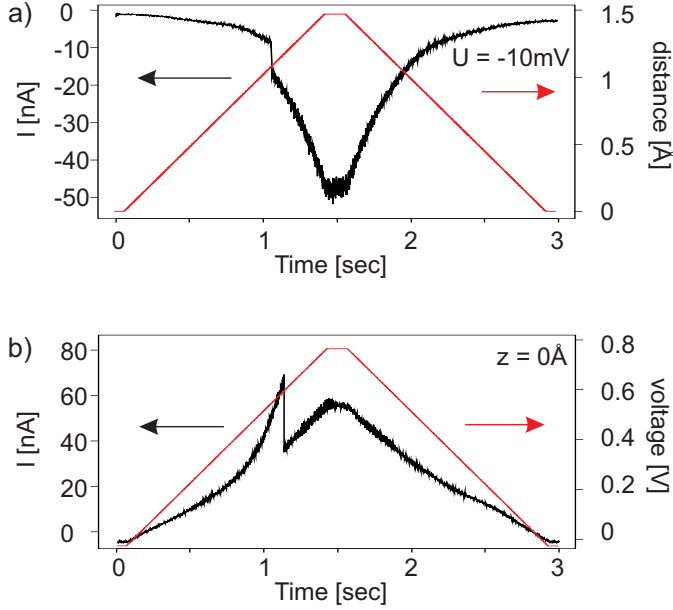
Figure 3.3: (a) Picking up a Xe atom. Approaching procedure of the tip (red line) and response of the current (black line) (b) Putting down Xe in the void. Voltage variation procedure (red line) and current response (black line). Jump in the current denote the moment when Xe jump to (a) or from (b) the tip.

The first experiments with single Xe atom manipulation were performed by Eigler and Schweizer [136]. It has been shown that Xe can be successfully picked up from the Ni(110) surface and placed back with STM tip. The picking up procedure described by them was adapted in the current work for picking up Xe from the Au(111) surface. It was taking into account that Au(111) is less attractive than Ni(110). In the present work the tip has been moved from the stabilisation point (bias -10 mV, current 50 pA) towards the Xe on the surface, for a distance of ≈ 1.6 Å, until Xe spontaneously jumps to the tip. In case of the Xe jump, the STS spectra show abrupt increase of the conductance, see Fig. 3.3(a). To put Xe back on the Au(111) surface or in the void of the "square" phase of PTCDA, we apply the potential of -0.8 V to the junction [143]. The STS spectra show an abrupt decrease of the conductance (see Fig. 3.3(b)). Thus, the STS spectra can be used to monitor the process of Xe transition from the surface and back to the tip. The additional control

was carried out by rescanning the surface and checking if Xe is still on the surface. The described protocol of the Xe atom manipulation is reliable and reproducible. This allowed us to study the imaging properties of STM tips decorated with a single Xe atom systematically.
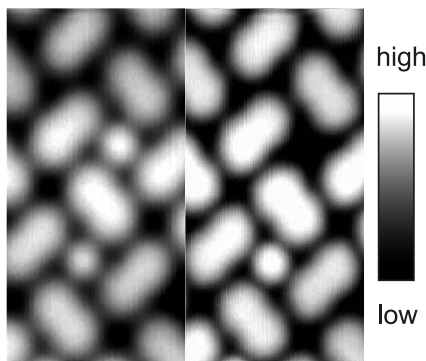
Figure 3.4: PTCDA/Au(111). The change of the contrast before (left) and after (right) the atom of Xe was picked up from the void. In case of scan image made with Xe on the tip the edges of PTCDA molecules looks sharper. The images are recorded in the constant current regime. The current flow value is shown by the colorbar.

The images of molecules, recorded by scanning in the constant current regime with the Xe on the tip apex, show the slight change in the contrast. The edges of the molecules are sharper (see Fig. 3.4) [139]. The current and the conductance images, recorded very close to the surface in the constant height regime, show the similar contrast as in the H_2 (D_2) case. The geometrical structure of the molecules is visible (Fig. 3.5). However, the Xe-decorated tip shows poorer contrast of the intramolecular geometry structure of PTCDA than the H_2 decorated tip. Nevertheless, the preparation of the Xe-sensor is explicit and better controlled than preparation of H_2- or D_2-sensors [118].

As an other example the internal geometry structure of a copper phthalocyanine (CuPc) molecule on Au(111) was successfully resolved with Xe on the tip. The experiment with CuPc molecules is sophisticated because the molecules are mobile on Au(111) and do not stick to the Au(111) substrate as good as PTCDA molecules. Due to the interaction with the tip, CuPc can follow the tip along the surface. To obtain an image of CuPc, the molecule was pinned to the edge of PTCDA island where the mobility of CuPc is reduced significantly due to the interaction with the edge of PTCDA island.
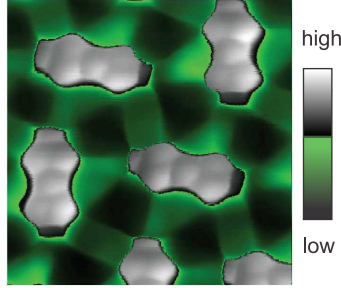
Figure 3.5: The image of PTCDA/Au(111), recorded in the constant height regime with Xe modified tip. The image shows geometrical structure of the PTCDA molecule similar to that obtained in STHM experiments. The contrast in case of Xe is poor but the geometry of the molecule is visible. The current flow value is shown by the colorbar.

The geometrical contrast on the CuPc molecule is displayed in Fig. 3.6. To get a better view of tiny details, it is shown as 3D plot.
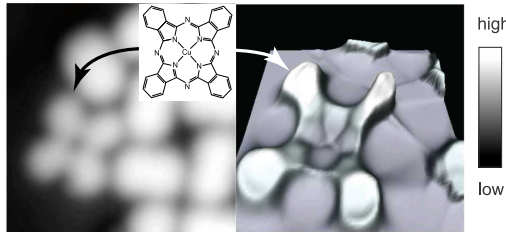
Figure 3.6: Images of a single CuPc molecule at the edge of the PTCDA island on Au(111), obtained in the constant current regime (left) and in the constant height regime (right). For better view the contrast and the inner tiny structure, it is plotted as a 3D surface. The current flow value is shown by the colorbar.

Another experiment with Xe was performed with PTCDA/Ag(110), where the structure of the PTCDA overlayer is completely different. On Ag(111), the structure is mainly "herringbone", which is very close to the [1 0 2] plane of a bulk structure of the PTCDA crystal. This happens because the intermolecular interactions are much stronger than the interactions between the molecules and the surface [132]. On Ag(110), molecules of PTCDA form commensurate "brickwall" phase [144, 145] for the coverage less than 1 ML [146]. The interaction between the molecules and the surface is stronger

than between the neighbouring PTCDA molecules. Therefore, the PTCDA molecules will be oriented perpendicular to the rows of the silver atoms, with the central C_6 ring located between the atomic rows [144]. Due to the interaction between the negatively charged anhydride groups and the positively charged perylene cores, PTCDA molecules form rhombic islands where the negatively charged anhydride groups face each other. These places are additionally preferable for Xe atoms, where they can be found easily. The Xe atoms adsorb above the adjacent anhydride groups, see Fig. 3.7(a), and can easily switch between neighbouring positions 1 and 2. The jump to another adjacent anhydride groups position is restricted by the interaction with the PTCDA molecules.

A scan of PTCDA/Ag(110) recorded with Xe sensor is displayed in Fig. 3.7(b). The scan is recorded in the constant height regime and shows the STHM-like geometrical contrast where is possible to recognize the perylene core with the bright central ring. It is observed a drop of the current where the C-C bond between adjacent C_6 side ring is, but in fact it is very subtle. Nevertheless, it is possible to see it in the current profile across these two rings in Fig. 3.7(c), where the dip and its position on the scan is marked with the red arrow.   Difference in the STHM-like contrast can be due to the structure of the Ag(110) surface that has rectangular unit cell and is more attractive than Au(111) surface. PTCDA molecules are oriented perpendicularly to the rows of sticking out Ag atoms. The central C_6 ring of PTCDA is located above one of the row. Side C_6 rings are in average farther from the surface. Due to the strong interaction between PTCDA molecule and Au(111) surface geometry and electronic structure deviates from the free molecule form [147,148]. Due to these reasons the conductance of the center C_6 rings can be higher then the side C_6 rings.

3.2.2   Carbon monoxide

The next gas which was used for experiments was carbon monoxide. Previously it was reported that CO was used in AFM experiments for tip functionalization to get high resolution of the molecules [149, 150].   The AFM experiments have shown that it is possible to recover the structure of the molecule measuring the frequency shift of the dynamic AFM sensor. Scans of the organic molecules reveal the geometrical structure which looks similar to the structural formula from chemical books. Authors Gross *et al.* ascribe the contrast obtained with such tip to repulsive Pauli force [149]. Temirov *et al.* have linked STHM contrast also to the Pauli repulsion [118].   Therefore
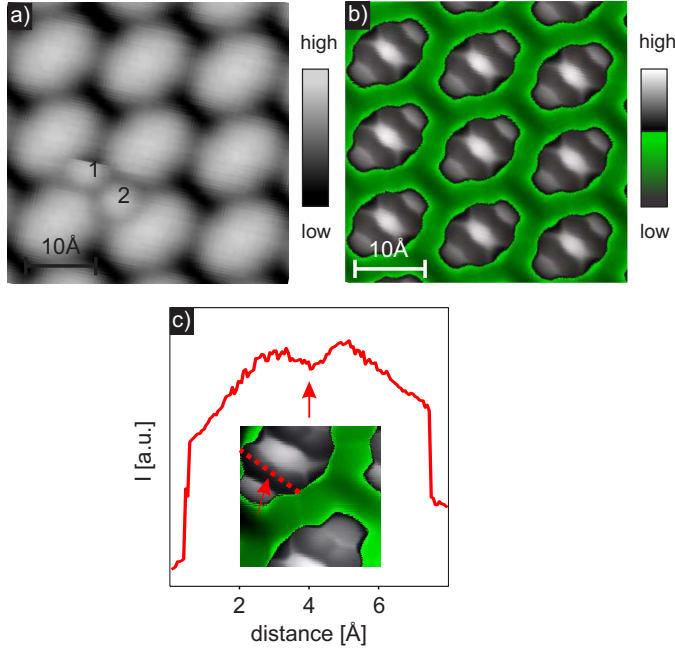
Figure 3.7: PTCDA/Ag(110), "brickwall" phase. The scan images are made with Xe on the tip: (a) Image made in constant current regime. Xe molecule sits above adjacent anhydride groups and can switch from position 1 to 2 under the interaction with the tip. (b) Image made in the constant height regime, (set point 50 nA, 50 mV, voltage applied to the junction -10 mV). (c) Current profile along the dotted line across the double C_6 rings (see inlay figure), the dip in the conductance is shown with the red arrow. Dip position coincide with the location of C-C bond.

the next logical step is to check whether CO can be used to get STHM-like geometrical contrast. This would confirm this aspect of STHM imaging.

The CO molecules present in every vacuum chamber as a rest gas, so it is possible to find them on the surface. In the experiment for the reasons of clarity CO was deposited on the freshly prepared system in amount of ∼0.01 ML. The CO molecules sit on the Au(111) surface in the on-top sites and are orientated perpendicular to the surface with carbon end down [151, 152]. A single molecule of CO is visible with STM and has a distinct appearance that makes it easy to distinguish on the surface: CO molecule appears as

depression independent of the polarity when they are scanned with a clean STM tip [151, 153]. CO appears as protrusion independently of the bias if it is imaged with a tip with another CO molecule at its apex (see Fig. 3.8). Single molecules of CO located mainly on elbows of $22 \times \sqrt{3}$ Au(111) reconstruction [130]. Owing to the change of the surface structure between fcc and hcp, the elbows of the gold reconstruction are attractive to the adatoms of the different contaminations including CO molecules.
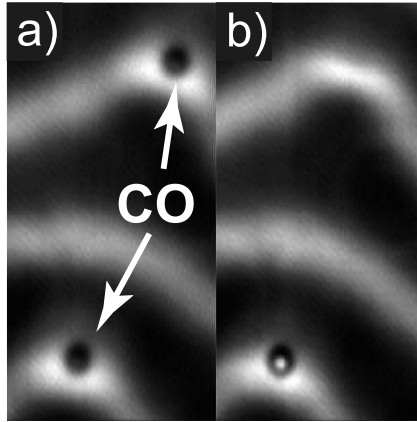
Figure 3.8: CO on Au(111), CO molecule looks like a black blob sits on the elbow of reconstruction. (a) two CO molecules scanned with clean tip. Before upper one is picked up. (b) CO molecule scanned with the CO-terminated tip. CO on the surface appears as protrusion.

The deattachment of the CO molecule occurs due to the temporary tunnelling electron injected into a $2\pi^*$ antibonding state of CO, which leads to the breakup of the bond between CO and the surface [151, 152, 154]. The excited CO molecule can jump either to a nearby atom on the surface or towards the tip. Our experiments show that CO jumps to the tip with a very high probability which is in agreement with paper reports.

The molecule of CO can be picked up in controllable and reproducible way [151]. To pick up CO from Au(111), the tip was positioned above it and the bias of 2 V was applied between the tip and the sample. The initial set point of the tip was defined with $I = 50$ pA, $V = -10$ mV (see Fig. 3.9). The checking, whether the CO molecule is on the tip, is made visually by scanning the position of the picked up CO. The quality of the tip was checked by measuring a molecule of CO that sits on the surface with the CO decorated
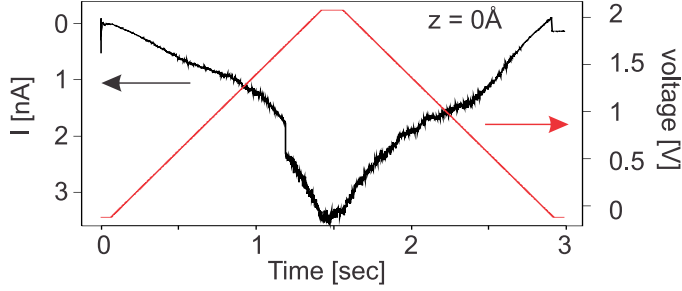
Figure 3.9: Picking up the CO. Approaching procedure of the tip (red line) and response of the current (black line). The step in the current denotes the moment when CO jumps on the tip.

tip. The control of the CO jump by spectra is complicated because the transition of CO molecule from the surface to the tip does not change strongly the conductance of the junction. Ideally a small jump in the current should look like in Fig. 3.9, but in many cases this jump was not observed, although the CO molecule jumps actually to the tip. The tip is retracted from the surface in average by ≈ 0.05 Å when CO molecule comes in the junction (see Fig. 3.2). After one CO molecule is picked up, the contrast of the scan recorded in the constant current regime changes. CO on the surface obtains a characteristic bright spot (protrusion) in a dark ring (Fig. 3.8) [151].
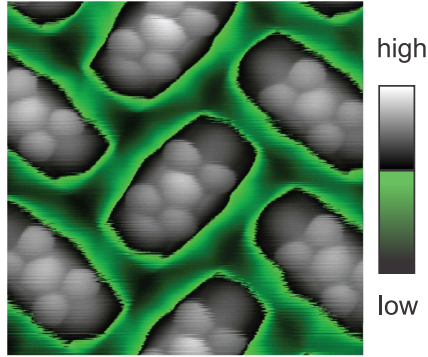
Figure 3.10: PTCDA/Au(111) scanned in the constant height regime with CO on the tip. Perylene core is visible as 5 blobs corresponding to the C_6 rings.

The CO modified tip yields better contrast resolution of the perylene core of PTCDA than the Xe modified tip. Also the C_6 rings of perylene core have a specific round shape. The two C_5O heterorings located at the ends of the molecule are not resolved as good as in case of the Xe. The specific CO contrast remains when molecules other from PTCDA species were scanned. An example of the scan image of TTCDA/Au(111) is presented in Fig. 3.11.
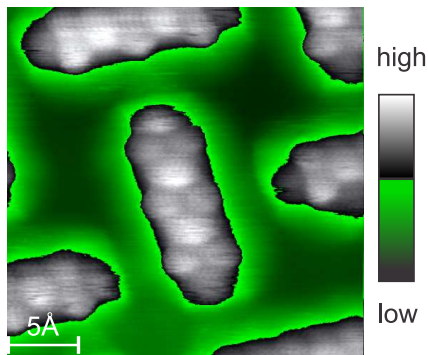
Figure 3.11: TTCDA/Au(111) scanned in the constant height regime with CO on the tip. The white blobs are corresponding to the C_6 rings of the TTCDA core.

CO-sensors are characterized by a high stability with respect to bias applied to the junction. The dI/dV image of PTCDA/Au(111) is shown in Fig. 3.12(a). This scan image was recorded at the bias $V = -1.6$ V using the lock-in techniques. At -1.6 V it is a position of HOMO of the PTCDA on the Au(111) substrate. At the same bias voltage, the dI/dV image recorded with the clean tip shows contrast (Fig. 3.12(b)) related to the HOMO of PTCDA. The comparison of two images in Fig. 3.12 (a) and (b) shows that the STHM contrast is not just an enhancement of the conventional LDOS resolution that derives from molecular electronic resonances. However, the STHM contrast is affected by the sample LDOS what makes the central ring appears dark, because the HOMO has a node there, two mutually perpendicular nodal planes perpendicular to the plane of molecule intersect there.

3.2.3   Methane

The next series of experiments were performed with methane (CH_4), because the methane molecule has right tetrahedron form with four hydro-
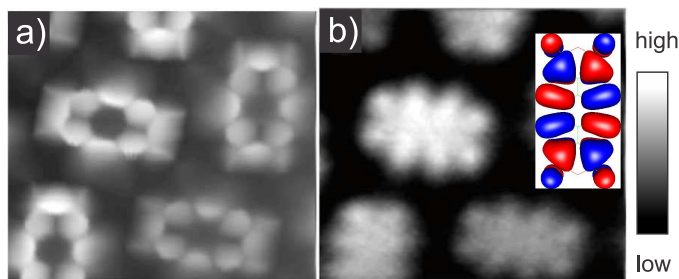
Figure 3.12: PTCDA/Au(111), (a) dI/dV image made with CO on the tip at -1.6 V. (b) Image of HOMO of PTCDA made with clean tip at -1.6 V. Inlay: model of HOMO.

gens in the corners. One corner of tetrahedron would point towards surface, whereas the other three interact with the tip and, thus, stabilize the configuration of the molecule. Because of the tetrahedron form the orientation of CH_4 on the tip can be quite different which can bring variation in conductance of the junction and in the structure of the obtained image of the surface. It is possible that one hydrogen atom sticks out or two atoms stick out. This case is similar to the orientation of hydrogen on the tip. In experiments CH_4 was picked up randomly, without any control of the orientation. No dependence on the orientation of CH_4 in the junction was revealed.

The melting temperature of methane is 91 K. A single methane molecule is weakly bounded to the Au(111). Due to the high mobility on the surface the difficulties associated with methane were similar as in case of hydrogen or deuterium. Individual CH_4 molecules can be found in the voids of the "square" phase of PTCDA/Au(111) where they spontaneously adsorb during the deposition. The observation of the CH_4 on the edges of islands is complicated because of the high mobility of the methane. Single CH_4 molecule cannot be picked up reproducibly from the voids with the STM tip as it is in case of Xe or CO. Therefore, larger quantities of CH_4 have to be adsorbed on the surface. Nevertheless, for methane the evaluated coverage was less than 1 ML. The preparation procedure of the CH_4 sensor is thus very similar to the recipe used for obtaining STHM junctions with H_2 or D_2 [80], CH_4 spontaneously jumps to the tip during the lateral scanning.

For the CH_4 the submolecular resolution of the organic molecules was observed as in the previous cases. The structure of the image is similar to STHM contrast but the intermolecular contrast is not as pronounced as in

case of hydrogen. The contrast in case of the CH$_4$ is like the contrast obtained with Xe on the tip.
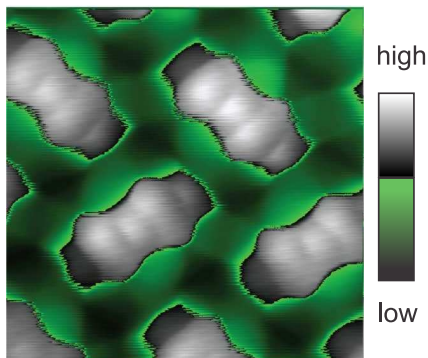
Figure 3.13: PTCDA/Au(111). The tip decorated with CH$_4$ molecule demonstrates geometrical structure of the surface similar to the STHM-like contrast.

3.3 Discussion

The experiments with PTCDA/Au(111) showed that the CO-, Xe-, CH$_4$-sensors can successfully reveal the structural contrast of the molecules deposited on the metal substrate. The obtained images had a corrugation pattern very similar to the structural formula of the whole molecule or at least parts of it. At the same time the corrugation of the intermolecular contrast changes from sensor to sensor, but the pattern related to the geometry of the molecule remains. The best intramolecular contrast was observed with CO-sensor which quality is comparable or similar to the H$_2$ sensor. The conductance above the bond and the centre of the rings have the sharpest change in its value for the used sensors. In case of CO the C$_6$ rings have specific round shape while in case of Xe and CH$_4$ the shape is angular and is closer to the hexagonal form, as in case of H$_2$ or D$_2$.

In Fig. 3.14(a) the profiles of the aromatic rings recorded above the PTCDA molecule are shown. The profiles demonstrate the corrugation of the Pauli repulsion contrast with low conductance above bonds where electronic density is larger [118]. The figure shows that the images recorded with the Xe- and CH$_4$-sensors are laterally distorted. The Xe and CH$_4$ sensors show asymmetry in the profiles across the molecule. Also the three aromatic

rings along the profile have different sizes. Note, that the structure of the profile does not depend on the direction of the scanning. This rules out a friction and slip-stick as an origin of the asymmetry, because, otherwise, the direction of the slope will depend on the direction of scanning what will be observed in the experiment. Asymmetry of the profile and slope presence cannot be caused by the global drift of the tip from or towards the surface, the drift is small in the microscope. Since the position of the imaged PTCDA molecule does not change during the scan, the observed image distortions must be caused by deformations of the sensor due to the complex tip shape [153, 155]. In case of CO the profile is more symmetric and the least distorted comparing to the profiles obtained with Xe and CH_4 sensors. However, the distance between the extreme points of the rings in case of CO is shorter than in other cases. This can be because CO is bounded stiff to the tip while xenon or methane sit loosely and can move on the tip [156, 157]. But still, it can be possible that the image is distorted because of the tilt of CO on the tip [153, 158].
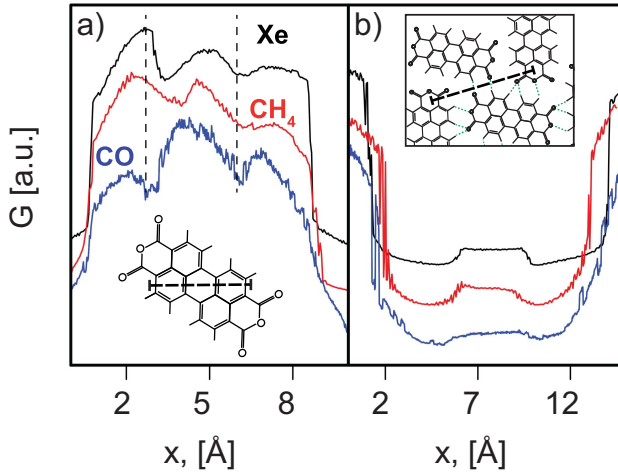
Figure 3.14: PTCDA/Au(111). Conductance profile across the molecule (a) and the bond (b). Each of the curves was divided by the factor $|G_{\max} - G_{\min}|$, where $G_{\max}$ ($G_{\min}$) are the maximum (minimum) values of the conductance in the current curve. The resulting curves were shifted along the vertical axis.

Xe- and CH_4- sensors show intermolecular contrast which coincides with the contrast obtained with H_2 (D_2) sensor. The area between the molecules

is broken up into the tiles of different sizes and conductances. The tiles with small conductance have three PTCDA molecules as a neighbour and have large size. The tiles of low conductance interchange with tiles of high conductance. They are smaller and have two PTCDA molecules as a neighbour. The edges of the tiles are in good agreement with the location of H−H bonds [142]. The profile recorded across the hydrogen bonds (see Fig. 3.14(b)) shows that, in fact, all three sensors behave in a similar way and are sensitive to the difference of the conductance over different points of the intermolecular area. In case of Xe- and CH$_4$-sensors, the conductance drop is stronger above the hydrogen bond and has a kink unlike in case of CO. In case of CO, conductance profile varies smoothly with a small variation of magnitude in the areas where H−H bonds should be. It is hard to observe a variation at that region on the scan images because of the very weak contrast variation. The mechanism of hydrogen bond imaging in STHM is not yet fully understood, so the poor performance of the CO-sensor can be related to some distinctive properties of CO.

To understand better the variation of the intramolecular contrast between the different sensors, we analysed the STS conductance spectra versus tip-surface separation distance. The conductance spectra $G(z)$ measured in two neighbouring points (see inset of Fig. 3.15) are shown in Fig. 3.15: over the center of side ring (black) and over the side carbon atom (red). All the $G(z)$ curves plotted in Fig. 3.15 show a similar exponential dependence far from the surface and nonexponential behaviour at short tip-sample distances. The analogous behaviour was demonstrated earlier for the spectra made with molecular hydrogen and deuterium in the junction [118].

Far from the surface the conductance $G(z)$ spectra are exponential. The deviation from the exponential behaviour emerges at some point and increases with the reduction of the tip-surface distance (See section 1.5). The suppression of the conductance is presumably due to the depletion of the DOS in the tip caused by Pauli repulsion between the tip and the particle adsorbed at the tip apex [118]. At the distances close to the surface spectra behaves nonexponential and show distinction in curve shape for different tip positions above the surface, The spectra measured above a carbon atom (red curve) show larger suppression of the conductance than the spectra measured above a center of C$_6$ ring (black curve) of the PTCDA backbone. This distinction leads to the pattern corrugation in conductance scan images. The first point where the deviation emerges marks the starting distance when the STHM-like contrast will be observed in the scan images. STHM-like contrast, observed in the scans of the surface, happens at the very short tip-surface distances where the spectra are nonexponential.
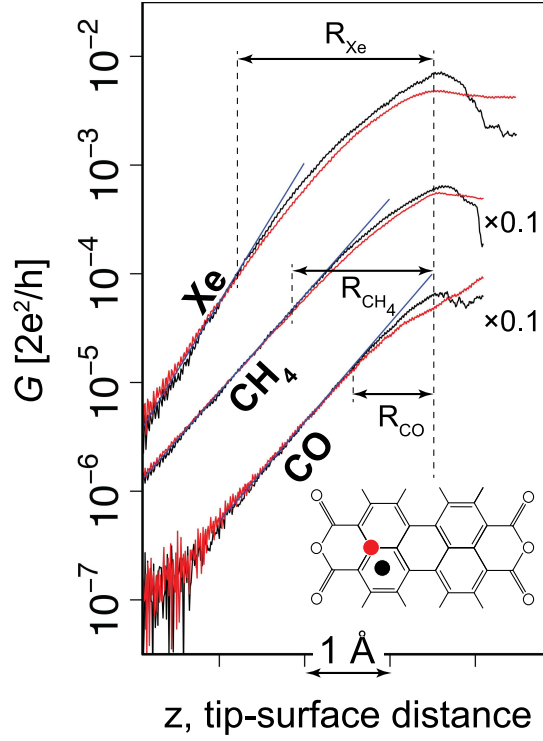
Figure 3.15: The approach conductance spectra measured above PTC-DA/Au(111) from the stabilization point: $I = 50$ pA, $V = -10$ mV. x-axis shows the relative distance between the surface and the tip. The curves were shifted along the z-axis such that the tip-surface distances, at which the Figures 1d, 2c, and 2g were scanned, coincide. For visual clarity the curves of CH_4 and CO were multiplied by 0.1.

The tip-surface distance at which the geometrical contrast is observable is different for three sensors. The sensitivity range, R, was introduced for the sensor characterization. One endpoint of R-range is defined by the tip-sample distance where the first deviation from the exponential behaviour occurs. Another endpoint is the tip-surface distance at which the maximum difference in conductance values over the atom and over the center of the C_6 ring is observed. Sensitivity range, R, shows how deep it is possible to probe the space under the tip (see Fig. 3.16). In case of Xe the sensitivity range is larger than in case of CO. According to Fig. 3.15, $R_{Xe} > R_{CH_4} > R_{CO}$. This
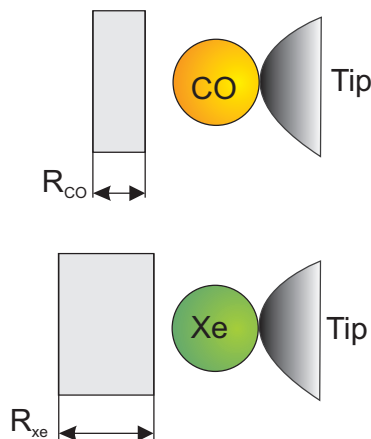
Figure 3.16: Sensitivity range defines how deep it is possible to probe the space under the tip. In case of Xe the sensitivity range is larger than in case of CO. This corresponds to the fact that with the Xe intermolecular and intramolecular contrast are observed while in case of CO only intramolecular contrast is presented.

means that the Xe- and CH_4-sensors produce detectable output in a wider range of tip-surface distances, while the sensitivity of the CO-sensor decays faster as the tip is moved away from the sample surface.

3.4   Conclusions

In this chapter it has been shown that the STM tip with a single CO or CH_4 molecule or with a single atom of Xe creates a single particle sensor that simultaneously performs the function of an atomic-scale force sensor and a signal transducer, which couples the short-range force acting on the tip to the tunnelling conductance of the junction. These sensors have successfully resolved the inner structure of large organic molecules like PTCDA and CuPC and have shown the scan image contrast is related to the geometrical structure of the molecule. The scan image contrast have similar pattern for all different gas particles used in experiment. Therefore, the mechanism of the submolecular geometrical contrast formation does not depend on the details of the sensor particle or its interaction with a tip. This points out that it should be a general physical phenomenon. Experiments with Xe and

CO have shown explicitly that only one molecule or one atom is needed to create the molecular force sensor. Therefore, one can conclude that in case of H_2 or D_2 also only one molecule on the tip apex should play role for sensor formation but not a molecule on the surface under the tip. To get the STHM contrast hydrogen molecule jumps and sticks to the tip, what happens during the motion of the tip above the surface. The area where the sensor was created and where it was used for scanning are spaced far on the surface what excludes the situation when the tip "drags" the particle along the surface. During dragging the particle will be lost because of the numerous defects and the terraces on the surface. Therefore, the single particle sensor really consists of the single molecule of the gas attached to the tip apex.

The studies of the PTCA molecules on different substrates show common pattern of the geometrical contrast, however, slight variations are observed in the contrast. The substrates of Au(111), Ag(111) or Ag(110) have different morphology and physical properties that affect the electronic structure of the PTCDA molecules and shift the position of the HOMO and LUMO of the PTCDA molecule. The full contrast observable in experiments with single particle sensor has variations due to the different electronic structure of the molecules but the geometrical pattern, ascribed to the geometrical structure of the molecule, remains and is the same for all the crystal surfaces.

For sensor characterization the parameter R, sensitivity range, was introduced. Sensitivity range determines how deep the sensor can probe the space underneath it. The CO-sensors have the short sensitivity range, while Xe- or CH_4-sensors have large sensitivity range. The sensors with large R show poor contrast for the intramolecular area and matching contrast of the intermolecular area related to the hydrogen bonds. Sensors with small R works in the opposite way, they show poor structure of the intermolecular area, but they show intramolecular contrast of good quality. H_2 and D_2, as well as Xe, are able to resolve the intermolecular structure, therefore, the sensors made with H_2 or D_2 presumably should have large sensitivity range.

Chapter 4

Calibration of the atomic-force sensor

4.1   Introduction

The STM tip decorated with a single molecule of CO or CH_4 or with a single Xe atom acts as a molecular force sensor. The action of that sensor is similar to the cases of H_2 or D_2 which were reported earlier [80]. Such sensors were suggested to be able to change the tunnelling current in response to the forces acting from the surface. Therefore, an image of the tunnelling current variation, recorded with the tip in a constant height, reflects the Pauli repulsion effect from atoms. The image of the surface shows the structure of the surface. For molecules deposited on the surface, the image will reflect the structure of the molecules. The structural resolution of the molecules on the surface was obtained independently using an AFM sensor with CO decorated tip [93, 149, 159]. Gross *et al.* [149] have shown direct observation of Pauli repulsion from atoms. These two observations point out that there is dependence between the force acting on the sensor and the tunnelling current.

Current studies show that STHM contrast is related to the force acting on the tip and therefore, it is possible to calibrate the signal in the conductance channel in terms of force. For calibration, it is necessary to separate the effect of the force acting on the sensor from all other factors influencing the conductance. The force cannot be tuned by simply changing the tip-surface distance, because in such cases the tunnelling current follows the changes of LDOS. In experiment, the PTCDA molecule itself will be used as a force

source. It has been shown that planar organic molecules can be used to vary the force acting on the tip in the pN range; if the tip is at a constant distance from the substrate and is placed at different locations of the molecule [149]. Measurements in two closely spaced points in the PTCDA molecule show that LDOS does not vary significantly. In this case, all the variations in tunnelling conductance are only due to the change of the force acting on the tip.

A combined NC-AFM/STM sensor has an advantage that it can measure the force and conductance spectra simultaneously. STM images LDOS at the position of the tip, where the tip is far above the molecule. So the tip probes not only a molecular orbital in its exponential tail, but also the tail of metal states that may leak through the molecule and blur the resulting picture. AFM relies on the force measurements. To image the atomic resolution the tip should be moved very close to the object of study. Here the AFM sensor is in a regime where short-range forces give the main contributions. Pauli repulsion is responsible for the atomic resolution, while van der Waals and electrostatic forces add only a diffuse attractive background [149]. This problems can be partially solved with a reduced contribution of the long-range forces by using FM-AFM and the force gradient measuring. The force gradient in the proximity of the surface depends mainly on rapidly varying short-range forces, while long-range forces vary rather slowly, and so can be neglected in FM-AFM. Additionally, at small distances, the results of measurements are affected by an influence of the exact atomic tip geometry and unintended lateral and vertical movement of the molecules. The functionalization of the tip with an atom or a molecule allows the reactivity of the tip to be reduced and therefore, the tip can move closer to the surface.

Using a combined NC-AFM/STM sensor the tunnelling current and the frequency shift were measured simultaneously at different tip-surface distances. This information was used to reconstruct the force and conductance spectra as a function of the proximity to the surface. These spectra were analysed for the possibility to calibrate the sensor. As the relation between the force and the conductance is known, it is possible to use an STM tip as a microscopic force sensor when a molecule or an atom is attached to its apex.

The results of this chapter have been published in paper: G. Kichin, C. Wagner, F. S. Tautz, R.Temirov. Calibrating atomic-scale force sensors installed at the tip apex of a scanning tunneling microscope. *Physical review B*, 87:081408, 2013.

4.2 Experiment

An experiment was performed with NC-AFM/STM in UHV conditions at 5 K. A test system was chosen as PTCDA/Au(111). The preparation of PTCDA/Au(111) is described in section 2.3. Above the monolayer of "herringbone" phase of PTCDA was chosen an area 13×13 Å^2 containing one molecule. The probing of the surface was made with the qPlus sensor [114] with PtIr tip (see Fig. 2.4). Preparation of the tip is described in section 2.6.2. The operational oscillation frequency of the qPlus sensor was $f_0 = 30.3$ kHz. During the measurements, the amplitude of the sensor's oscillation was kept constant at ≈ 0.2 Å [160]. Constant height scan images were made with small tunnelling bias $V = -12$ mV applied to the junction.

Three different types of tips were used: a clean Au tip, an Au tip decorated with a single CO molecule and an Au tip decorated with a single Xe atom. Sequences of images with frequency shift (Δf) and conductance (dI/dV) were recorded simultaneously at various tip-surface distances with a step of 0.1 Å. Spectra of frequency shift ($\Delta f(z)$) and conductance ($dI/dV(z)$) were extracted from the sequence of scanned images. For calibration spectra two particular positions on the molecule were chosen. One spectrum of interest was obtained for the central point of the central C_6 and the other above the nearest carbon atom, indicated by the blue and red circle in Fig. 4.1(a). These two points are located ≈ 1.4 Å from each other. For these two points, force and conductance spectra have been obtained. Force spectra, $F(z)$, were obtained by integrating frequency shift spectra over the measured range of distances,

$$F(z) = \int\limits_{0}^{z} \frac{2k_0}{f_0} \Delta f(z) dz, \tag{4.1}$$

where $k_0 = 1800$ N/m is the fork stiffness of the qPlus sensor and $z = 0$ is the maximal distance from the surface, at which the scan image was recorded. z increases as the tip approaches the surface. For large tip-to-surface distances, no corrugation in image contrast was observed [161].

A sequence of images recorded with a clean Au tip shows featureless contrast without any internal structure of the molecule at any distance (Fig. 4.1(a)). Spectra extracted above the ring and above the atom (see Fig. 4.1(b)) are identical, so

$$F_{\text{atom}}(z) = F_{\text{ring}}(z) \tag{4.2}$$

and

$$dI/dV_{\text{atom}}(z) = dI/dV_{\text{ring}}(z). \tag{4.3}$$

Figure 4.1: (a) 13×13 Å^2 constant height Δf (top) and dI/dV (bottom) images from the image sequence of PTCDA/Au(111) measured at different heights with the clean Au tip. The chemical structure formula of PTCDA is shown in the tile, red and blue circles mark the positions at which $F(z)$ and $dI/dV(z)$ were evaluated. (b) Force $F(z)$ (top) and conductance $dI/dV(z)$ (bottom) spectra extracted from the image series (a). Spectra were measured over the atom (red curve) and over the middle point of central C$_6$ ring. For F scale negative (positive) value corresponds to an attractive (repulsive) force.

LDOS of PTCDA does not deviate significantly between these two locations. Force $F(z)$ spectra in Fig. 4.1(b) show that clean Au tip is quite reactive. The tip senses a strong attraction toward the surface [162]. At $z \approx 3$ Å, white patches on the Δf image show local interaction of the tip with the corner oxygens of PTCDA. This points out the chemical nature of the attraction. The corner oxygen flips up and tries to form a chemical bond with the tip [163]. As the tip approach further towards the surface, the interaction increases and destabilizes the junction.

Unlike the clean tip, a tip with attached CO molecule is able to show the internal molecular structure of PTCDA in both Δf and dI/dV channels

Figure 4.2: (a) 13×13 Å^2 constant height Δf (top) and dI/dV (bottom) images from the image sequence of PTCDA/Au(111) measured at different heights with the Au tip decorated with CO molecule. (b) Force $F(z)$ (top) and conductance $dI/dV(z)$ (bottom) spectra are extracted from the image series shown in Fig. 4.2(a). Spectra were measured over the atom (red curve) and over the middle point of central C_6 ring.

(see Fig. 4.2(a)). The appearance of structural resolution in the scan image measured at $z = 2$ Å shows that at this distance the tip feels the short-range Pauli repulsion acting on it from PTCDA. Extracted force spectra also prove this statement. The force rises faster over the atom than over the ring center (Fig. 4.2(b)).

For CO terminated tip the values of

$$\Delta F(z) = F_{\text{atom}}(z) - F_{\text{ring}}(z) \tag{4.4}$$

and

$$\Delta dI/dV(z) = dI/dV_{\text{atom}}(z) - dI/dV_{\text{ring}}(z). \tag{4.5}$$

show distinct variation with tip-surface distance. Far from the surface ($z = 0$) $\Delta F(z) = 0$. This value grows as the tip approaches the surface, reaching a maximum value at the distance $z \approx 2.2$ Å. Here $\Delta dI/dV(z)$ is negative and keeps decreasing with the tip approach. Spectra show that junction conductance drops with an increase of the force acting on the tip. Close to the surface, at distances $z \gtrsim 2.3$ Å, the value of $\Delta F(z)$ starts to become negative. Inversion in Δf happens at smaller z' values ($z' < z$), which follows from Eq. 4.1. In the spectra we observe a change of sign for $\Delta F(z)$ and Δf. In the frequency shift scan images, this effect leads to the contrast inversion (see Fig. 4.2). Far from the surface C-C bonds are bright and the rings are dark. Frequency shift for tip positioned above the rings is smaller than over the atoms and bonds (see Fig. 4.2). For $z > 2.2$, the frequency shift Δf above the ring become larger than over the atoms or bonds. At the same $z \approx 2.2$, $\Delta dI/dV(z)$ shows a weak response to the change in tip-surface interaction, which can be due to different types of tip-surface interaction. The emergence of an attractive force cannot be described with a simple two particle Lennard-Jones type potential. The emerged attraction can be due to the complicated structure of the junction that has a large number of degrees of freedom, owing to the particle in the junction. For instance, lateral movement of the particle can influence strongly on the interactions in the junction. Therefore, at short tip-surface distances, the coupling between $\Delta F(z)$ and $\Delta dI/dV$ might have a different character of relation.

The Xe-sensor shows similar behaviour to the CO-sensor. The relation between $\Delta F(z)$ and $\Delta dI/dV$ have similar characteristic as in the case of CO. The molecular structure of PTCDA starts become visible at distances starting from $z \geq 3.1$ Å. Visually the corrugation of image contrast is not as strong as in the case of CO-tip. Thus, the difference between minimum and maximum values of the conductance and force is larger for Xe in comparison with CO. Poor quality of the image resolution and spectra can be caused by several reasons. The tip with Xe is more reactive than the tip with CO (compare in Figs. 4.2(b) and 4.3(b) spectra of Δf and $\Delta dI/dV$), and less reactive than the clean tip (compare in Figs. 4.1(b) and 4.3(b) spectra Δf and $\Delta dI/dV$). Another reason may be a small contribution of Δf and $\Delta dI/dV$ to the total signal comparable to the total signal, which makes it hard to detect. Also the tip with Xe is more sensitive to the amplitude of qPus sensor oscillation, because of the soft Xe-tip bond. Displacement of Xe in the junction adds blur to the scanned images and spectra.

Large conductance of the junction with Xe is due to the existence of additional tunnelling channels through the valence $5p$ state of Xe [141]. The state is broadened due to the strong hybridization with the gold states. Xe
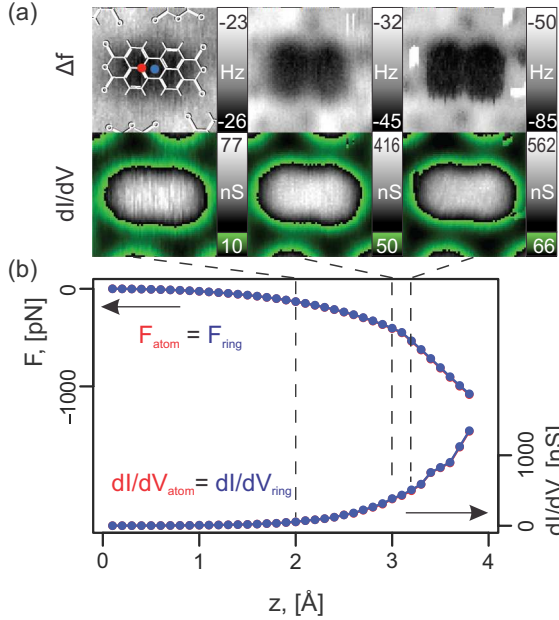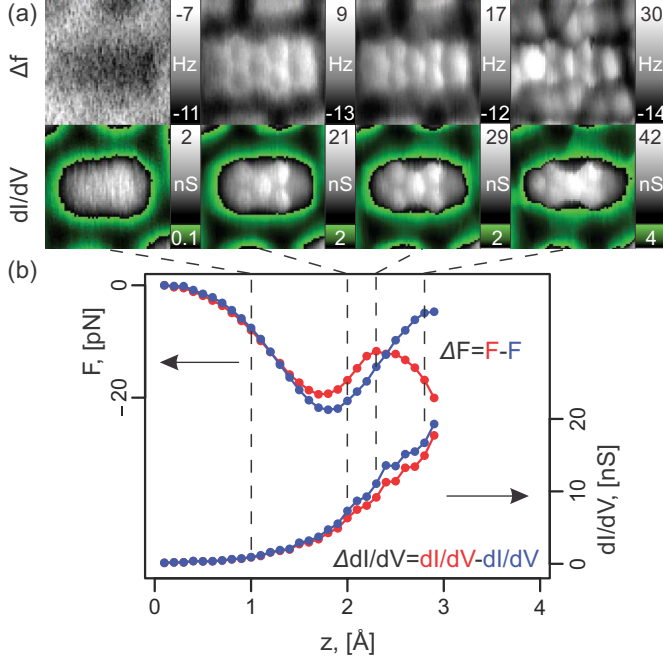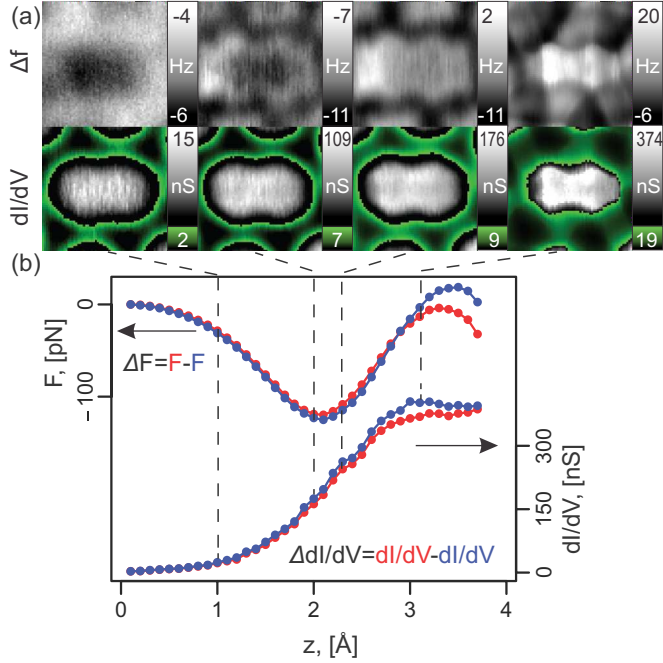
Figure 4.3: (a) 13×13 Å^2 constant height Δf (top) and dI/dV (bottom) images from the image sequence of PTCDA/Au(111) measured at different heights with the Au tip decorated with Xe atom. (b) Force $F(z)$ (top) and conductance $dI/dV(z)$ (bottom) spectra extracted from the image series shown in Fig. 4.3(a). Spectra were measured over the atom (red curve) and over the middle point of central C$_6$ ring.

also induces a dipole moment which screens the interaction between the leads, and decrease the conductance [141]. Nevertheless, the contribution to the tunnelling through $5p$ state is quite large and overcomes the screening effect. This disagrees with the calculations of Ref. [138, 139], where the calculated electron transport through Xe was found to occur through the tail of the $6s$ orbital.

4.3   Discussion

$\Delta F(z)$ and $\Delta dI/dV(z)$ are used to characterize the conductance response in the acting force. To get a relation between $\Delta F(z)$ and $\Delta dI/dV(z)$ (see Eq. 4.4 and 4.5) these two values are plotted versus each other (see Fig. 4.4). Far from the surface at $z = 0$ the proportionality between $\Delta F(z)$ and $\Delta dI/dV$ was found to be linear. Linear proportionality was found in different experiments, where the tip was freshly prepared and decorated with the same type of particle. The linear proportionality was observed up to the moment when $\Delta F(z)$ changes its sign. The coefficient of proportionality for Xe was found equal to $\alpha_{\mathrm{Xe}} \approx -2000 \, \frac{S}{N}$ and for CO equal to $\alpha_{\mathrm{CO}} \approx -200 \, \frac{S}{N}$. Thus, relation between force and conductance can be unambiguously defined as linear with a single proportionality constant.
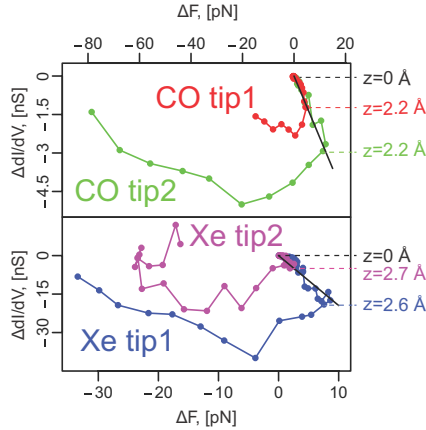
Figure 4.4: Conductance response $\Delta dI/dV$ vs the applied force $\Delta F(z)$. The upper (lower) panel shows spectra measured with two different CO (Xe) tips. The regime in which the response of conductance is linear is indicated by the black fitted lines. The distance at which each tip starts to deviate from the linear response regime is marked on the right.

The linear regime violates near the point where $\Delta F(z)$ changes its sign. It happens at short tip-surface distances, when the attractive force acting on the tip from the side of the surface dominates the interactions in the junction. In the non-linear regime, the coupling between $\Delta F(z)$ and $\Delta dI/dV(z)$ seems tip-dependent. The particle in the junction starts to behave in a complicated way. Nevertheless, for all investigated tips, coupling behaviour was

found qualitatively similar (Fig. 4.4). Remarkably, the inner structure of the PTCDA molecule is observed on a large range of z-distances even when the coupling is not only in linear but also in non-linear regimes.

Interestingly, the hydrogen bonds in intermolecular area of the STHM contrast, happens only at z-distances, where the sensor is in the non-linear regime [142,164]. Xe and CO STHM-like contrast with observable intermolecular structure is shown on rightmost tile in Fig. 4.3(a) for Xe and Fig. 4.2(a) for CO. It is possible to conclude that hydrogen bonds act in a specific way on the sensor particle. The mechanism that is responsible for the non-linear coupling is sensitive for this kind of action and transduces this force into the conductance channel.

These observations give us a reason to believe that for other molecules like H_2, D_2, CH_4, for which STHM contrast was reported, coupling between force and conductance spectra should be observed in a similar way. The coupling between force and conductance is expected to be in two regimes, linear and non-linear. It is assumed that the linear regime should be observed at large tip-surface distances, where the decrease of the junction conductance is proportional to the increase of the force acting on the tip. The linear regime is fully defined with a single proportionality constant that does not depend on the microscopic structure of the tip but only on the type of particle. At small tip-to-surface distances, non-linear proportionality is expected. The mechanism standing behind the geometrical contrast formation seems to have universal character and should not depend on the atomic structure of the tip or the particle attached to the tip. This follows from the fact that STHM images are observed for different types of particles. The molecules and the single atoms have different structures and different bonding character to the tip (chemical or van der Waals).

A possible model of STHM contrast formation was suggested by Martinez *et al.* [165]. The proposed model assumes that molecular hydrogen dissociated on the Au tip and the adsorbed hydrogen atoms, change the density of states of the tip, increasing its p-orbital and reducing the s-orbital contribution. The interaction of the H-decorated Au tip with PTCDA/Au(111) pins the Fermi energy, E_F, in the middle of the PTCDA LUMO peak and increases the sample DOS at the Fermi energy level, which allows electrons to tunnel from or to this peak at very low bias voltages. The model relies on the specific details of the chemical interaction between H_2 and Au. Dissociated H_2 should make a strong bond with the tip, and therefore the energy needed to clean the tip should be high (≈ 2 eV). This disagrees with the STHM experiments. An energy needed to clean the tip is actually much

smaller $(40 - 200$ eV$)$, which tells us that the molecular hydrogen should sit on the tip as a whole molecule. Another reason is that hydrogen molecules do not dissociate on single crystal Ag [166, 167] and the Au surfaces [168, 169], because of the considerable activation barriers that prevent this.

The model of STHM contrast formation proposed in [80] and described in section 1.5 has in fact a more general character. It implies that a particle adsorbed on the tip interacts also with the surface. The interaction between the particle and the surface disturbs the particle and shifts its position with respect of the tip during the scanning. In this case the position to the particle should contain information about the interactions. If the position of the particle changes the tunnelling current through the junction, then the force acting on the particle is coupled to the conductance. The character of this coupling will be defined by the physical mechanism through which the particle position influenced the electron tunnelling.

Currently there are two mechanisms that can possibly explain how the displacement of the particle on the tip can affect the conducting properties of the junction. According to one of them, the particle is shifted on the tip due to the interaction with the surface and is pressed into the tip. The particle changes the tip DOS via the Pauli repulsion acting between the tip and the particle. The conductance of the junction using the Tersoff-Hamann approximation, is proportional to the DOS of the tip. Here the coupling occurs due to the increased repulsion between tip and sensor particle that depletes the tip DOS close to the Fermi level [118].

Another possible model was proposed by van der Maas et al. [170]. Their model assumes that only the electrons tunnelling in some finite solid angle Ω_t give a contribution to the tunnelling current. The atom or molecule attached to the tip works as a shutter that reduces the number of tunnelling electrons by elastically scattering them back. The presence of the particle reduces solid angle Ω_t by a value Ω_s, and casts a "shadow" on the surface. Electrons in this "shadowed" solid angle are scattered back and do not contribute to the total tunnelling, thus the total solid angle that contributes to the tunnelling is $\Omega_t - \Omega_s$. The authors proposed that the solid angle Ω_t depends only on the tip, while Ω_s depends on the tip-particle distance. At large tip-surface distances, the particle sits at a constant position with respect to the tip and therefore Ω_s is constant. For large distances the tunnelling current depends only on the tip-surface separation, d, exponentially $I \propto \exp(-d)$. At small tip-surface separations, the second effect take place, the particle starts to interact with the substrate and is pushed into the tip. Due to this shift Ω_s is increased and, consequently, the total angle $\Omega_s - \Omega_t$ is decreased . Non-

linearities will be observed in the conductance spectra. In the case when the second effect is strong, the resulting tunnelling current will decrease as the tip approaches the surface.

Both models predict that the increase of the force pressing on the tip will lower the junction conductance. That is in qualitative agreement with experiments. Unfortunately, experiments cannot give a distinction between these two models. Quantitative computer simulations of the coupling are necessary for further discrimination between these two models.

4.4 Conclusions

The experiments have shown that an interrelation between conductance of the junction and force acting on the tip exists. At large distances between the tip and the surface interrelation has a linear dependence. The linear regime is stable and reproducible. The coefficient of proportionality α depends on the type of a particle attached to the apex of the tip, but not on the details of tip's or particle's atomic structure. For Xe sensor we found $\alpha_{\mathrm{Xe}} = -2000 \frac{\mathrm{S}}{\mathrm{N}}$ and for CO sensor $\alpha_{\mathrm{CO}} = -200 \frac{\mathrm{S}}{\mathrm{N}}$, where the minus sign shows that the conductance of the junction decreases with an increase of the force acting on the tip.

At short tip-surface distances the linear regime violates. The force-conductance relation starts to depend on the shape of the tip. The interrelation for non-linear regime was found qualitatively to be identical in different experiments. This approach shows that it is possible to reconstruct force from the conductance. For further study numerical calculations should be performed where the form of the tip is taken into account.

The geometrical contrast of the molecule is observed in conductance scan images at the distances where the sensor works in the linear regime and partially in the non-linear regime. The STHM-like intermolecular contrast is observed only in a deep non-linear regime, when the tip is very close to the surface. In case of D_2, H_2, CH_4 similar relation between force and conductance is also expected. With such sensors it is possible to obtain structural resolution of the surface with little effort and without additional equipment.

Chapter 5

Two level system surface scanning microscopy with D$_2$ decorated tip

5.1 Introduction

The STM tip decorated with a single molecule (CO) or a single atom (Xe) works as a microscopic force sensor that varies the tunnelling current in response to the forces acting from the surface on the tip (see chapter 4). Such a sensor is able to resolve the geometrical structure of large organic molecules. The conductance scan images show that the geometrical contrast is observed up to tunnelling biases $V \approx \pm 2$ V applied to the junction. This tells us about the stability of the junction in a very wide bias range. In contrast, for sensors based on H$_2$ and D$_2$ STHM the contrast breaks at relative low bias ($\approx \pm(10 - 100)$ mV) and at high bias conventional STM contrast is restored.

The voltage-dependent conductance spectra show a complex behaviour. For H$_2$ and D$_2$ there are specific spike-like features located symmetrically around zero bias. The spikes represent transitions between junction states. The analysis of the spikes can provide information about the property of the surface.

In this chapter voltage-dependent conductance spectra for H$_2$ (D$_2$) will be analysed. The energy of expelling H$_2$ (D$_2$) from the junction will be compared with the surface adsorption potential. For this a force-field simulation will be performed to calculate the excitation energy of H$_2$ (D$_2$) out of the junction.

The relation between H_2 (D_2) displacement on the tip and the conductance scan images will be discussed.

5.2   Experiment

The experiment was performed in UHV conditions at the temperature $T = 5$ K. For the experiment, PTCDA molecules were deposited on the Au(111) surface. PTCDA molecules form islands with the regular structure (see section 2.3). Molecular deuterium was dosed into the STM chamber from where it condenses on the sample surface. D_2 does not dissociate on single crystal Au surfaces due to the considerable activation barriers [168, 169].

To obtain the D_2 sensor, the tip was moved along the surface from where D_2 spontaneously jumps to the tip. As soon as D_2 is on the tip, the new type of contrast appears, the so called STHM contrast. The deposition of deuterium was stopped as soon as a stable STHM contrast was achieved. In the previous chapter it was shown that only one molecule is needed for contrast formation, but a single D_2 molecule is invisible with STM, therefore a larger amount of D_2 is needed.

While the tip was moved along the surface in the constant height, a set of voltage-dependent conductance spectra was measured above an area of 13×13 Å^2 on a grid of 64×64 points. The bias voltage was varied between -200 mV and 200 mV. The tip was placed over the center of the molecule with parameters $I = \ 100$ pA and $V = 316$ mV, so the initial tip-surface distance was set. The lock-in technique was used to measure the differential conductance dI/dV (modulation amplitude 4 mV, frequency 4.8 kHz). The experiment lasted 4 hours with switched off feedback. In the experiment, the total z-drift was 0.3 Å, which shows the high stability of the measuring equipment.

A typical spectrum recorded with a clean metal tip shows a smooth conductance curve without any peculiarities (see Fig. 5.1(a)). The spectrum was changed if the molecular deuterium sat on the tip. The $dI/dV(V)$ spectra reveal an abrupt change of the conductance(see Fig. 5.1(b)). The regions with different conductance are separated by a pronounced gap-like feature with an amplitude of spikes larger than the fluctuations of the signal. The spikes arise in pairs and are located around the zero bias symmetrically at $\pm U_s$, which signals an inelastic tunnelling process in the junction. The classical theory of the inelastic tunnelling predicts a step-like behaviour of the

conductance with respect to the bias. An inelastically tunnelling channel is opened or closed (see 1.2) which leads to the changes in the conductance. Inelastically tunnelling electrons can excite vibrational modes of the molecular D_2 and induce its motion out of the junction [171–173]. The structure of the junction changes. In our experiment at low bias, molecular D_2 sits in the junction while at high bias the junction is clean [80].
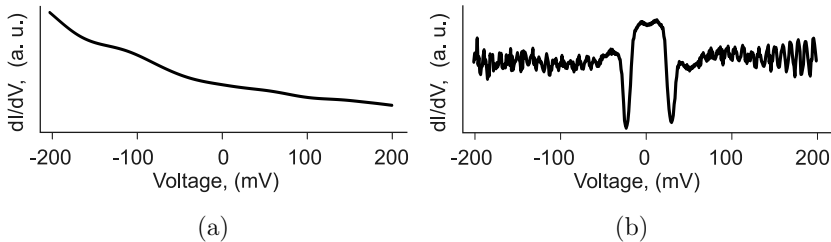
Figure 5.1: Conductance spectra over the layer of PTCDA (a) with a clean tip and (b) with the deuterium in the junction. In case of D_2 symmetrically located spike-like features are observed.

5.3 Two level systems

The conductance spectra measured with a tip decorated with H_2 (D_2) show spike-like anomalies. Although the spikes are regularly observed in the experiments with deuterium and hydrogen, the model that describes this physical process is still debatable. There are two models in the literature under discussion that describe the spike-like features in the conductance spectra. Both models suggest that the STM junction can be in different states.

Halbritter *et al.* [174] proposed a two level system (TLS) with two minimal energy states (marked with Ψ_L and Ψ_H) that are separated by a potential barrier (see Fig. 5.2(a)). The junction that is described with TLS has different conductance in each state, σ_L in the L-state and σ_H in the H-state. Direct transitions between the states occur owing to the inelastically tunnelling electrons that excite H_2 (D_2) in the junction. Spike-like behaviour can occur only if there is a strong asymmetry in the coupling between the states. The asymmetry can arise if the ground state L is non-degenerate and the excited state H is highly degenerate. In such case, $\gamma_L = N\gamma_H$, where N is the number of the degenerate H levels, γ_L is coupling of the electrons to the lower state of TLS and γ_H is coupling to the upper state. In other
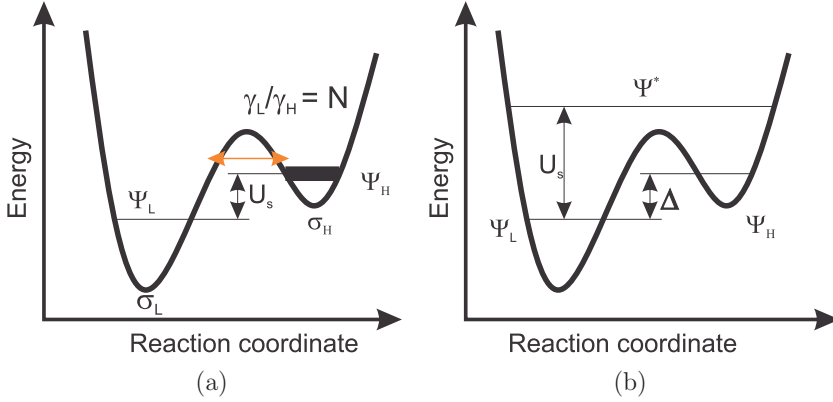
Figure 5.2:   (a) Schematic picture of D_2 transition between the states in (a) Halbritter model and in (b) Thijssen model.

words, once the particle is inelastically excited it cannot easily relax back. In the conductance spectra, this asymmetry leads to the appearance of the spikes at $\pm U_s$. According to this model, the voltage U_s is tied with the energy difference between these two states [175–177]. Halbritter *et al.* point out that the position of the spikes is not constant. It strongly depends on the amount of H_2 (D_2) and shows a broad distribution in the energy range of $30 - 100$ meV.

In the other model, Thijssen *et al.* [178] suggested a similar TLS model with two energy minima, also separated by an energy barrier, but with a different mechanism of transition between the states. The transition does not occur directly between the states Ψ_L and Ψ_H, but through the intermediate state Ψ^*. The H_2 molecule that is in state Ψ_L is first excited by an inelastically tunnelling electron to the state Ψ^*. Now it has enough energy to overcome the barrier and then relaxes to the state Ψ_H (see Fig. 5.2(b)). The coupling of tunnelling electrons to both states is considered to be equal. In this model, the spike voltage U_s is related to the energy difference between Ψ_L and Ψ^*. Using molecular controlled break junctions (MCBJ) with H_2, Thijssen *et al.* have found that the spike energy is observed near ≈ 42 meV, which relates to the transversal vibrational mode of H_2 in the junction, where the H_2 vibration is perpendicular to the current direction. Thijssen's experiments show an isotope shift of the spike positions. For D_2 the spike energy shifts by the factor $\approx \sqrt{2}$ and was observed at ≈ 29 meV, as expected for molecular vibration mode energies [179].

Non-linearities in the conductance spectra were studied also by Gupta *et al.* [180]. Metal surfaces covered with H_2 were investigated with STM. It was found that the bias at which the spikes were observed depends on the surface coverage of deposited H_2. The experiments with H_2 and D_2 show that it is not possible to distinguish between these two gases using STM. The coverage cannot be precisely measured, and therefore the dependence of the spike position on the coverage cannot be derived. The disagreement with results obtained with MCBJ can be due to the differences in the junction structure in the case of MCBJ and STM. Our experiments show that the spike position depends on the coverage of D_2 as in case of Gupta's experiments. Additionally, it was found that the spikes are sensitive to the surface area beneath the tip. From our experiments, it is not possible to distinguish which of the model, mentioned above, is preferable. We will keep to the concept of the two-level system where the junction can be in different states.

Our experiments show that one pair of spikes is always related to expelling of the H_2 or D_2 molecules from the junction. When there are two pairs of spikes, the one at the larger bias value is related to expelling. This fact was confirmed by the spectra and by the scan images taken at different biases [80]. The STHM contrast is observed only at the low bias, while at the high bias the structure of the conductance images coincide with the conventional STM contrast. The distance-dependent conductance spectra show an exponential behaviour at high bias and nonexponential behaviour at low bias where the scan images exhibit the STHM contrast.

The TLS model concept will be applied to the junction states to probe the surface. In general, the parameters of the TLS model depend on the tip, on the local surface area beneath the tip and on the state of D_2 in the junction. The STM tip remains unchanged during the scanning. The states of TLS are represented by a junction with and without D_2. Switching between the TLS levels provides information about desorption energy potential of D_2 from the surface. Therefore, the excitation energy of D_2 depends on the surface under the tip. The excitation energy can be monitored with the voltage-dependent conductance spectra.

5.4   Experimental results

5.4.1   Lateral dependence of conductance spectra

The spectra recorded in different points of the surface show high sensitivity of TLS on the surface properties. Above the PTCDA molecule (Fig. 5.3(b)), only one pair of symmetric spikes is observed. It shows that the junction can be in two states, Ψ_L and Ψ_H. The spikes at $U_s = U_{out} \approx \pm 35 - 40$ mV denote D_2 excitation out of the junction. The same is observed for negative bias. When the tip is above the intermolecular area (Fig. 5.3(a)), two pairs of transitions are observed. Consequently, there are two pairs of spikes, at $\pm U_s$ and at $\pm U_{out}$ and three states of the junction. Actually, we are interested in the spikes at $\pm U_{out}$, since at $\pm U_{out}$, the D_2 molecule is expelled from the junction. We are interested in the bias voltage needed the clean the junction. For the voltages $V < |U_{out}|$, the junction is filled. The spikes at $\pm U_s$ show that there is a process, in which the conductance of the junction changes but D_2 remains in the junction. The initial low-bias state Ψ_L switches to the Ψ_M state with different conductance.
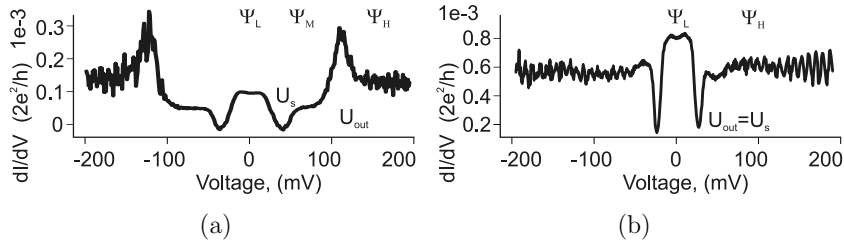
Figure 5.3: Conductance spectra measured (a) between the molecules and (b) above the molecule. Above the molecule, the junction can be in two states. Between the molecules a third state of the junction is observed. In Ψ_M, D_2 is present in the junction. The junction is empty in both cases at high bias (Ψ_H).

In Fig. 5.4 a set of the spectra measured along a line that connects the center of the PTCDA molecule and the middle point between two neighbouring molecules is presented. Only the two types of spectra that were described above are observed. The spectrum recorded on the border of the molecule separates spectra of these two types. The large noise level of the border spectrum reflects the instability of the junction on the edge of the molecule. The shape of the spectra clearly depends on the point of the surface. Note

that there are also clear differences between the spectra of the same type.
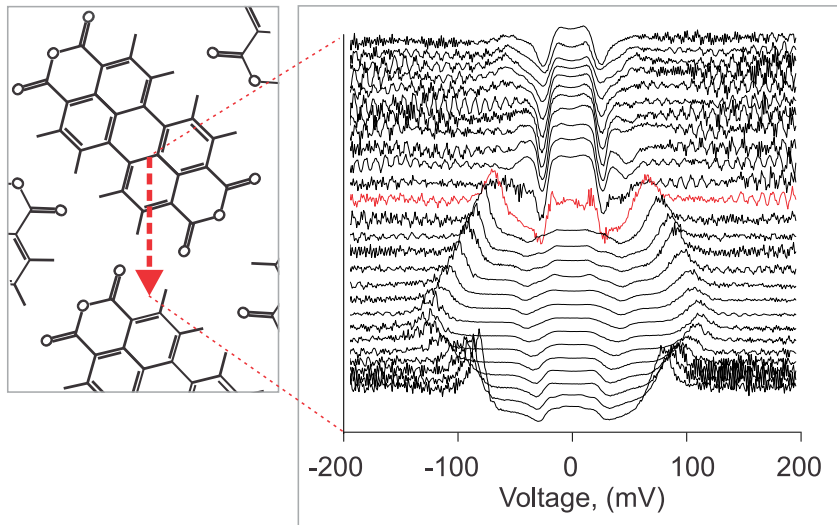
Figure 5.4: Set of conductance spectra measured along the path marked with red line. For better view all the spectra are shown with offset. The red one spectra corresponds to the point where the tip is over the edge of the molecule. Over the molecule two states of the junction are observed while between the molecules there are three states.

Above the molecule, the STS spectra show only one transition at $\approx 35 - 40$ mV, between the state Ψ_H and the state Ψ_L. D_2 can easily escape from the junction indicating that D_2 sits in a shallow potential well with a low escape barrier. The conductance spectra measured in between neighbouring molecules show two transitions and three states of the junction. The state Ψ_M arises between the states Ψ_L and the state Ψ_H only between the molecules. In the Ψ_M state, D_2 is still in the junction. The junction state switches to the new state Ψ_M at $U_s = \pm 35 - 50$ mV (see below). The escape of D_2 from the junction occurs at U_{out}. The values of U_s do not vary significantly, while values of U_{out} vary from 35 mV near the edge of the molecule and to 160 mV in the middle point between molecules. This can be understood in the following way: D_2 can be pushed into the gap between the molecules, because there is a room there. But D_2 cannot be pushed into the PTCDA because the average distance between the atoms of neighbouring PTCDA molecules is larger than the distance between the atoms of the same molecule. The movement of D_2

is restricted by the PTCDA molecules at the sides and, thus, the bias voltage
needed to expel D_2 is high between the molecules.

The excitation energy eU_{out}, at which D_2 escapes the junction, is plotted
in Fig. 5.5. The x and y denote coordinates of the tip position. The pattern
of the image shows several features. For tip positions above the molecule, the
pattern is reminiscent of the geometrical structure of PTCDA. In particular,
the areas related to the central and to the peripheral C_6 rings of PTCDA
are distinguishable. Here the value of eU_{out} is relatively small. eU_{out} is even
smaller above the internal bonds of PTCDA, including C−C bonds (marked
with (f)). The C_6 rings at the periphery (marked with (e)) have a bit larger
eU_{out} value than central C_6 ring (marked with (d)). This reveals that the
position of D_2 above the bonds and the central ring is less stable than the
position above the rings at the periphery.
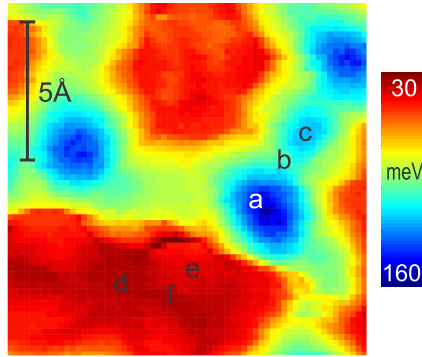
Figure 5.5: Map of eU_{out} for each (x, y) position of the tip. The characters
(a)-(f) mark the area positions discussed in the main text.

The variation of the eU_{out} values also exhibits a complicated pattern for
intermolecular (x, y) tip positions. There are large voids with three neigh-
bouring molecules, marked with (a) in Fig. 5.5 and the smaller voids with
two neighbouring molecules, marked with (c). Both regions have a common
border that coincides with the location of H−O hydrogen bonds between two
PTCDA molecules (marked with (b)). The maximum energy value of eU_{out}
is observed in the centers of the areas of types (a) and (c). eU_{out} drops sig-
nificantly above the borders (b) between these areas and above the molecule
border.

D_2 sits in a 3-dimensional potential well in the junction. This potential
well is the sum of the tip potential and the surface potential. The potential

created by the tip remains unchanged during the scanning, while the surface
potential varies from point to point on the surface and adds a perturbation
to the initial potential well of the tip. By mapping the excitation energy
along the surface, it is possible to obtain the information related to the local
adsorption potential of the D_2 molecules on the surface. It is interesting
to compare obtained information with the adsorption energy for the D_2-like
molecules. This will be done in section 5.5. However, before we turn to this
task, we are going to construct bias dependent maps from the spectra of the
present section and discuss the bias dependence of the imaging mechanism

5.4.2   Bias dependence of the STHM contrast

The STS spectra show that an escape of D_2 from the junction occurs at
U_{out}. At the bias $V > U_{out}$ the junction is empty and at the bias $V < U_{out}$ the
junction holds a D_2 molecule. For different points of the surface switching
occurs at different bias voltages U_{out}. At some biases both types of contrast,
STM and STHM contrast, should be observed in one image, depending on the
position. Rebuilding the conductance maps at the fixed biases, it is possible
to reconstruct the contrast conversion from STHM to STM. For low bias
voltage, the reconstructed images show the same type of corrugation as the
scan images recorded with the corresponding bias in the constant height
regime. An example of the image taken from [142] and reconstructed image
are in Fig. 5.6).   We note in passing that the possibility to reconstruct
STHM images from statically measured spectra rules out a contribution of
any dynamic effects, such as friction or stick-slip, in STHM image formation.

The evolution of the conductance scan images with respect to the bias
voltage applied to the junction is shown in Fig. 5.7. At $V = 5$ mV the
scan image shows STHM contrast (Fig. 5.7(a)) and at $V = 150$ mV the
contrast converts completely to the conventional STM contrast (Fig. 5.7(o)).
Figs. 5.7(b)-(n) show the intermediate steps of the contrast conversion from
STHM to STM.

At low bias, the STHM contrast is observed for intra- and intermolecular
areas, D_2 is present in the junction for all tip positions (see Figs. 5.7(a)-
(e)). According to the spectra, the transition to the state Ψ_H happens earlier
above the molecules. The breaking of the STHM contrast starts at the bias of
$V \approx 30$ mV at the edges of the molecules and then it propagates towards the
centers of the molecules along the bonds. Sharp lines, that denote chemical
bonds, blur and smooth out. First the central ring is blurred, the peripheral
rings after. In Figs. 5.7(f)-(i) we observe the change of the contrast for the
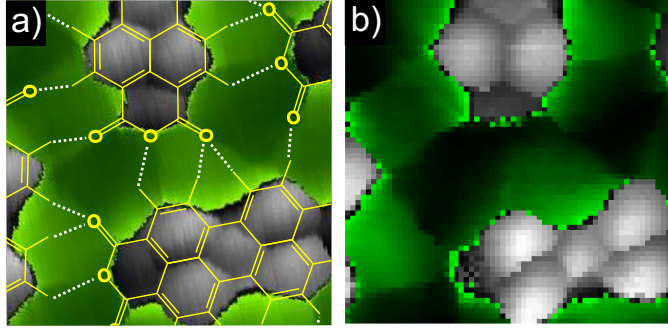
Figure 5.6:   PTCDA/Au(111), (a) STHM image recorded in the constant height regime, bias applied to the junction, V = -2 mV, taken from reference [142]. The backbone structure of PTCDA is superimposed over the picture. The size of the image is 1.3 nm × 1.3 nm. (b) The image of the PTCDA/Au(111) reconstructed from the set of the STS spectra discussed in section 5.4.1 at the bias of V = -2 mV.

peripheral rings. The geometrical structure of the molecules is not visible anymore starting from the bias $V \approx 50$ mV (Fig. 5.7(i)). For the position above the molecules the junction state is Ψ_H with no D_2 on the tip.

The initial STHM-like contrast between the molecules is retained still at $V \geq 50$ mV. According to the spectra, the junction here switches first into the state Ψ_M. Thus, we can conclude that the junction in state Ψ_M still has a D_2 molecule in it. Between the molecules switching from the STHM to the STM contrast is observed starting from the bias of $V \gtrsim 70$ mV. The blurring starts to propagate toward the intermolecular area along the hydrogen bonds (marked with yellow arrow in Fig. 5.7 (k)-(m)). We can see that the areas with the STHM contrast are separated from the areas with the STM contrast with borders of increased conductance (see Fig. 5.7(m)-(n)). The areas of STHM contrast are squeezing to the circular spots (is marked with red arrows in Fig. 5.7(n)) until they disappear completely at $V \approx 150$ mV. For the bias $V \gtrsim 150$ mV the whole image has the STM contrast.

The conductance profiles across the molecule and intermolecular area are quite different in case of the STM and the STHM contrast. Fig. 5.8 shows how the conductance profile (marked in Fig. 5.8 left panel with a red arrow) changes with respect to the bias and how the transformation from the STHM contrast to the STM contrast occurs. At $|V| < 35$ mV, the junction is in the state Ψ_L and the STHM contrast is observable. The junction is in state Ψ_L
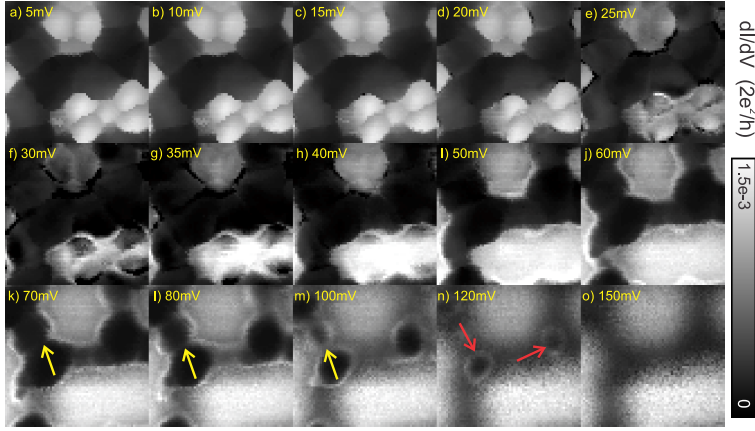
Figure 5.7: Slices extracted from the set of the conductance spectra at the different biases. Each picture shows the conductance map at the distinct constant bias. (a)-(e) STHM contrast of PTCDA/Ag(111). The geometrical pattern of the PTCDA molecules is observed. The contrast related to the hydrogen bonds is observed between the molecules. The junction is in the state Ψ_L. (f)-(h) STHM-like contrast, the junction is in state Ψ_M above the molecules and Ψ_H everywhere else. (i)-(n) The junction is in the state Ψ_H (empty junction) over the molecules. The STM-like contrast is observed, what is the sign that the junction is free of D_2. For the intermolecular area the junction is in the state Ψ_M. The STHM-like contrast is observed. Here D_2 sits in the junction. (k)-(m) The STM contrast is almost everywhere. The yellow arrows show the hydrogen bonds along which STHM contrast converts to the STM-like contrast. (n) The STM contrast is almost everywhere. The red arrows show last spot of the area with STHM contrast. (o) STM-like contrast of the PTCDA/Au(111).

and shows better sensitivity to the variations in the substrate. It shows an abrupt jump of the conductance between the tip position above the molecule and above the intermolecular area. At $|V| \approx 50 - 150$ mV the junction is partially in the state Ψ_H and in the state Ψ_M. The areas are separated by the spikes. The profile at the high bias ($|V| \geqslant 150$ mV) corresponds to the LDOS. The variation in the conductance values of the profile for STM contrast is smooth, with no abrupt jumps.
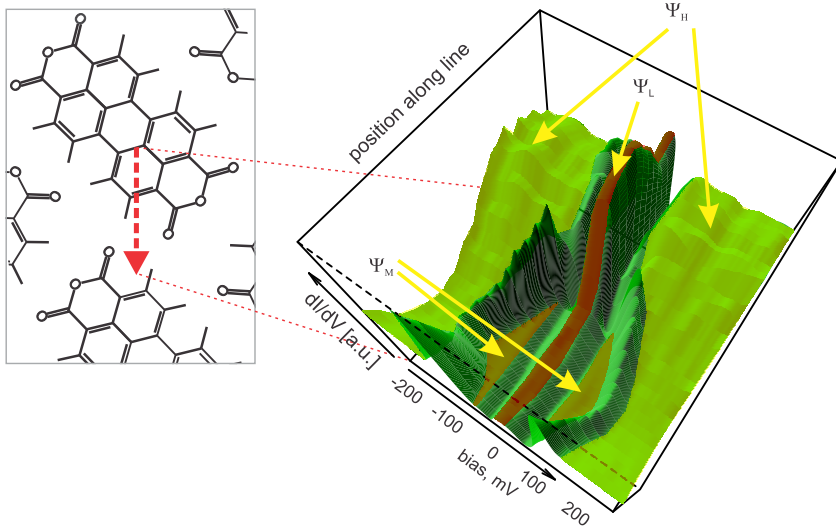
Figure 5.8: Set of conductance spectra measured along the path (red line). for $V \leq 35$ mV STHM contrast is observed. Junction is in state Ψ_L, for 35 mV $\leq V \leq 160$ mV mixed contrast is observed. Junction is in state Ψ_M and Ψ_H, for $V \geq 150$ mV STM contrast is observed. Junction in state Ψ_H is empty. Points related to the same state are highlighted with the similar colour.

5.5   Reconstruction of the D_2-surface potential

5.5.1   Force-field model

The mapped excitation energy of D_2 along the surface gives us the information related to the local adsorption potential of the D_2-like molecules on a surface. A force-field simulation was performed to analyse the structure of the junction and the behaviour of D_2 in the junction. D_2 sits in the junction in the potential well that is created by the superposition of the tip and of the surface potential fields.

$$U_{\text{total}} = U_{\text{s}} + U_{\text{t}}. \tag{5.1}$$

For the known field distribution, it is possible to calculate the work that is needed to switch the TLS from one state to the other by removing the D_2 molecule from the junction. Note, the adopted approach is consistent with the TLS approaches proposed by Thijssen and by Halbritter *et al.* [174, 178].

The D_2 escape out of the junction was treated as a displacement in lateral direction for at least 2 Å from the (x, y)-position of the tip. For this displacement the molecule will be far from the tip and the dominating part of the tunnelling current will flow directly from the tip to the substrate. This is reasonable since the size of D_2 is 1.4 Å [181].

To describe the interaction between the D_2 molecule and the tip with the surface a Morse potential was used. The Morse potential for two interacting atoms is a sum of two exponential functions.

$$U(r) = D_0(e^{-2a(r-r_0)} - 2e^{-a(r-r_0)}), \qquad (5.2)$$

where r_0 is a equilibrium distance and D_0 is a well depth. The parameter a is related to the width of the potential well. In this notation zero of energy is at $r \to \infty$. The first exponential in Eq. 5.2 describes a short-range Pauli repulsion and the second the long-range attraction.
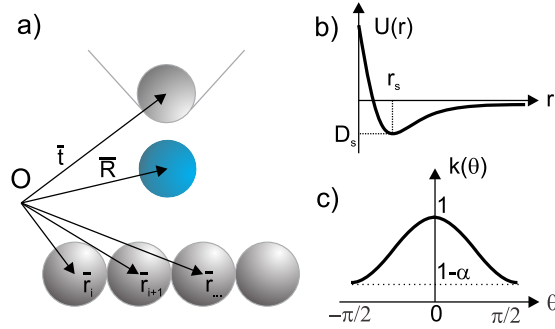
Figure 5.9: (a) Tip-D_2-PTCDA scheme. (b) Morse potential. (c) Angular coefficient $k_t(\theta)$.

The potential for the D_2 molecule in the junction is calculated by a pairwise summation over the Morse potentials between the D_2 molecule and all relevant atoms of the surface (the first term) and the tip (the second term),

$$U_{\text{total}}(\vec{R}) = \left(\sum_i^{\text{surface atoms}} U_a(|\vec{r}_i - \vec{R}|) \right) + U_t(|\vec{t} - \vec{R}|, \theta). \qquad (5.3)$$

The first term refers to the surface potential, $U_\mathrm{s}(r)$:

$$U_\mathrm{s}(r) = \sum_i U_\mathrm{a}(r), \tag{5.4}$$

where for each atom the Morse potential is written,

$$U_\mathrm{a}(r) = D_\mathrm{a} \left(e^{-2a_\mathrm{a}(r-r_\mathrm{a})} - 2e^{-a_\mathrm{a}(r-r_\mathrm{a})} \right). \tag{5.5}$$

The surface was represented as a PTCDA/Au(111) herringbone layer. The metal substrate was neglected, since its presence adds just a constant attractive background to the interaction. The size of the D_2 molecule was included through a Morse potential. The structure of D_2 molecule was neglected, it was represented as a spherical particle. Accordingly, the orientation of the molecule was omitted, but in principle it can be introduced also through the Morse potential by choosing fitting parameters of D_0, a, r_0 [165]. For a qualitative computation these simplification are reasonable.

The parameters of the Morse potential for the D_2-PTCDA interaction were determined from the assumption that the D_2 molecule sits in a potential well above the PTCDA molecule at the same distance as above a graphene layer. The Morse potential for D_2 (H_2) above the graphene layer is known from the literature: $r_\mathrm{GL} = 2.7$ Å, $D_\mathrm{GL} = 85$ meV [165, 182]. These parameters do not depend significantly on the orientation of the D_2 (H_2) molecule and on the different D_2 (H_2) positions above C atoms, the C−C bonds or the centers of C_6 rings. In case of PTCDA layer, the Morse potential for each atom, U_a, was chosen identical. U_a with values $r_\mathrm{a} = 3.5$ Å, $a_\mathrm{a} = 1$ Å^{-1}, $D_\mathrm{a} = 4.5$ meV add up to a Morse potential of the layer, U_s, with $r_\mathrm{s} = r_\mathrm{GL}$, $D_\mathrm{s} = D_\mathrm{GL}$, how it is in case of graphrene layer. The parameter a_a was chosen from the lower limit values used in the literature $(1-1.5$ Å$)$ [165, 183, 184]. A potential energy landscape map for a particular z-distance has sharper contrast for large a_a and is blurred and smoothed for small a_a. However, the map pattern remains unchanged. Note that the parameter a_a is important for the longitudinal vibration of the D_2, the movement along the current flow direction, which was not considered in the calculations. For the Morse potential, the equilibrium distances r_a in case of D_2 and H_2 can be taken equal [185–187].

The tip was represented as a single atom and was simulated with the modified Morse potential.

$$U_\mathrm{t}(r,\theta) = D_\mathrm{t} \left(e^{-2a_\mathrm{t}(r-r_\mathrm{t})} - 2e^{-a_\mathrm{t}(r-r_\mathrm{t})} \right) \times k_\mathrm{t}(\theta). \tag{5.6}$$

The parameters were chosen considering that the distance between the D_2 (H_2) and the Ag atom is 1.9 Å [179, 188]. The well depth D_t of the Morse

potential for the tip was chosen $10 - 50\%$ larger than the depth D_s of the potential well for the surface ($D_t = (1.1 - 1.5) \times D_s$), because D_2 prefers to sit in the potential well near the tip. At the same time the well depth D_t should be not too large because the STHM experiments show that the D_2 molecule can easily jump away from the tip. An additional modification of the tip Morse potential was an introduction of an angular dependence (see Fig. 5.9(c)),

$$k_t(\theta) = 1 - \alpha \sin^2(\theta), \text{ where } 0 \leq \alpha \leq 1, \tag{5.7}$$

where θ is the angle of deviation from the z-direction (z axis is perpendicular to the surface plane), α is a parameter related to the stiffness of the D_2-tip bond. The angular dependence reflects the fact that the D_2 molecule sits near the tip apex. The parameters a_t and $k_t(\theta)$ are related to the spatial size of the 3D potential well near the apex of the tip, where the D_2 molecule sits. To summarise, the Morse potential of the tip has the initial parameters: $r_t = 1.9$ Å, $a_t = 1$ Å^{-1}, $D_t = 112, 5$ meV, $\alpha = 0.5$.

5.5.2   Energy maps

The total potential energy field consists of the superposition of the potential fields generated by the tip and by the PTCDA layer. It is clear that the proximity and the mutual position of the tip and the surface affect the shape of the potential well. In particular, potential well depth and the work needed to expel D_2 changes depends on both the tip and the sample.

Putting the tip in a different position above the PTCDA layer we can calculate a deformation of the potential well (see Fig. 5.10). For every tip position E_{min} and its (x, y, z)-position were calculated. The energy needed to expel D_2 out of the junction is $\Delta E \simeq eU_{out}$. We also have evaluated the vibrational energy $\hbar\omega$ and the number of the levels N in the well. The number of the levels in the well is needed to evaluate the consistency of our model.

The calculations were performed for different values of r_a, r_t, D_a, D_t, a_a, a_t, α. The calculations have shown that if the tip-surface distance is less than the sum of equilibrium distances of Morse potential for the tip and for the surface then the map of an excitation energy ΔE is comparable to the map of eU_{out} obtained from experiment (see below),

$$l_{t-s} < r_s + r_t. \tag{5.8}$$

For such distances l_{t-s} only the short-range repulsion part plays an important role. The small values of a_t, a_a and α add blur to the images and do not
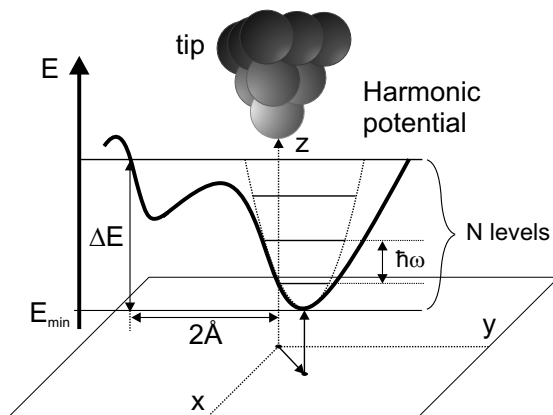
Figure 5.10: Scheme of the potential well in the vicinity of the surface. The tip position is (x,y,z), $E_{\min}$ is the energy value of the potential well, ΔE is the work needed to move the particle away by 2 Å, $\hbar\omega$ is the vibrational energy, N is possible the number of levels in the harmonic potential well.

affect on the image structure.   For the contrast shape analysis the ratio between D_a and D_t is important. The values of D_a and D_t can be easily rescaled to match the measured excitation energy.

Fig. 5.11 shows energy maps calculated using the force field model introduced in the previous section. The parameters of the calculation for the figures in this section are the following: for the tip equilibrium distance is 1.9 Å and $D_t = 110$ meV, for the PTCDA equilibrium distance is 2.7 Å and $D_s = 85$ meV, the tip-PTCDA distance is 3.75 Å, $\alpha = 0.8$.

If only the potential $U_s(r)$ is calculated, there are two types of the potential wells created by PTCDA layer. The first type has the energy $E_{\min,1} = -85$ meV and is located above the center of the PTCDA molecule at the distance of 2.7 Å above the molecules' plane. This well was used to adjust the starting parameters for our model. The second type of the potential well is closer to the PTCDA layer (≈ 2.1 Å) and is located above the intermolecular area with three neighbouring PTCDA molecules and has $E_{\min,2} \approx -160$ meV. However, if we add the tip, the absolute minimum of the potential energy $U_{\text{total}}(r)$ will be in the near the tip apex independently from the tip position,

The map of $E_{\min}$ is in Fig. 5.11(a). Let's look first when the tip is above the intramolecular area. The potential well for D_2 is deeper when the tip position is above the central C_6 ring of PTCDA than above peripheral C_6

rings. This is a consequence of the symmetry of the PTCDA molecule. The potential created by a single PTCDA molecule has its absolute minimum above the central C$_6$ ring. But there are also local potential minima above the peripheral C$_6$ rings. However, the well depth here is not deep, since the contribution from the far atoms of the same PTCDA molecule is significantly less. The neighbouring PTCDA molecules are even further away and add almost no contribution.
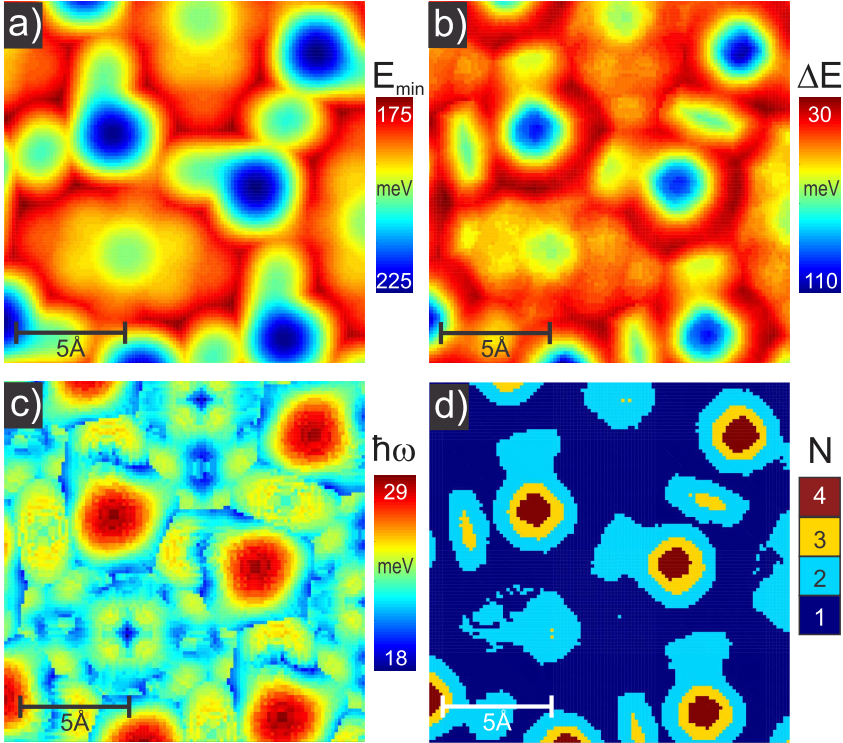
Figure 5.11:   (a) The map of energy values of the potential well bottom, E_{min}, for every tip position. (b) The work ΔE needed to move the particle away by 2 Å. (c) vibrational energy $\hbar\omega$. (d) An approximate number of levels N in the well. The x and y axes denote the lateral (x, y) position of the tip.

The work ΔE needed to expel D$_2$ from the junction (excitation energy for transition $\Psi_L \rightarrow \Psi_H$) is shown in Fig. 5.11(b). This plot is based on the potential $U_{total}(r)$. When the tip is above the molecule ΔE is relative low,

because the D_2 molecule is squeezed in the junction in a shallow potential well and can easily move sideways. When the tip is above the intermolecular area, the tip pushes D_2 into the layer. D_2 sits in a deep potential well. Therefore, D_2 movement is restricted. The work needed to expel D_2 out of the junction will be up to 4 times larger than when the tip is above the molecule. The least stable positions of D_2 are when the tip is above the edge of the PTCDA molecule.
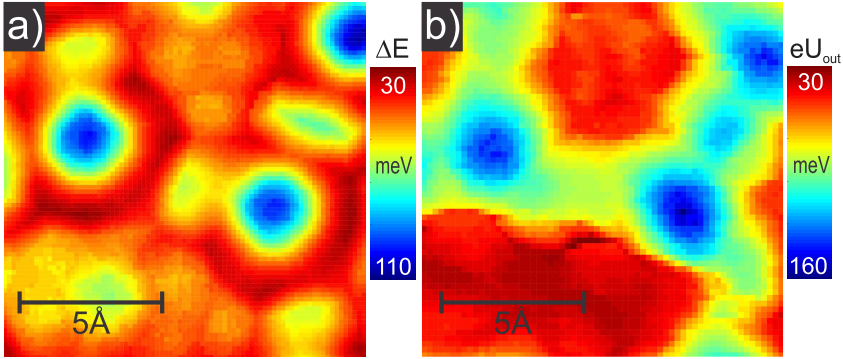
Figure 5.12: (a) Excitation energy of D_2 out of the junction obtained from the calculations Fig. 5.11. (b) Excitation energy of D_2 out of the junction obtained from the experiment.

The excitation of D_2 out of the junction is due to the D_2 oscillations in the junction. Thijssen [178] and Halbritter [174] associate the escape with the excitation of the transversal mode of D_2 oscillation in the junction where D_2 oscillates perpendicular to the current flow direction [174, 178, 179]. To estimate vibrational frequencies and the number of levels in the well, we approximate the potential energy with a 2D harmonic well in (x, y)-plane around the point of $E_{\min}$. Fig. 5.11(c) and (d) show the vibrational energy $\hbar\omega$ and the number of levels in the potential well. The harmonic well is good only to estimate the ground state. The vibrational energy varies from 18 to 29 meV what is in agreement with 29 meV reported in the literature [179]. For tip position above the molecule, there are one or two vibrational states. Between the molecules the number of levels can rise up to 4 for the deepest potential wells.

The number of the states does not vary significantly for the different computational parameters (r_a, r_t, D_a, D_t, a_a, a_t, α). The calculations show reasonable numbers of the states in the well. Comparing with experiment,

there should be 1 or 2 states in the potential well. Note that, for the higher states, the harmonic approximation is not adequate and can give incorrect values because the real shape of the potential wells will be anharmonic. The levels in an arbitrary anharmonic potential, however, cannot be easily calculated. The excitation energies obtained from the calculations are consistent with the numbers observed in the experiment (see Fig. 5.12).

The calculated excitation energy ΔE for the transition $\Psi_L \to \Psi_H$ (Fig. 5.11(b) and 5.12(a)) shows the same order of magnitude and has a very similar spatial pattern as observed in experiment (eU_{out} Fig. 5.12(b)). The energy needed to expel D_2 is $\Delta E \sim 100$ meV if the tip is positioned above the intermolecular area. The tip position close to the PTCDA edge decreases the stability of the junction and D_2 can easily move away ($\Delta E \sim 30$ meV).

5.5.3   Displacement of D_2 in the junction

In Figs. 5.11 and 5.12 we plotted characteristic parameters of the potential energy landscape of a tip-suspended D_2 molecule: binding energy E_{min}, work ΔE required to move the particle 2 Å away from the tip (excitation energy for transition $\Psi_L \to \Psi_H$), vibrational energy $\hbar\omega$ and number N of vibrational levels.   The x and y coordinates in the maps are the lateral coordinates of the tip position.   However, it is clear that due to deviation of the potential energy landscape from two-, three-, four-, six-fold or even cylindrical symmetry the actual position of the D_2 molecule can actually be more away from the tip position despite of the restoring forces included into the tip-D_2 Morse potential. In this section we analyse the lateral and vertical position of the D_2 molecule relative to the tip for all lateral tip positions, as these parameters will influence the tunnelling current through the junction.

The equilibrium position of the D_2 molecule can be described with the following parameters: a lateral shift d, a D_2-PTCDA surface distance Z, a tip-D_2 distance R (see Fig. 5.13). The values of these parameters for different tip position are shown in Fig. 5.14 The tip-PTCDA surface distance can be expressed with these parameters as

$$l_{t-s} = R\cos\theta + Z, \tag{5.9}$$

with the tilting angle θ given by

$$\sin(\theta) = \frac{d}{R}. \tag{5.10}$$
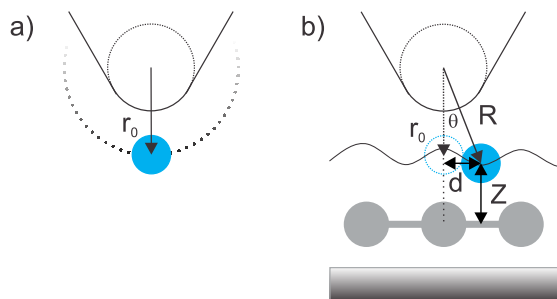
Figure 5.13: (a) Schematic picture of unperturbed position D_2 on the tip. r_0 is the position of D_2 in the potential field U_t of the tip. (b) D_2 displacement on the tip in the vicinity of the surface. R is a position of energy minimum of U_{total}. Z is a distance to the surface. d is a lateral shift of $E_{\min}$ from the tip (x, y) position.

The lateral shift d (see Fig. 5.14(b)) shows that the maximum value is observed for tip positions above the borders of the PTCDA molecules, where D_2 feels the repulsive forces from the atoms mainly from one side, and above the atoms and bonds where the repulsion rises faster, according to the Morse potential.

The direction of the lateral shift of equilibrium position of the D_2 molecule with respect to the tip position is shown in Fig. 5.15(a) with small blue arrows. The figure has clear tile pattern where the tile borders are plotted with white lines.   Arrows on opposite sides of the border point in the opposite directions. When the tip is above the tile, the force acting on the D_2 molecule directs it to the center of the tile. The positions of the tile edges are in a good agreement with the positions of the intramolecular and intermolecular bonds. The tile vertexes coincide with the positions of the atoms of the PTCDA molecules in the layer.   The histogram of D_2 position distribution (Fig. 5.15(b)) allows us to come to the same conclusions. This tells that D_2-sensor is sensitive to the hydrogen bonds as was proposed before [142].

However, there are complicated situations when two bonds are located close to each other. In this case we do not see an additional tile between them. There is only one border that is shifted towards the shorter bond. For the two bonds of length 1.9 Å and 2.2 Å (marked with yellow arrows in Figs. 5.15(a) and 5.16), the tile border is near the bond with the length of 1.9 Å. The closer two atoms are located the stronger is repulsion. Therefore
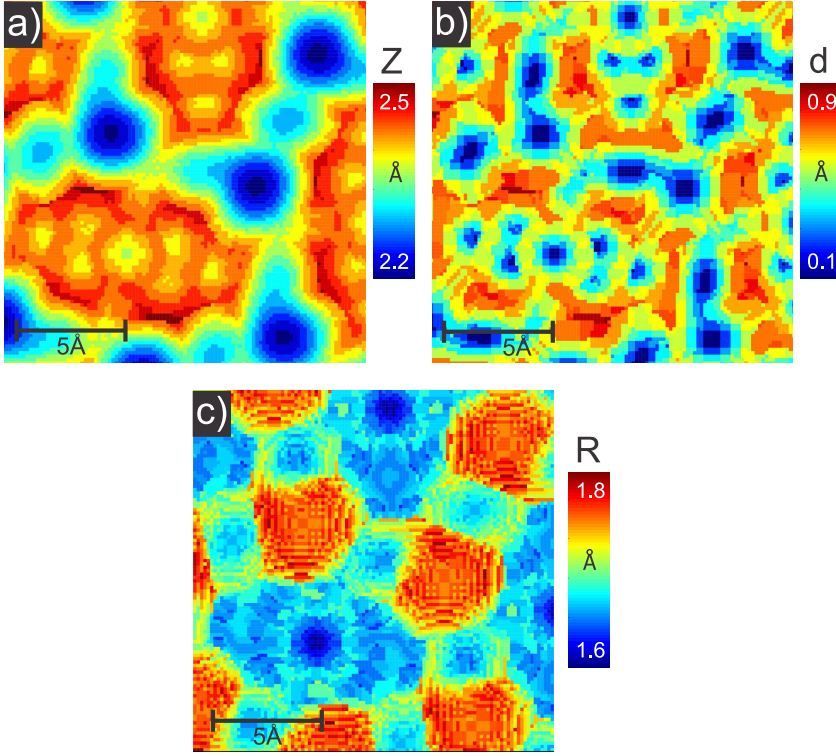
Figure 5.14: (a) z-position of the energy minima. (b) Magnitude of lateral shift of the energy minima from the tip position (x, y). (c) Distance between the PTCDA layer and D$_2$ molecule. z, R, D are depicted in Fig. 5.13.

above the shorter bond the repulsion grows faster than above the longer bond. This effect is observable in experiment and in calculations. That is why the border is shifted away from the longer bond.

In case of PTCDA/Au(111) for the intermolecular area the edges of the tiles coincide with the hydrogen bonds between the neighbouring molecules. PTCDA molecules form "herringbone" structure that is very close to the [102] plane of the bulk structure of the PTCDA crystal. This shape is due to the stronger intermolecular interaction than the interaction with the Au substrate. Intermolecular interactions are represented by hydrogen bonds between the neighbouring PTCDA molecules. For "herringbone" structure they are shorter than any other intermolecular bonds and distances.
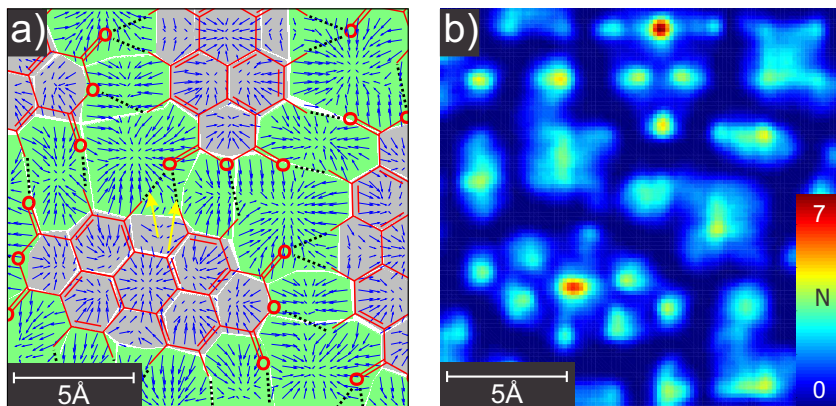
Figure 5.15:   (a) Tiled structure of the map. White lines denote the borders between the tiles. Small blue arrows show the directions of the lateral shift of the position of $E_{\min}$. The magnitude of the arrow is shown in proportionality with a displacement. The backbone structure (red) of PTCDA is superimposed over the picture. Hydrogen bonds are plotted with black dotted lines. (b) Histogram of the positions of D_2 attached to the STM tip during the scanning. N shows how many times D_2 is in a position (x, y).
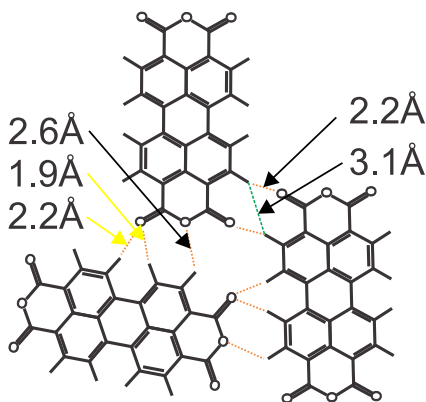
Figure 5.16: Scheme of PTCDA/Au(111) "herringbone" phase with marked distances.

The parameter R, the tip-D_2 distance, depends on how dense atoms of PTCDA are under the tip (see Fig. 5.14(c)). If the density of the atoms is

small (as in case of the intermolecular area) then the net force acting on the D_2 molecule is also small and the R value varies hardly from its unperturbed value $r_0 = 1.9$ Å. D_2 is pushed by the tip into the PTCDA layer. Above the borders of PTCDA, where d value is large, R value changes only slightly, since D_2 moves circumferentially around the tip apex and try to keep the same tip-D_2 distance. A big change of the value R are observed above the areas with high density of the atoms, where the lateral movement is restricted (above the molecules, but not above the edge of the molecule). Generally speaking, D_2 sits in an imaginary pyramid with base vertexes in surface atoms and top in the atom of the tip apex. D_2 turns to be squeezed between a tile formed by atoms from below and the atom of the tip from above. The force acting on D_2 moves it downwards and to the center of the pyramid base. The larger the pyramid base is, the stronger D_2 is pushed toward the base and the less the R varies. This is very well observed in case of the tiles belong to the intermolecular area.
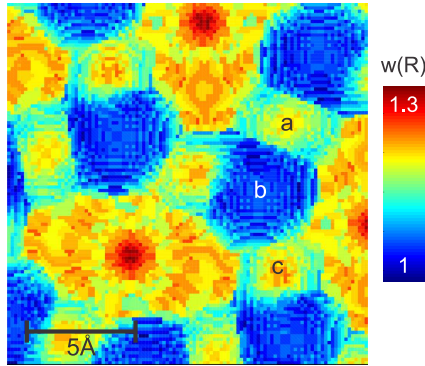
Figure 5.17:   Distribution of the value $w(R)$ derived from tip-surface distance. The structure of intermolecular part of the image is identical to the intermolecular structure of the STHM scan image.

Remarkably, for such configuration the image of the value

$$w(R) = \frac{\exp(-R)}{\exp(-r_0)} \tag{5.11}$$

will resemble and coincide with the STHM-like contrast of the intermolecular area in the STHM experiments (see Fig. 5.17). This quantity shows large values of the conductance above the molecules and above some intermoleculars tiles. $w(R)$ is normalized to the value of the D_2 position r_0 and follows

the rule how tip's LDOS changes with distance. Using for $w(R)$ the same logic that was described above, we will obtain that the magnitude of $w(R)$ is small for the large tiles (mark (b) in Fig. 5.17), and large for the small tiles (mark (a) and (c) in Fig. 5.17) and the molecules. Abrupt borders are due to the strong repulsion from the bonds and large shift of the D_2 molecule to the center of one of the tile. Such $w(R)$ behaviour for the intermolecular area is clearly observed for a wide range of the computation parameters. In case of the intramolecular areas $w(R)$ cannot be clearly linked to the STHM contrast. The variation of $w(R)$ over the molecule is weak and does not show clear profile. The corrugation pattern depends on the parameters of the calculation. The parameter Z also does not show visual picture for the intermolecular structure in case of the STHM contrast. Unfortunately, the current model cannot give an answer how the intramolecular contrast is formed.

5.5.4   PTCDA/Ag(110)

STHM is capable to image local, noncovalent intermolecular interactions, such as hydrogen bonds, in two-dimensional molecular layers [142]. In the STHM pattern of the PTCDA/Au(111) layer, a remarkable coincidence is observed between the lines that connect oxygen atoms on one molecule to adjacent hydrogen atoms on neighbouring molecules and the positions at which hydrogen bonds are expected. The proposed in section 5.5.1 model imply that lines are actually related to the shortest connections between atoms of neighbouring molecules. In case of PTCDA/Au(111) the shortest connections between neighbouring PTCDA molecules coincide,in fact, with the O−H bonds (see Fig. 5.16). But, in general case, this can be not true.

We want to propose that for STHM experiments with PTCDA/Ag(110) O−H bonds should not be observed. PTCDA/Ag(110) adsorbs flat [28] on Ag(110) in the "brickwall" commensurate phase [189] where molecules are facing each other with anhydride groups. The unit cell contains only one PTCDA molecule. A configuration of this phase is due to the strong interaction with substrate. PTCDA molecules are oriented on substrate perpendicular to the Au rows and then assemble into islands forming hydrogen bonds (see Fig. 5.18 marked with orange). There are two types of O−H bonds with lengths of 3.3 Å and 2.7 Å. But the shortest connection is actually H−H that is 2.3 Å (see Fig. 5.18 marked with blue line). According to the proposed model, in place of the H−H connection position we should observe a line in the STHM contrast.
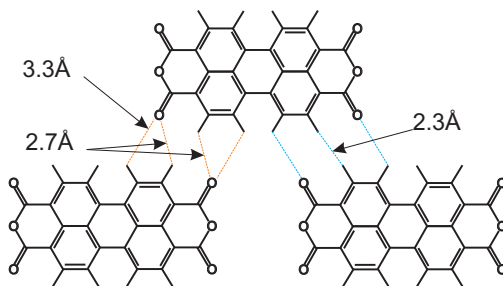
Figure 5.18: Scheme of the PTCDA "brickwall" phase on Ag(110). Hydrogen bonds are marked with orange dotted line. Blue dotted lines are expected in STHM contrast.

Unfortunately, there is no direct experiments with H_2 or D_2 to prove the statement. But based on the discussion in chapter 3 the intermolecular contrast in case of D_2 (H_2) and in case of Xe should coincide. This has been shown for PTCDA/Au(111), and it is expected to be true also for PTCDA/Ag(110). Fig. 5.19 shows STHM-like contrast of PTCDA/Ag(110) obtained with STM tip decorated with Xe atom. A scan image is recorded in the constant height regime with tunnelling parameters $I = 1.0$ nA and $V = -10$ mV. The scan image coincide with a scan shown in Fig. 1(h)-(j) in [80]. In case of Xe three lines are observed between the neighbouring PTCDA molecules. As the model predicts, the bright central line coincides with the H−H connection. Additional sidelines are not very well observed.

5.6 Conclusions

The experiment has shown that the voltage-dependent conductance spectra, recorded with a tip decorated with D_2 (H_2), depend strongly on the tip position above the surface. The spectra show spike-like features that denote excitation of D_2 (H_2) out of the junction. Measuring spectra in many points over the surface and taking slices at particular bias it is possible to reconstruct the conductance scan images for the same bias. The analyses of these scans have shown laterally inhomogeneous transformation of the STHM contrast into the STM contrast. For some positions D_2 (H_2) is restricted to move and therefore the STHM contrast survives longer. The possibility to reconstruct STHM images from statically measured spectra rules out dynamic effects, such as friction or stick-slip, in STHM image formation.
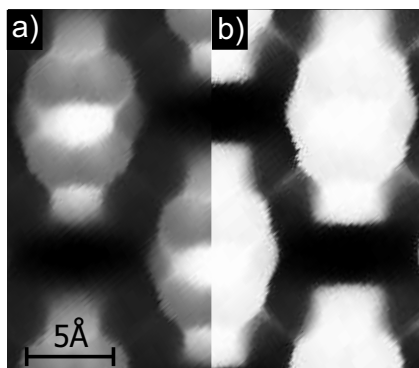
Figure 5.19: (a) PTCDA/Ag(110), STHM-like contrast obtained with Xe decorated tip in the constant height regime. (b) PTCDA/Ag(110), STHM-like contrast. Enhanced contrast for better view of intermolecular contrast structure.

The state of the junction depends on the position of the tip and on the bias applied to the junction. The transition between the states happens when the D_2 (H_2) is excited out of the junction by an inelastically tunnelling electron. For high bias, the junction is empty and have one state. And it can be one or two low-bias states where D_2 (H_2) sits in the junction. The reconstructed constant height images show that for all states with D_2 (H_2) in the junction, the STHM contrast is observed. The condition of D_2 (H_2) does not affect the STHM contrast.

The TLS concept was applied to the junction states. Junction TLS was used to probe the surface. Moving the tip in the constant height regime above the surface and mapping the energy of the excitation of the D_2 (H_2) out of the junction we have obtained the information that is related to the adsorption energy of the D_2-like molecules. To simulate the process of the D_2 excitation out of the junction, a force-field model was introduced. The excitation energy obtained in calculations was found to be in a good agreement with the experiment results. Furthermore, under the proposed model the analysis of the displacement of D_2 on the tip shows a correlation between the intermolecular STHM contrast and the D_2-tip distance. The model predicts that the lines, observed in the experiment and connect the molecules, are related, actually, to the shortest line segments with endpoints in the atoms of the adjacent molecules. And, in the general case, it is not necessary that these line segments coincide with the intermolecular bonds what was

proposed earlier. This force-field model despite its simplicity gives interesting and important results that allow us to understand the formation of the STHM contrast better.

Chapter 6

Summary and Outlook

Direct imaging of the inner structure of molecules has always been the challenge for the surface science. Scanning probe methods with decorated tips show that they are a powerful instrument for surface studies. An application of complex probes like a tip with an attached single molecule or a single atom allows to get an image of the surface with atomic precision. Due to the new physics involved in the tip surface interaction new details about the surface properties can be obtained. The decorated STM tips can be sensitive to the structure of the substrate, what means it could be used to describe the geometrical structure of the molecules and what can be useful for the chemical and physical characterisation of the molecules.

6.1 Main results of the work

In the first part of the thesis it was reported that the individual Xe atom or the single CO or CH_4 molecule adsorbed on the STM tip apex create a microscopic single particle sensor that simultaneously performs the function of an atomic-scale force sensor and a signal transducer, which couples the short-range force acting on the tip to the tunnelling conductance of the junction Experiments with new gases have shown unambiguously that a single particle plays role for structural contrast formation. Single molecule sensors demonstrate geometrical resolution of the surface similar to the STHM resolution that was achieved previously with hydrogen or deuterium. The mechanism of the submolecular geometrical contrast resolution does not depend on the details of the sensor particle or its interaction with a tip what points out that it should be a general physical phenomenon. The single particle sen-

sors can be characterized with a sensitivity range, which shows how deep the sensor can probe the surface beneath them. This characteristic is important because it helps to choose the proper sensor to study the particular surface.

In the second part of the thesis, it was reported that the structural contrast of the surface can be obtained simultaneously in the conductance and the force channels. The particle decorating the tip simultaneously performs the function of the atomic-scale force sensor and the transducer which couples the short-range force acting on the tip to the tunnelling conductance of the junction. The coupling between the force and the conductance was observed and discussed. On the basis of the experimental data, two distinct coupling regimes are identified. In the first regime, the coupling show linear dependence and the force sensor-transducer function can be calibrated quantitatively. In the second regime, the coupling has an irregular complicated character, which depends on the shape of the tip.

In the third part of the thesis the voltage-dependent conductance spectra recorded with the STM tip decorated with D_2 have been discussed. The experiment performed on the "herringbone" phase of PTCDA/Au(111) has shown that the STM junction can switch between different states, owing to the excitation of the D_2 molecule out of the junction by inelastically tunnelling electrons. Due to this property, the STM junction was considered as a TLS that can be used to probe the surface. The variation of the energy needed to expel D_2 from the junction is related to the geometrical structure of the surface and hold the information about the excitation energy of D_2 from the surface. The excitation energy calculated using a force-field model was found to be in a good agreement with the experiment results. The analysis of the displacement of D_2 on the tip have shown a correlation between the STHM contrast of the intermolecular area of the PTCDA layer and the variation of the D_2-tip distance. According to the model, the lines between the molecules are related to the shortest connections between the atoms of the adjacent molecules. And, in the general case, this line can not coincide with the intermolecular bonds as it was proposed earlier.

6.2   Future development

The imaging of the surface with the tip gives the information about the processes occur on the surfaces. Such methods will be important for study the chemical reactions on the surfaces and a single molecule chemistry. It makes possible to see how reactions proceed on surfaces and define products by

scanning the surface with the tip. There are some reported examples obtained with NC-AFM where the functionalized tip was used to define the structure of the unknown molecules [79] or to study the single molecule chemical reaction [190]. In such a case an application of the STM with a functionalized tip can give solutions of such a kind of the problems with much less effort.

All the main experiments have been performed with PTCDA molecules. The layer of PTCDA has complicated structure that depends on the surface. Experiments with PTCDA have shown that it is possible to use STM tip for chemical characterization of the surface. The numerical calculations for the PTCDA are quite complicated. Nevertheless, simple models of the complicated objects give a good result. For further study it is necessary to switch to the simple objects that are very well investigated and more precise models. Simple objects can be calculated with much less effort and gives more profound understanding of the physical phenomena, which plays here the role. A couple of steps were made in this direction. The STM tip decorated with CO and with Xe molecule was used to obtain scans of the layers of xenon and sodium chloride. For these simple objects, an interesting and sophisticated contrast corrugation of the image was observed. It was found that the contrast shape strongly depends on the tip-surface distance. A layer of xenon or sodium chloride can be calculated with the modern tools to get results which can make a big contribution of the understanding of the STHM-like geometrical contrast formation. This knowledge opens new horizons in surface science and gives understanding for the further application of functionalized tips.

Appendix

Program code

Program code listing of the routine to calculate potential energy for tip-surface system for chapter 5. Code is written for Octave/MATLAB.

```
1 # Plot the U_total field distribution
  # Routine for calculating Morse potential for PTCDA layer and the tip
  # Routine for calculation the displacement of the D2 position

  # prepare the memory for calculations
6 close all;
  clc;
  clear all

  ####################################################################
11 # function description part
  ####################################################################

  function [areax, areay, areaz] = prepare_space(z)
  # describe the area of interest for calculation
16 # define the center of area
   areaCenterCoord = [0,-8.5];
  # define width and length of the area
   areaSize = [1,1]*20;
  # define starting z-distance above the PTCDA layer
21 areaHborder = [0.1,z];
   areaBorderPos = 1/2*[areaSize',areaSize']*diag([-1,1])+\
    [areaCenterCoord' , areaCenterCoord'];
  # number of grid points
   x_points = 101;
26 y_points = 101;
   z_points = 101;

   listx = linspace(areaBorderPos(1), areaBorderPos(3),x_points);
   listy = linspace(areaBorderPos(2), areaBorderPos(4),y_points);
```

```
31  listz = linspace(areaHborder(1), areaHborder(2),z_points);
     [areax, areay, areaz] = meshgrid(listx, listy, listz);
    endfunction

    # STM tip is implemented as single atom with a charge on it
36  # charge part is not used for calculations
    function [charges, qQ] = create_tip(x,y,z)
     charges = [x, y, z]; # coordinates of charge [x, y, z]
     qQ = [0]; # values of charges in colon (is not used)
    endfunction
41
    # create layer of PTCDA
    # mol_num - order of further neighbour
    # Prepare to read the file PTCDA_HB.hin with description of
    # the unit cell of PTCDA/Au(111)
46  function [charges, qQ] = create_PTCDA_hb_layer(mol_num)
     fid = fopen("PTCDA_HB.hin");
     rrline = fgets(fid); rrline = fgets(fid); rrline = fgets(fid);

    # load atom position of two molecules of one unit cell from the file
51  for molnum = 1:2,
      rrline = fgets(fid); rrline = fgets(fid);
      for ii = 1:38,
       rrline = fgets(fid);
       ns = findstr(' ',rrline);
56     for i3 = 6:9,
        met(ii+(molnum-1)*38,i3-5) = \
        str2num( rrline( [ns(i3)+1 : ns(i3+1)-1] ) ) );
        end;
       end;
61  end
    # read and load translation vectors
     rrline = fgets(fid);rrline = fgets(fid);rrline = fgets(fid);
     ns = findstr(' ',rrline);
     rv = diag(ones(6));
66  ii = 1;
     for i3 = 1:2,
      rv(ii) = str2num( rrline( [ns(i3)+1 : ns(i3+1)-1] ) ) );
      ii = ii+1;
     end
71  rrline = fgets(fid);
     ns = findstr(' ',rrline);
     for i3 = 1:2,
      rv(ii) = str2num( rrline( [ns(i3)+1 : ns(i3+1)-1] ) ) );
      ii = ii+1;
76  end;
     rrline = fgets(fid);
     ns = findstr(' ',rrline);
     for i3 = 1:2,
```

```
    rv(ii) = str2num( rrline( [ns(i3)+1 : ns(i3+1)-1] ) ) );
81   ii = ii+1;
    end;
    fclose(fid);
    shiftVec = [rv(3)-rv(1), rv(4)-rv(2) ; \
     rv(5)-rv(1), rv(6)-rv(2) ]'*1;
86  qQNa = [];
    chargesNa = [];
    cellNum = mol_num;

   # create a layer of PTCDA consisted of (2*cellNum+1)*(2*cellNum+1) unit cells
91  for ii = -cellNum:cellNum,
    for jj = -cellNum:cellNum,
     aaa = [met(:,2:3)+\
       [(shiftVec*[ii;jj])(1)*ones(size(met)(1),1), \
       (shiftVec*[ii;jj])(2)*ones(size(met)(1),1)], \
96     met(:,4)];
     qQNa = [qQNa, met(:,1)'];
     chargesNa = [chargesNa; aaa];
    end
    end
101 qQ = qQNa;
    charges = chargesNa;
    endfunction

   # calculate Pauli repulsion potential and gradient for every point
106 # of the grid for PTCDA layer
    function [U, Ex, Ey, Ez] = \
      potential_Pauli_artificial(r, chargeRx, chargeRy, chargeRz )
    r = r;
    D = 1;
111 dist = 3.5;
    aa = 2;
    # 4.5 coefficient to convert to meV
    dd = D*exp(aa*dist) * 4.5;
    U = dd.*exp(-aa.*r) ;
116 Ex = -aa .* U .* chargeRx ./r;
    Ey = -aa .* U .* chargeRy ./r;
    Ez = -aa .* U .* chargeRz ./r;
    endfunction

121 # calculate chemical potential and gradient for every
    # point of the grid for PTCDA layer
    function [U, Ex, Ey, Ez ] = \
      potential_chem_artificial(r, chargeRx, chargeRy, chargeRz )
    r = r;
126 D = 1;
    dist = 3.5;
    aa = 1;
```

```
      # 4.5 coefficient to convert to meV
      dd = -2*D*exp(aa*dist) * 4.5;
131   U = dd.*exp(-aa.*r) ;
      Ex = -aa .* U .* chargeRx ./r;
      Ey = -aa .* U .* chargeRy ./r;
      Ez = -aa .* U .* chargeRz ./r;
      endfunction
136
      # calculate Pauli repulsion potential and gradient for every point
      # of the grid for the tip
      function [U, Ex, Ey, Ez] = \
       potential_Pauli_artificial_tip(r, chargeRx, chargeRy, chargeRz )
141   r = r;
      D = 25;
      dist = 1.9;
      aa = 2;
      # 4.5 coefficient to convert to meV
146   dd = D*exp(aa*dist)* 4.5;
      U = dd.*exp(-aa.*r) ;
      Ex = -aa .* U .* chargeRx ./r;
      Ey = -aa .* U .* chargeRy ./r;
      Ez = -aa .* U .* chargeRz ./r;
151 endfunction

      # calculate chemical potential and gradient for every point
      # of the grid for the tip
      function [U, Ex, Ey, Ez ] = \
156   potential_chem_artificial_tip(r, chargeRx, chargeRy, chargeRz )
      r = r;
      D = 25;
      dist = 1.9;
      aa = 1;
161 # 4.5 coefficient to convert to meV
      dd = -2*D*exp(aa*dist)* 4.5;
      U = dd.*exp(-aa.*r) ;
      Ex = -aa .* U .* chargeRx ./r;
      Ey = -aa .* U .* chargeRy ./r;
166 Ez = -aa .* U .* chargeRz ./r;
      endfunction

      # calculate 1/z values for every point of volume of interest
      function [chargeRx, chargeRy, chargeRz ] = \
171       uniform_relation(areaz,qCoord)
      chargeRx = - qCoord(1);
      chargeRy = - qCoord(2);
      chargeRz = areaz - qCoord(3);
      endfunction
176
      # calculate 1/r, where r = (x,y,z)
```

```
     function [chargeRx, chargeRy, chargeRz ] = \
          spherical_relation(areax, areay, areaz, qCoord)
      chargeRx = areax - qCoord(1);
181   chargeRy = areay - qCoord(2);
      chargeRz = areaz - qCoord(3);
     endfunction

     # calculate angular coefficient for the tip field calculation
186 function [out] = getAngleCoeff(areax, areay, areaz, qCoord)
      chargeRx = areax - qCoord(1);
      chargeRy = areay - qCoord(2);
      chargeRz = areaz - qCoord(3);
      rs = component2abs(chargeRx, chargeRy, 0);
191   r = component2abs(chargeRx, chargeRy, chargeRz);
      # kd - coefficient of variation, shows how stable is the position under the tip
      kd = 0.5;
      out = (1-kd*(rs./r).^2);
     endfunction
196
     # calculate potentials and fields created by PTCDA layer
     function [U, Ex, Ey, Ez ] = \
      potentials2(areax,areay,areaz, chargesPosition, qQValue)
     # prepare initial grid
201   U_pauli = zeros([size(areax)]);
      U_chem = zeros([size(areax)]);
      U_vdw = zeros([size(areax)]);
      U_el = zeros([size(areax)]);
      Ex = zeros([size(areax)]);
206   Ey = zeros([size(areax)]);
      Ez = zeros([size(areax)]);
     # fill grid with values
      for ii = 1:(size(qQValue)(2))
       [chargeRx, chargeRy, chargeRz ] = \
211   spherical_relation(areax, areay, areaz, chargesPosition(ii,:));
       r = component2abs(chargeRx, chargeRy, chargeRz);

       [U1, Ex1, Ey1, Ez1] = \
       potential_Pauli_artificial(r, chargeRx, chargeRy, chargeRz) ;
216    [U2, Ex2, Ey2, Ez2] = \
       potential_chem_artificial( r, chargeRx, chargeRy, chargeRz) ;
       [U3, Ex3, Ey3, Ez3] = \
       potential_vdW( r, chargeRx, chargeRy, chargeRz) ;

221    U_pauli = U_pauli + U1 ;
       U_chem = U_chem + U2 ;
       U_vdw = U_vdw + U3; # is not used

       Ex = Ex + Ex1 + Ex2 + Ex3; # is not used
226    Ey = Ey + Ey1 + Ey2 + Ey3;
```

```
     Ez = Ez + Ez1 + Ez2 + Ez3;
    end
  # return values
   U.pauli = U_pauli;
231 U.chem = U_chem;
   U.vdw = U_vdw ;
   endfunction

  # calculate potentials and fields created by the tip
236 function [U, Ex, Ey, Ez ] = \
     potentialsTip(areax,areay,areaz,chargesPosition,qQValue)
   # prepare initial grid
   U_pauli = zeros([size(areax)]);
   U_chem = zeros([size(areax)]);
241 U_vdw = zeros([size(areax)]);
   U_el = zeros([size(areax)]);
   Ex = zeros([size(areax)]);
   Ey = zeros([size(areax)]);
   Ez = zeros([size(areax)]);
246 qQValue = zeros([size(areax)]);
   # calculate potential for every point of the grid
   for ii = 1:(size(qQValue)(2))

    angleCoeff = \
251 getAngleCoeff(areax, areay, areaz, chargesPosition(ii,:));

    [chargeRx, chargeRy, chargeRz ] = \
    spherical_relation(areax, areay, areaz, chargesPosition(ii,:));
    r = component2abs(chargeRx, chargeRy, chargeRz);
256
    [U1, Ex1, Ey1, Ez1] = potential_Pauli_artificial_tip(r,0,0,0) ;
    [U2, Ex2, Ey2, Ez2] = potential_chem_artificial_tip(r,0,0,0) ;
    U_pauli = U_pauli + U1 ;
    U_chem = U_chem + U2 ;
261
   end
  # return values
   U.pauli = U_pauli;
   U.chem = U_chem;
266 U.vdw = U_vdw ;
   U.angCoef = angleCoeff;

   endfunction

271 # convert components to distance and to projection
   function val = component2abs(x, y, z)
   if (z!=0),
    val = sqrt(x.*x + y.*y + z.*z);
   else,
```

```
276  val = sqrt(x.*x + y.*y);
      end;
     endfunction

     # calculate index from coordinate
281  function [m,n] = coord2index(x,y, areax, areay)
      [xs,ys, zs] = size(areax);
      m = floor((xs-1)/(areax(1,end,1)-areax(1,1,1))*(x-areax(1,1,1))+1);
      n = floor((ys-1)/(areay(end,1,1)-areay(1,1,1))*(y-areay(1,1,1))+1);
     endfunction
286
     # calculate step between grid points in x,y,z directions
     function [stepx, stepy, stepz] = getSteps(areax, areay, areaz)
      stepx = areax(2,2,2) - areax(2,1,2);
      stepy = areay(2,2,2) - areay(1,2,2);
291  stepz = areaz(2,2,2) - areaz(2,2,1);
     endfunction

     # find energy needed to shift D2 for particular distance
     # and coordinate of the point
296  function [Point]=getFringeEnergy2D(x,y,zmap,myXTipPos,\
             myYTipPos,radius)
     # debug flag
      debugflag = 0;
     # iteration step in energy
301  energy_step = 0.1;
     # initial parameters for
      Point.En = NA;
      Point.x = myXTipPos;
      Point.y = myYTipPos;
306  # get index from point coordination
      x_index = floor((myXTipPos-x(1))/(x(end)-x(1))*(length(x)-1)+1);
      y_index = floor((myYTipPos-y(1))/(y(end)-y(1))*(length(y)-1)+1);

      xmin_index = max ( floor( ( (myXTipPos - radius) - x(1)) \
311   / (x(end)-x(1)) * (length(x)-1) +1),1);
      xmax_index = min ( floor( ( (myXTipPos + radius) - x(1)) \
       / (x(end)-x(1)) * (length(x)-1) +1),length(x));

      ymin_index = max ( floor( ( (myYTipPos - radius) - y(1)) \
316   / (y(end)-y(1)) * (length(y)-1) +1),1);
      ymax_index = min ( floor( ( (myYTipPos + radius) - y(1)) \
       / (y(end)-y(1)) * (length(y)-1) +1),length(y));

      z_cur = zmap(ymin_index:ymax_index, xmin_index:xmax_index);
321  Energy_min_near_tip = min(min(z_cur));

      [y_energy_min_index, x_energy_min_index] = ind2sub([length(y), \
         length(x)], find( zmap == Energy_min_near_tip));
```

```
     # esli eto real min it will not move
326  x_area_cur_min = max(x_energy_min_index-3,1);
      x_area_cur_max = min(x_energy_min_index+3, length(x));
      y_area_cur_min = max(y_energy_min_index-3, 1);
      y_area_cur_max = min(y_energy_min_index+3, length(y));

331  z_cur = zmap(y_area_cur_min:y_area_cur_max, \
          x_area_cur_min:x_area_cur_max);
      # find potential minimum value near for tip position
      Energy_min_near_tip_pr = min(min(z_cur));

336  [y_energy_min_index_pr, x_energy_min_index_pr] = \
          ind2sub([length(y), length(x)], \
          find( zmap == Energy_min_near_tip_pr));
      # find potential value for tip position
      Energy_under_tip = zmap(y_index, x_index);
341  area_flag = 0*ones(length(y), length(x));

      [yy0, xx0] = ind2sub([length(y), length(x)], \
          find(zmap < Energy_min_near_tip_pr));
      # length(xx0)
346  for ii = 1:length(yy0)
       area_flag( yy0(ii), xx0(ii) ) = -1;
      end

     # Main routine for findings points that are located at certain distance
351 # with minimal work needed to move it there. start from E_min and then
     # increasing energy check what points we can reach. Stop if the points is
     # at the distance of interest otherwise continue searching.
      if ( ((x(x_energy_min_index_pr) - x(x_index))^2 + \
        (y(y_energy_min_index_pr) - y(y_index))^2) < radius^2)

356
       area_flag(y_energy_min_index_pr, x_energy_min_index_pr) = 1;
       flag = 1;
       iiE = 0;

361   while(flag)
        flag = 0;
        iiE = iiE+1;
        energy_next_1 = Energy_min_near_tip_pr+energy_step*(iiE-1);
        energy_next_2 = Energy_min_near_tip_pr+energy_step*iiE;
366    if (energy_next_2<0)
         flag = 1;
        end

        out = zmap;
371     out( out > energy_next_2 ) = NA;
        out( out <= energy_next_1 ) = NA;
        [yy, xx] = ind2sub([length(y),length(x)], find(!isna(out)));
```

```
     xx = [xx; xx0];
     yy = [yy; yy0];
376  flag2 = 1;
  # add points with new, a bit higher, energy to the sequence
     while(flag2)
      flag2 = 0 ;
  # for each point add neighbour points to sequence
381   for ii = 1:length(xx)
       area = [];
       for ix = -1:1,
        for iy = -1:1,
  # check if point is not out of range of calculated area
386       if( xx(ii)+ix!=0 &&\
           yy(ii)+iy!=0 &&\
           xx(ii)+ix!= length(x) + 1 &&\
           yy(ii)+iy!= length(y) + 1 \
           )
391        area = [area, area_flag(yy(ii)+iy, xx(ii)+ix)];
         end
        end
       end
  # for each point in sequence calculate if it is fulfil selection rule
396    if (max(area) == 1)
        area_flag( yy(ii), xx(ii) ) = 1;
        dx = x(xx(ii)) - x(x_index);
        dy = y(yy(ii)) - y(y_index);
        point_tip_dist = sqrt(dx*dx + dy*dy);
401 # stop if point is less than critical distance of radius
        if (point_tip_dist <radius)
         if ii == 1
          refr = 2:length(xx);
         elseif ii == length(xx)
406        refr = 1:length(xx)-1;
         else
          refr = [1:(ii-1),(ii+1):length(xx)];
         end
         xx = xx(refr);
411      yy = yy(refr);
         flag2 = 1;
         break
        end
        flag = 0;
416     energy2excite = zmap(yy(ii), xx(ii) )
        Point.En = energy2excite;
        Point.x = x(xx(ii));
        Point.y = y(yy(ii));
        break
421    end
      end
```

```
        end

  # fill rest of yy loop with 0
426    for ii = 1:length(xx)
        area_flag( yy(ii), xx(ii) ) = -1;
      end
      xx0 = xx;
      yy0 = yy;
431
      if (debugflag ==1)
       figure
       surf(area_flag)
       xlabel('x');
436    end

     end
    else
     energy2excite = 0;
441 end

  endfunction

  ####################################################################
446 # Function main()
  ####################################################################

  function main(Param)
  # preparation procedures
451
  # set current position of the tip
   tipHightPosition = Param.h;
   tipx = Param.x;
   tipy = Param.y;
456
  # prepare global values that should be calculated once
   ifsave = 0; # flag if we need to save value
   cutoff = 0.1; # cutoff in z distance to reduce calculating area
   global U; # energy potential value
461 global Ex; # energy potential gradient value
   global Ey;
   global Ez;
   global chargesPosition; # position of atoms of PCTDA
   global qQValue; # charge values of atoms of PTCDA
466
  # allocate volume of interest and create grid for it
   [areax, areay, areaz] = prepare_space(tipHightPosition-cutoff);
   [stepx, stepy, stepz] = getSteps(areax, areay, areaz);
   [xN, yN, zN] = size(areax);
471 zmin = areaz(1);
```

```
 zmax = areaz(end);

# reload unchanged parameters instead of calculate them again
 if(size(U)(2)==0)
# create PTCDA layer and buld potential distribution for it
  [chargesPosition, qQValue] = create_PTCDA_hb_layer(2);
  [U, Ex, Ey, Ez] = \
  potentials2(areax, areay, areaz, chargesPosition, qQValue);
  end


# preview the molecule
 if(1)
  figure;
  plot(chargesPosition(:,1), chargesPosition(:,2),'o')
  hold on;
  title("PTCDA sketch");
  axis equal;
 end


# calculate potential for tip

# create tip
 [chargesPosition1, qQValue1] = \
  create_tip(tipx, tipy, tipHightPosition);
# calculate potential energy created by tip
 [U1, Ex1, Ey1, Ez1] = \
  potentialsTip(areax, areay, \
  areaz, chargesPosition1, qQValue1);


# calculate total potential energy
 amplCoef = 1;
 amplCoefSurf = 1;
 UoiSurf = (U.pauli + U.chem) * amplCoefSurf;
 UoiTip = ( U1.pauli + U1.chem).*U1.angCoef*amplCoef;
 Uoi = UoiTip + UoiSurf;


# preview slices across molecule at certain x or y position
 if(1)
# slice positions
 xslice = [0]; #[tipx];
 yslice = [0]; #[tipy];
 zslice = []; # no slice at z
# plot picture
 figure;
 h = slice(areax, areay, areaz, Uoi, xslice, yslice, zslice);
 colorbar;
 set(h, 'EdgeColor', 'none')
 title('Energy field')
 if(1) # preview molecule position
```

```
521   hold on;
      figure;
      plot3(chargesPosition1(:,1), chargesPosition1(:,2),'o')
      title("PTCDA slice");
     end
526  end

   # preview approach curves at certain x,y position of interest
   # this part is needed to monitor Morse potential for different point.
    if (1)
531  figure;
     hold on;
   # point 1 # C6 ring center coordinate
     poixV = 9.7;
     poiyV = 6.1;
536  [m,n] = coord2index(poixV, poiyV, areax, areay);
     poiz = [1:zN];
     z_coord = areaz(1,1,poiz)(:);
     u_value1 = (Uoi)(n, m, poiz)(:);
     u_value1(u_value1 >1) =NA; # cut value for better view
541  plot(z_coord, u_value1, 'bo-');
   # point 2 # C atom coordinate
     poixV = 10.6;
     poiyV = 5;
     [m,n] = coord2index(poixV, poiyV, areax, areay);
546  poiz = [1:zN];
     z_coord = areaz(1,1,poiz)(:);
     u_value1 = (Uoi)(n, m, poiz)(:);
     u_value1(u_value1 >1) = NA;
     plot(z_coord, u_value1, 'ro-');
551 # surface below the tip
     u_valueSurf = (UoiSurf)(tipyindex, tipxindex, poiz)(:);
     u_valueSurf(u_valueSurf >1) =NA;
     plot(z_coord, u_valueSurf, 'k.-');
   # tip + surface below tip
556  u_value1 = (Uoi)(tipyindex, tipxindex, poiz)(:);
     u_value1(u_value1 >1) =NA;
     plot(z_coord, u_value1, 'go-');
   # additional info for
     xlabel("z, angstrem");
561  ylabel("U, meV");
     title("void(blue), atom(red), tip-surf(green)");
     if (ifsave ==1)
      print('-dsvg', '-r300', '-color', \
       ['Morse_under_tip','TH_',num2str(tipHightPosition*10),\
566   '_xTip_', num2str(tipx*10+100),\
      '_yTip_', num2str(tipy*10+100)]);
      close;
     end
```

```
       end
571
    # preview slice at certain hight (distOfInt)
     if (0)
     # for distOfInt = [0.5:0.5:3];#(tipHightPosition-cutoff)],
     # for distOfInt = [0.5:0.2:4],
576  Energy = min(min(min(Uoi)));
     disp(["Energy: ", num2str(Energy)])
     [y, x, z] = ind2sub([xN, yN, zN], find( Uoi == Energy));
     figure;
     distOfInt = 1.6;
581  poiz = floor((zN-1)/(zmax-zmin)*(distOfInt - zmin) + 1);
     out = reshape(Uoi(:,:,poiz),xN,yN);
     pcolor(areax(1,:,1)(:), areay(:,1,1)(:) , out);
     xlabel("x, angstrem");
     ylabel("y, angstrem");
586  colorbar;
     title( ['slice_TH_',\
       num2str(tipHightPosition*1),\
       '_xTip_', \
       num2str(tipx*1),\
591    '_yTip_', \
       num2str(tipy*1),\
       '_zEnergy_',\
       num2str(distOfInt*1),\
       '_Energy_', \
596    num2str(Energy)])
     shading flat;
    # save result
     if (ifsave == 1)
      print('-dsvg', '-r300', '-color', \
601    ['bw_map_TH_',\
       num2str(tipHightPosition*10),\
       '_xTip_', \
       num2str(tipx*10+100),\
       '_yTip_', \
606    num2str(tipy*10+100),\
       '_zEnergy_',\
       num2str(distOfInt*10),\
       '_Energy_', \
       num2str(Energy),\
611    '.svg']);
      close;
     end
    # preview results
     if(1)
616    [PX,PY] = gradient( out, stepx, stepy) ;
       figure;
       quiver(areax(1,:,1)(:),areay(:,1,1)(:),PX(:,:,1),PY(:,:,1));
```

```
      axis equal;
      hold on;
621   title('3D vectors model')
      xlabel("x, angstrem");
      ylabel("y, angstrem");
     end
   # preview molecule or point of interest
626  if(1)
      hold on;
      plot(chargesPosition(:,1), chargesPosition(:,2),'g.')
      end

631  px = polyfit(areax(1,(x-2):(x+2),1)(:), \
         Uoi(y,(x-2):(x+2),z)(:),2);
     py = polyfit(areay((y-2):(y+2),1,1)(:), \
         Uoi((y-2):(y+2),x,z)(:),2);
     end
636
   # preview vector map of lateral shift of D2
    if(1)
     [PX,PY,PZ] = gradient(Uoi,stepx,stepy,stepz) ;
     for distOfInt = [0.5:0.5:1.5];
641   poiz = floor((zN-1)/(zmax-zmin)*(distOfInt - zmin) + 1);
      out = reshape(Uoi(:,:,poiz),xN,yN);
      figure;
      quiver(areax(1,:,1)(:), areay(:,1,1)(:), \
          PX(:,:,poiz), PY(:,:,poiz));
646   axis equal;
      hold on;
      title( ['3D vectors map: XY vec, Energy_', \
        num2str(distOfInt*10) ]);
      xlabel("x, angstrem");
651   ylabel("y, angstrem");
    # take map values at distance of poiz
      PXmat = PX(:,:,poiz);
      PX = PX(:,:,poiz);
      dyPX = sign(PX(:,1:end-1,1))-sign(PX(:,2:end,1));
656   dyPX = abs([dyPX, dyPX(:,end,1)]);
      PX = PX';
      dxPX = sign(PX(:,1:end-1,1))-sign(PX(:,2:end,1));
      dxPX = abs([dxPX, dxPX(:,end,1)]);
      PX = PX';
661
      figure;
      surf(areax(1,:,1)(:), areay(:,1,1)(:), sqrt(dxPX.^2+dyPX.^2) );
      shading flat;
      axis equal;
666   colorbar;
      title(['dPX, Energy_', num2str(distOfInt*10) ] );
```

```
       xlabel("x, angstrem");
       ylabel("y, angstrem");

671    figure;
       surf(areax(1,:,1)(:), areay(:,1,1)(:), PZ(:,:,poiz));
       shading flat;
       axis equal;
       colorbar;
676    title(['3D vector model: Z vector value, Energy_', \
           num2str(distOfInt*10)]);
       xlabel("x, angstrem");
       ylabel("y, angstrem");
     end
681  end


   # find work needed to move D2 away from the tip
    if (1)
    # for distOfInt = [1.5:0.3:(tipHightPosition-cutoff)],
686  # for distOfInt = [1.5:0.3:3.5],
     Energy = min(min(min(Uoi)));
     [y, x, z] = ind2sub([xN, yN, zN], find( Uoi == Energy));
     distOfInt = areaz(1,1,z)(:) ;
     [tipxindex, tipyindex] = coord2index(tipx, tipy, areax, areay);
691  poiz = floor((zN-1)/(zmax-zmin)*(distOfInt - zmin) + 1);
   # x, y, z, xxTip (x tip position), yyTip (y tip position), radius
     [out] = getFringeEnergy2D(areax(1,:,1), areay(:,1,1), \
            Uoi(:,:,z), tipx, tipy, 2);
     E_fringe = out.En
696  [xInd, yInd] = coord2index(out.x, out.y, areax, areay)
   # find parameters for harmonic potential
     px = polyfit(areax(1,(x-2):(x+2),1)(:), \
         Uoi(y,(x-2):(x+2),z)(:),2);
     pp = polyval(px,areax(1,(x-2):(x+2),1)(:));
701  py = polyfit(areay((y-2):(y+2),1,1)(:), \
         Uoi((y-2):(y+2),x,z)(:),2);
     pp = polyval(py, areay((y-2):(y+2),1,1)(:) );
   # save the results
     if (ifsave == 1)
706  print('-dsvg', '-r300', '-color', \
       ['line_x_minEnergy_TH_', num2str(tipHightPosition*10), \
       '_x_', num2str(tipx*10+100),'_y_',num2str(tipy*10+100),\
       '_z_', num2str(distOfInt*10), '.svg']);
     close;
711  end
   # write to file
     if (1)
     disp('writing')
     nameX = 'all_i_want_to do_';
716  fid = fopen( ['out_TSdist_', num2str(tipHightPosition*10),\
```

```
          nameX, '.txt' ] ,'a+');
       fprintf(fid,\
        '#f\t#f\t#f\t#f\t#f\t#f\t#f\t#f\t#f\t#f\t#f\n', \
        tipx, tipy, tipHightPosition,\
721     areax(1,x,1), areay(y,1,1), areaz(1,1,z),\
        areax(1,xInd,1), areay(yInd,1,1), \
        Energy, E_fringe, \
        px(1), py(1)
        );
726     fclose(fid);
      end
    end


    # show 3D picture
731  if (1)
      tolerance = 0.2;
      Energy = min(min(min(Uoi)))+0*tolerance
      out = Uoi;
      out( out > (Energy+tolerance) ) = NA;
736   out( out < (Energy-tolerance) ) = NA;
      [y, x, z] = ind2sub([xN, yN, zN], find(!isna(out)));
      x1 = areax(1,x,1)(:);
      y1 = areay(y,1,1)(:);
      z1 = areaz(1,1,z)(:);
741   figure;
      plot3(x1,y1,z1,'.');
      xlabel("x, angstrem");
      ylabel("y, angstrem");
      zlabel("z, angstrem");
746   # zlabel("meV")
      # colorbar;
      title(["points with the energy of ",num2str(Energy),', TH_',\
         num2str(tipHightPosition*10),', xTip_', \
         num2str(tipx*10),', yTip_', num2str(tipy*10)])
751   Energy = min(min(min(Uoi)))+2*tolerance
      out = Uoi;
      out( out > (Energy+tolerance) ) = NA;
      out( out < (Energy-tolerance) ) = NA;
      [y, x, z] = ind2sub([xN, yN, zN], find(!isna(out)));
756   x2 = areax(1,x,1)(:);
      y2 = areay(y,1,1)(:);
      z2 = areaz(1,1,z)(:);
      hold on;
      plot3(x2,y2,z2,'.r');
761   Energy = min(min(min(Uoi)))+4*tolerance
      out = Uoi;
      out( out > (Energy+tolerance) ) = NA;
      out( out < (Energy-tolerance) ) = NA;
```

```
766  [y, x, z] = ind2sub([xN, yN, zN], find(!isna(out)));
     x3 = areax(1,x,1)(:);
     y3 = areay(y,1,1)(:);
     z3 = areaz(1,1,z)(:);
     hold on;
771  plot3(x3,y3,z3,'.y');
     set(gcf,'Color',[0.6,0.6,0.6])
     # set(gca,'CameraPosition',20*[sin(angle) 0 cos(angle) ]);
   # preview molecule or point of interest
     if(1)
776  hold on;
     #figure;
     ii = 4;
     atom_in_PTCDA = 38; # 30 for core ; 38 for whole
     plot3(chargesPosition(\
781      (atom_in_PTCDA*ii+1):(atom_in_PTCDA*(ii+1)),1), \
         chargesPosition(\
         (atom_in_PTCDA*ii+1):(atom_in_PTCDA*(ii+1)),2),'ok')


     hold on;
786  ii = 0;
     plot3(chargesPosition(\
         (atom_in_PTCDA*ii+1):(atom_in_PTCDA*(ii+1)),1),\
         chargesPosition(\
         (atom_in_PTCDA*ii+1):(atom_in_PTCDA*(ii+1)),2),'ok')
791
     Energy = min(min(min(Uoi)));
     [y, x, z] = ind2sub([xN, yN, zN], find( Uoi == Energy));
     distOfInt = areaz(1,1,z)(:);
     poiz = z;
796  out = reshape(Uoi(:,:,poiz),xN,yN);
     pcolor(areax(1,:,1)(:), areay(:,1,1)(:) , out);
     shading flat;
     end
     view(240, 30);
801  if(ifsave == 5)
      print('-dsvg', '-r300', '-color', \
         ['3D_',\
          'TH_',\
          num2str(tipHightPosition*10),\
806       '_xTip_', \
          num2str(tipx*10+100),\
          '_yTip_', \
          num2str(tipy*10+100)]);
      close;
811  end
     name = ['TH_',num2str(tipHightPosition*10),'_3D'];
   # prepare data to save
     toSave.x1 = x1;
```

```
      toSave.z1 = z1;
816   toSave.y1 = y1;
      toSave.x2 = x2;
      toSave.z2 = z2;
      toSave.y2 = y2;
      toSave.x3 = x3;
821   toSave.z3 = z3;
      toSave.y3 = y3;
      toSave.chargesPosition = chargesPosition;
      toSave.areax = areax;
      toSave.areay = areay;
826   toSave.out = out;
      save name toSave;
      close;
     end
    endfunction
831
    ####################################################################
    # program starts here
    ####################################################################

836 # x and y steps of grid for tip position
    mystep = (20/127);
    # h - z-position of the tip;
    # x,y - x and y position of the tip
    [h ,y, x] = meshgrid( [4], -5:mystep:12, -11:mystep:6 );
841
    allval = length(x(:));
    for ii = 1:length(x(:))
     Param(ii).x = x(ii);
     Param(ii).y = y(ii);
846  Param(ii).h = h(ii);
    end

    # global parameters needed to calculate once to save total
    # computational time
851 global U;
    global Ex;
    global Ey;
    global Ez;
    global chargesPosition;
856 global qQValue;

    for tt = 1:allval
     clear -x tt Param allval U Ex Ey Ez chargesPosition qQValue;
     main(Param(tt));
861 end
```

The description of the unit cell of PTCDA on Au(111).

```
% Description of the herring bone structure of PTCDA layer
% structure of the string is the next:
% name #num - atom_descroption atom_position - partial_charge_value x y z
4 %
% mol 1
atom 1 - C 0.004196167 0.1528866 -3.744266 0.01138122
atom 2 - C -0.1479287 -1.209324 -3.550244 0.005194386
atom 3 - C -0.108273 1.021363 -2.635129 0.01064787
9 atom 4 - C 0.01191139 0.5325196 -1.34359 0.004555251
atom 5 - C -0.03022575 -0.8769351 -1.12241 0.00149474
atom 6 - C 0.0245142 -1.744455 -2.232792 0.0008782791
atom 7 - C -0.1479268 -3.152233 -2.032282 -0.003795298
atom 8 - C 0.01191235 -1.432525 0.1916723 -0.0007755269
14 atom 9 - C -0.1082726 -2.80397 0.3535403 -0.004852661
atom 10 - C 0.004196405 -3.67005 -0.7574658 -0.006796176
atom 11 - C -0.1479297 3.152227 2.032275 -0.004544073
atom 12 - C 0.02451372 1.744451 2.232796 9.880461e-006
atom 13 - C 0.004193544 3.670039 0.7574549 -0.006938186
19 atom 14 - C -0.1082716 2.803954 -0.3535442 -0.003388885
atom 15 - C 0.01190948 1.432511 -0.1916624 0.0007271195
atom 16 - C -0.0302248 0.8769233 1.122421 0.0008460354
atom 17 - C 0.01191139 -0.5325347 1.343607 0.001470514
atom 18 - C -0.1479259 1.209327 3.550254 0.003406957 3
24 atom 19 - C 0.004196167 -0.1528943 3.74429 0.005388714
atom 20 - C -0.1082721 -1.021377 2.63516 0.003597346
atom 21 - H 0.1296895 0.5699118 -4.759921 0.01639607
atom 22 - H 0.1222507 2.111245 -2.799161 0.01430543
atom 23 - H 0.1222504 3.226784 -1.371374 -0.003759135
29 atom 24 - H 0.129689 4.756413 0.5985163 -0.01149259
atom 25 - H 0.1222502 -2.111263 2.799208 0.003753818
atom 26 - H 0.1296894 -0.569921 4.759953 0.008180749
atom 27 - H 0.1222503 -3.226808 1.371366 -0.006442073
atom 28 - H 0.1296895 -4.75643 -0.5985366 -0.01053608
34 atom 29 - C 0.4089208 4.031771 3.22193 -0.00711445
atom 30 - C 0.4089148 2.150876 4.691456 0.005151376
atom 31 - O -0.3057137 5.240309 3.273805 -0.01400339
atom 32 - O -0.3057232 1.90885 5.87667 0.01171442
atom 33 - O -0.2243776 3.512439 4.495692 -0.001118116
39 atom 34 - C 0.4089155 -2.150849 -4.691467 0.002481526
atom 35 - C 0.4089139 -4.031764 -3.221941 -0.005188323
atom 36 - O -0.3057203 -1.908796 -5.876687 0.003530481
atom 37 - O -0.3057222 -5.240334 -3.273822 -0.008757038
atom 38 - O -0.2243714 -3.512417 -4.495708 -0.002410372
44 % endmol 1
% mol 2
atom 1 - C 0.004196167 13.27003 5.392527 0.01138122
atom 2 - C -0.1479287 12.75223 4.117719 0.005194387
atom 3 - C -0.108273 12.40394 6.503535 0.01064787
```

```
49 atom 4 - C 0.01191139 11.03251 6.341655 0.00455525
   atom 5 - C -0.03022575 10.47692 5.027581 0.001494739
   atom 6 - C 0.0245142 11.34445 3.917206 0.0008782792
   atom 7 - C -0.1479268 10.80932 2.59975 -0.003795298
   atom 8 - C 0.01191235 9.067465 4.8064 -0.0007755269
54 atom 9 - C -0.1082726 8.578621 3.514849 -0.004852662
   atom 10 - C 0.004196405 9.4471 2.405717 -0.006796175
   atom 11 - C -0.1479297 8.390684 9.700246 -0.004544074
   atom 12 - C 0.02451372 7.855551 8.382794 9.880516e-006
   atom 13 - C 0.004193544 9.752909 9.89427 -0.006938186
59 atom 14 - C -0.1082716 10.62138 8.785129 -0.003388885
   atom 15 - C 0.01190948 10.13252 7.493592 0.0007271195
   atom 16 - C -0.0302248 8.723068 7.272421 0.0008460354
   atom 17 - C 0.01191139 8.167473 5.958335 0.001470514
   atom 18 - C -0.1479259 6.447769 8.18229 0.003406957
64 atom 19 - C 0.004196167 5.929943 6.907474 0.005388714
   atom 20 - C -0.1082721 6.796023 5.79646 0.003597346
   atom 21 - H 0.1296895 14.3564 5.55145 0.01639607
   atom 22 - H 0.1222507 12.82677 7.52136 0.01430543
   atom 23 - H 0.1222504 11.71127 8.949176 -0.003759135
69 atom 24 - H 0.129689 10.16994 10.90992 -0.01149259
   atom 25 - H 0.1222502 6.373182 4.778641 0.003753817
   atom 26 - H 0.1296894 4.843561 6.748544 0.008180749
   atom 27 - H 0.1222503 7.488733 3.350804 -0.006442073
   atom 28 - H 0.1296895 9.030073 1.390055 -0.01053608
74 atom 29 - C 0.4089208 7.449148 10.84146 -0.007114451
   atom 30 - C 0.4089148 5.568247 9.371955 0.005151376
   atom 31 - O -0.3057137 7.691187 12.02665 -0.01400339
   atom 32 - O -0.3057232 4.359686 9.423846 0.01171442
   atom 33 - O -0.2243776 6.087586 10.64571 -0.001118116
79 atom 34 - C 0.4089155 13.63177 2.928071 0.002481526
   atom 35 - C 0.4089139 11.75086 1.458541 -0.005188322
   atom 36 - O -0.3057203 14.84034 2.8762 0.003530481
   atom 37 - O -0.3057222 11.50882 0.2733212 -0.008757038
   atom 38 - O -0.2243714 13.11244 1.654311 -0.002410372
84 % endmol 2
   % Translation vector description
   0 1.90885 5.87667
   1 21.10885 5.87667
   2 1.908851 18.17667
```

Bibliography

[1] C. W. Tang and S. A. Van Slyke. Organic electroluminescent diodes. *Applied Physics Letters*, 51:913, 1987.

[2] J. Blochwitz, T. Fritz, M. Pfeiffer, K. Leo, D. M. Alloway, P. A. Lee, and N. R. Armstrong. Interface electronic structure of organic semiconductors with controlled doping levels. *Organic Electronics*, 2(2):97–104, 2001.

[3] K. Walzer, B. Maennig, M. Pfeiffer, K. Leo, et al. Highly efficient organic devices based on electrically doped transport layers. *Chemical Reviews-Columbus*, 107(4):1233–1271, 2007.

[4] Norbert Koch. Organic electronic devices and their functional interfaces. *ChemPhysChem*, 8(10):1438–1455, 2007.

[5] Klaus Müllen and Ullrich Scherf. *Organic light emitting devices*. Wiley Online Library, 2006.

[6] J. H. Burroughes, D. D. C. Bradley, A. R. Brown, R. N. Marks, K. Mackay, R. H. Friend, P. L. Burns, and A. B. Holmes. Light-emitting diodes based on conjugated polymers. *nature*, 347(6293):539–541, 1990.

[7] Henning Sirringhaus, Nir Tessler, and Richard H. Friend. Integrated optoelectronic devices based on conjugated polymers. *Science*, 280(5370):1741–1744, 1998.

[8] R. H. Friend, R. W. Gymer, A. B. Holmes, J. H. Burroughes, R. N. Marks, C. D. D. C. Taliani, D. D. C. Bradley, D. A. Dos Santos, J. L. Bredas, M. Lögdlund, et al. Electroluminescence in conjugated polymers. *Nature*, 397(6715):121–128, 1999.

[9] Peter Peumans, Soichi Uchida, and Stephen R Forrest. Efficient bulk heterojunction photovoltaic cells using small-molecular-weight organic thin films. *Nature*, 425(6954):158–162, 2003.

[10] Barry P. Rand, Jan Genoe, Paul Heremans, and Jef Poortmans. Solar cells utilizing small molecular weight organic semiconductors. *Progress in Photovoltaics: Research and Applications*, 15(8):659–676, 2007.

[11] B. Maennig, J. Drechsel, D. Gebeyehu, P. Simon, F. Kozlowski, A. Werner, Fenghong Li, S. Grundmann, S. Sonntag, M. Koch, et al. Organic pin solar cells. *Applied Physics A*, 79(1):1–14, 2004.

[12] P. Peumans, V. Bulovic, and S.R. Forrest. Efficient photon harvesting at high optical intensities in ultrathin organic double-heterostructure photovoltaic diodes. *Applied Physics Letters*, 76(19):2650–2652, 2000.

[13] Ruth Shinar and Joseph Shinar. *Organic electronics in sensors and biotechnology.* McGraw-Hill, Inc., 2009.

[14] Giuseppe Arrabito and Bruno Pignataro. Solution processed micro- and nano-bioarrays for multiplexed biosensing. *Analytical chemistry*, 84(13):5450–5462, 2012.

[15] Ching W. Tang. Two-layer organic photovoltaic cell. *Applied Physics Letters*, 48:183, 1986.

[16] Peter Strohriegl and Juozas V. Grazulevicius. Charge-transporting molecular glasses. *Advanced Materials*, 14(20):1439–1452, 2002.

[17] Gilles Horowitz. Organic thin film transistors: From theory to real devices. *J. Mater. Res*, 19(7):1946–1962, 2004.

[18] W. Clemens, W. Fix, J. Ficker, A. Knobloch, and A. Ullmann. From polymer transistors toward printed electronics. *Journal of Materials Research*, 19(7):1963–1973, 2004.

[19] Susanne Scheinert and Gernot Paasch. Fabrication and analysis of polymer field-effect transistors. *physica status solidi (a)*, 201(6):1263–1301, 2004.

[20] Fabio Cicoira and Clara Santato. Organic light emitting field effect transistors: advances and perspectives. *Advanced Functional Materials*, 17(17):3421–3434, 2007.

[21] A. Dodabalapur, L. Torsi, and H. E. Katz. Organic transistors: two-dimensional transport and improved electrical characteristics. *Science*, 268(5208):270–271, 1995.

[22] Ananth Dodabalapur, H. E. Katz, L. Torsi, and R. C. Haddon. Organic heterostructure field-effect transistors. *Science*, 269(5230):1560–1562, 1995.

[23] S. F. Nelson, Y-Y. Lin, D. J. Gundlach, and T. N. Jackson. Temperature-independent transport in high-mobility pentacene transistors. *Applied physics letters*, 72(15):1854–1856, 1998.

[24] Tommie W. Kelley, Paul F. Baude, Chris Gerlach, David E. Ender, Dawn Muyres, Michael A. Haase, Dennis E. Vogel, and Steven D. Theiss. Recent progress in organic electronics: Materials, devices, and processes. *Chemistry of Materials*, 16(23):4413–4422, 2004.

[25] Ullrich Mitschke and Peter Bäuerle. The electroluminescence of organic materials. *Journal of Materials Chemistry*, 10(7):1471–1507, 2000.

[26] Terje A. Skotheim and John R. Reynolds. *Handbook of conducting polymers*, volume 2. CRC PressI Llc, 2007.

[27] K. Oura. *Surface Science: An Introduction*. Advanced Texts in Physics. Springer, 2003.

[28] Y. Zou, L. Kilian, A. Schöll, Th. Schmidt, R. Fink, and E. Umbach. Chemical bonding of {PTCDA} on ag surfaces and the formation of interface states. *Surface Science*, 600(6):1240–1251, 2006.

[29] Takashi Kataoka, Hirohiko Fukagawa, Shunsuke Hosoumi, Kohjiro Nebashi, Kazuyuki Sakamoto, and Nobuo Ueno. Observation of a temperature-dependent transition of a copper-phthalocyanine thin film adsorbed on hopg. *Chemical Physics Letters*, 451(1):43–47, 2008.

[30] Andreas Langner, Annegret Hauschild, Sonja Fahrenholz, and Moritz Sokolowski. Structural properties of tetracene films on ag (111) investigated by spa-leed and tpd. *Surface science*, 574(2):153–165, 2005.

[31] C. Stadler, S. Hansen, F. Pollinger, C. Kumpf, E. Umbach, T.-L. Lee, and J. Zegenhagen. Structural investigation of the adsorption of snpc on ag (111) using normal-incidence x-ray standing waves. *Physical Review B*, 74(3):035404, 2006.

[32] V. Podzorov, E. Menard, A. Borissov, V. Kiryukhin, J. A. Rogers, and M. E. Gershenson. Intrinsic charge transport on the surface of organic semiconductors. *Physical review letters*, 93(8):086602, 2004.

[33] V. Podzorov, E. Menard, J. A. Rogers, and M. E. Gershenson. Hall effect in the accumulation layers on the surface of organic semiconductors. *Physical review letters*, 95(22):226601, 2005.

[34] Alessandro Troisi and Giorgio Orlandi. Charge-transport regime of crystalline organic semiconductors: Diffusion limited by thermal off-

diagonal electronic disorder. *Physical review letters*, 96(8):086601, 2006.

[35] Alessandro Troisi and Giorgio Orlandi. Dynamics of the intermolecular transfer integral in crystalline organic semiconductors. *The Journal of Physical Chemistry A*, 110(11):4065–4070, 2006.

[36] Alessandro Troisi. Prediction of the absolute charge mobility of molecular semiconductors: the case of rubrene. *Advanced Materials*, 19(15):2000–2004, 2007.

[37] H. A. v. Laarhoven, Cees F. J. Flipse, Mattijs Koeberg, Mischa Bonn, Euan Hendry, G Orlandi, OD Jurchescu, TTM Palstra, and Alessandro Troisi. On the mechanism of charge transport in pentacene. *The Journal of chemical physics*, 129:044704, 2008.

[38] J. B. Pendry. Off-diagonal disorder and 1d localisation. *Journal of Physics C: Solid State Physics*, 15(28):5773, 1982.

[39] David P. McMahon and Alessandro Troisi. Organic semiconductors: impact of disorder at different timescales. *ChemPhysChem*, 11(10):2067–2074, 2010.

[40] F.-J. Meyer Zu Heringdorf, M. C. Reuter, and R. M. Tromp. The nucleation of pentacene thin films. *Applied Physics A*, 78(6):787–791, 2004.

[41] Frank-J. Meyer Zu Heringdorf, M. C. Reuter, and R. M. Tromp. Growth dynamics of pentacene thin films. *Nature*, 412(6846):517–520, 2001.

[42] E. Bauer, M. Mundschau, W. Swiech, and W. Telieps. Surface studies by low-energy electron microscopy (leem) and conventional uv photoemission electron microscopy (peem). *Ultramicroscopy*, 31(1):49–57, 1989.

[43] E. Bauer, Y. Wei, T. Müller, A. Pavlovska, and I. S. T. Tsong. Reactive crystal growth in two dimensions: Silicon nitride on si (111). *Physical Review B*, 51(24):17891, 1995.

[44] A. Hanisch-Blicharski, A. Janzen, B. Krenzer, S. Wall, F. Klasing, A. Kalus, T Frigge, M Kammler, and M Horn-von Hoegen. Ultrafast electron diffraction at surfaces: From nanoscale heat transport to driven phase transitions. *Ultramicroscopy*, 2012.

[45] P. Babelon, A. S. Dequiedt, H. Mostefa-Sba, S. Bourgeois, P. Sibillot, and M. Sacilotti. Sem and xps studies of titanium dioxide thin films grown by mocvd. *Thin Solid Films*, 322(1):63–67, 1998.

[46] Diana Mardare, M. Tasca, M. Delibas, and G. I. Rusu. On the structural properties and optical transmittance of tio¡ sub¿ 2¡/sub¿ rf sputtered thin films. *Applied Surface Science*, 156(1):200–206, 2000.

[47] Christoph Boettcher, Boris Schade, and Juergen-Hinrich Fuhrhop. Comparative cryo-electron microscopy of noncovalent n-dodecanoyl-(d-and l-) serine assemblies in vitreous toluene and water. *Langmuir*, 17(3):873–877, 2001.

[48] Jeffrey D. Hartgerink, Elia Beniash, and Samuel I. Stupp. Self-assembly and mineralization of peptide-amphiphile nanofibers. *Science*, 294(5547):1684–1688, 2001.

[49] N. Mori, T. Oikawa, T. Katoh, J. Miyahara, and Y. Harada. Application of the "imaging plate" to tem image recording. *Ultramicroscopy*, 25(3):195–201, 1988.

[50] I. Petrov, P. B. Barna, Lars Hultman, and J. E. Greene. Microstructural evolution during film growth. *Journal of Vacuum Science & Technology A: Vacuum, Surfaces, and Films*, 21(5):S117–S128, 2003.

[51] Rolf Erni, Marta D. Rossell, Christian Kisielowski, and Ulrich Dahmen. Atomic-resolution imaging with a sub-50-pm electron probe. *Phys. Rev. Lett.*, 102:096101, Mar 2009.

[52] G. Binnig, C. F. Quate, and Ch. Gerber. Atomic force microscope. *Phys. Rev. Lett.*, 56:930–933, Mar 1986.

[53] Paul G. Piva, Gino A. DiLabio, Jason L. Pitters, Janik Zikovsky, Moh'd Rezeq, Stanislav Dogel, Werner A. Hofer, and Robert A. Wolkow. Field regulation of single-molecule conductivity by a charged surface atom. *Nature*, 435(7042):658–661, 2005.

[54] X. D. Cui, A. Primak, X. Zarate, J. Tomfohr, O. F. Sankey, A. L. Moore, T. A. Moore, D. Gust, Gari Harris, and S. M. Lindsay. Reproducible measurement of single-molecule conductivity. *Science*, 294(5542):571–574, 2001.

[55] B. D. Terris, J. E. Stern, D. Rugar, and H. J. Mamin. Contact electrification using force microscopy. *Physical Review Letters*, 63(24):2669–2672, 1989.

[56] J. E. Stern, B. D. Terris, H. J. Mamin, and D. Rugar. Deposition and imaging of localized charge on insulator surfaces using a force microscope. *Applied physics letters*, 53(26):2717–2719, 1988.

[57] Fabian Mohn, Leo Gross, Nikolaj Moll, and Gerhard Meyer. Imaging the charge distribution within a single molecule. *Nature nanotechnology*, 7(4):227–231, 2012.

[58] D. Rugar, H. J. Mamin, P. Guethner, S. E. Lambert, J. E. Stern, I. McFadyen, and T. Yogi. Magnetic force microscopy: General principles and application to longitudinal recording media. *Journal of Applied Physics*, 68(3):1169–1183, 1990.

[59] Y. Martin and H. Kumar Wickramasinghe. Magnetic imaging by "force microscopy" with 1000 å resolution. *Applied Physics Letters*, 50(20):1455–1457, 1987.

[60] C. Mathew Mate, Gary M. McClelland, Ragnar Erlandsson, and Shirley Chiang. Atomic-scale friction of a tungsten tip on a graphite surface. In *Scanning Tunneling Microscopy*, pages 226–229. Springer, 1993.

[61] Jean-Paul Salvetat, Andrzej J. Kulik, Jean-Marc Bonard, G. Andrew, D. Briggs, Thomas Stöckli, Karine Metenier, Sylvie Bonnamy, Francois Beguin, Nancy A Burnham, and Lásló Forró. Elastic modulus of ordered and disordered multiwalled carbon nanotubes. *Advanced Materials*, 11(2):161–165, 1999.

[62] Martin Stolz, Roberto Raiteri, A. U. Daniels, Mark R. VanLandingham, Werner Baschong, and Ueli Aebi. Dynamic elastic modulus of porcine articular cartilage determined at two different levels of tissue organization by indentation-type atomic force microscopy. *Biophysical Journal*, 86(5):3269, 2004.

[63] Stéphane Cuenot, Sophie Demoustier-Champagne, and Bernard Nysten. Elastic modulus of polypyrrole nanotubes. *Physical Review Letters*, 85(8):1690–1693, 2000.

[64] Joseph A. Stroscio and D. M. Eigler. Atomic and molecular manipulation with the scanning tunneling microscope. *Science*, 254(5036):1319–1326, 1991.

[65] Francesca Moresco, Gerhard Meyer, Karl-Heinz Rieder, Hao Tang, André Gourdon, and Christian Joachim. Conformational changes of single molecules induced by scanning tunneling microscopy manipula-

tion: A route to molecular switching. *Phys. Rev. Lett.*, 86:672–675, Jan 2001.

[66] Francesca Moresco. Manipulation of large molecules by low-temperature stm: model systems for molecular electronics. *Physics Reports*, 399(4):175–225, 2004.

[67] T. C. Shen, C. Wang, G. C. Abeln, J. R. Tucker, J. W. Lyding, Ph. Avouris, and R. E. Walkup. Atomic-scale desorption through electronic and vibrational excitation mechanisms. *Science*, 268(5217):1590–1592, 1995.

[68] L. Zhang, T. Sakai, N. Sakuma, T. Ono, and K. Nakayama. Nanostructural conductivity and surface-potential study of low-field-emission carbon films with conductive scanning probe microscopy. *Applied Physics Letters*, 75(22):3527–3529, 1999.

[69] J. M. R. Weaver and David W. Abraham. High resolution atomic force microscopy potentiometry. *Journal of Vacuum Science & Technology B: Microelectronics and Nanometer Structures*, 9(3):1559–1561, 1991.

[70] U. Hartmann. Magnetic force microscopy: Some remarks from the micromagnetic point of view. *Journal of Applied Physics*, 64(3):1561–1564, 1988.

[71] S. R. Higgins and R. J. Hamers. Morphology and dissolution processes of metal sulfide minerals observed with the electrochemical scanning tunneling microscope. volume 14, pages 1360–1364. AVS, 1996.

[72] M. Nonnenmacher, M. P. O'Boyle, and H. K. Wickramasinghe. Kelvin probe force microscopy. *Applied Physics Letters*, 58(25):2921–2923, 1991.

[73] R. Wiesendanger and M. Bode. Nano- and atomic-scale magnetism studied by spin-polarized scanning tunneling microscopy and spectroscopy. *Solid State Communications*, 119:341–355, 2001.

[74] E. Betzig, J. K. Trautman, T. D. Harris, J. S. Weiner, and R. L. Kostelak. Breaking the diffraction barrier: Optical microscopy on a nanometric scale. *Science*, 251(5000):1468–1470, 1991.

[75] Eric Betzig and Robert J. Chichester. Single molecules observed by near-field scanning optical microscopy. *Science*, 262(5138):1422–1425, 1993.

[76] D. M. Lewis, J. E. D. Spencer, and B. O. Field. An introduction to inelastic electron tunneling spectroscopy (iets) and its chemical applications. *Spectrochimica Acta Part A: Molecular Spectroscopy*, 44(3):247–261, 1988.

[77] Elena Bailo and Volker Deckert. Tip-enhanced raman scattering. *Chemical Society Reviews*, 37(5):921–930, 2008.

[78] R. Berndt, R. Gaisch, J. K. Gimzewski, B. Reihl, R. R. Schlittler, W. D. Schneider, M Tschudy, et al. Photon emission at molecular resolution induced by a scanning tunneling microscope. *Science*, 262:1425–1425, 1993.

[79] Leo Gross, Fabian Mohn, Nikolaj Moll, Gerhard Meyer, Rainer Ebel, Wael M. Abdel-Mageed, and Marcel Jaspars. Organic structure determination using atomic-resolution scanning probe microscopy. *Nature chemistry*, 2(10):821–825, 2010.

[80] R. Temirov, S. Soubatch, O. Neucheva, A. C. Lassise, and F. S. Tautz. A novel method achieving ultra-high geometrical resolution in scanning tunnelling microscopy. *New Journal of Physics*, 10(5):053012, 2008.

[81] G. Binnig, H. Rohrer, Ch. Gerber, and E. Weibel. Tunneling through a controllable vacuum gap. *Applied Physics Letters*, 40(2):178–180, 1982.

[82] Johannes A. A. W. Elemans, Inge De Cat, Hong Xu, and Steven De Feyter. Two-dimensional chirality at liquid-solid interfaces. *Chem. Soc. Rev.*, 38:722–736, 2009.

[83] Johannes A.A.W. Elemans. A new look at the chemical reaction. *Materials Today*, 12(7–8):34–38, 2009.

[84] Jürgen P. Rabe and Stefan Buchholz. Direct observation of molecular structure and dynamics at the interface between a solid wall and an organic solution by scanning tunneling microscopy. *Phys. Rev. Lett.*, 66:2096–2099, Apr 1991.

[85] P. Kowalczyk. High temperature stm/sts investigations of resonant image states on au (111). *Applied surface science*, 253(8):4036–4040, 2007.

[86] C.T. Herbschleb, S.C. Bobaru, and J.W.M. Frenken. High-pressure stm study of no reduction by co on pt(100). *Catalysis Today*, 154(1–2):61 – 67, 2010. ¡ce:title¿Catalytic Surface Science¡/ce:title¿.

[87] L. Bartels, S. Zöphel, G. Meyer, E. Henze, and K.-H. Rieder. Dimer formation and surface alloying: a stm study of lead on cu(211). *Surface Science*, 372(1–3):L261–L265, 1997.

[88] M. Kugler, Ch. Renner, V. Mikheev, G. Batey, and Ø. Fischer. A 3he cooled scanning tunneling microscope in uhv and high fields. *Physica B: Condensed Matter*, 280(1–4):551–552, 2000.

[89] John Bardeen. Tunnelling from a many-particle point of view. *Phys. Rev. Letters*, 6, 1961.

[90] J. Tersoff and D. R. Hamann. Theory and application for the scanning tunneling microscope. *Phys. Rev. Lett.*, 50:1998–2001, Jun 1983.

[91] J. Tersoff and D. R. Hamann. Theory of the scanning tunneling microscope. *Phys. Rev. B*, 31:805–813, Jan 1985.

[92] C.J. Chen. *Introduction to scanning tunneling microscopy*. Monographs on the physics and chemistry of materials. Oxford University Press, 2008.

[93] Leo Gross, Nikolaj Moll, Fabian Mohn, Alessandro Curioni, Gerhard Meyer, Felix Hanke, and Mats Persson. High-resolution molecular orbital imaging using a *p*-wave stm tip. *Phys. Rev. Lett.*, 107:086101, Aug 2011.

[94] B. N. J. Persson and A. Baratoff. Inelastic electron tunneling from a metal tip: The contribution from resonant processes. *Phys. Rev. Lett.*, 59:339–342, Jul 1987.

[95] D.M. Lewis, J.E.D. Spencer, and B.O. Field. An introduction to inelastic electron tunneling spectroscopy (iets) and its chemical applications. *Spectrochimica Acta Part A: Molecular Spectroscopy*, 44(3):247–261, 1988.

[96] J. Lambe and R. C. Jaklevic. Molecular vibration spectra by inelastic electron tunneling. *Phys. Rev.*, 165:821–832, Jan 1968.

[97] Chi Chen, Ping Chu, C. A. Bobisch, D. L. Mills, and W. Ho. Viewing the interior of a single molecule: Vibronically resolved photon imaging at submolecular resolution. *Phys. Rev. Lett.*, 105:217402, Nov 2010.

[98] Paolo Samorì. *Scanning probe microscopies beyond imaging*. Wiley-VCH, 2006.

[99] Nicolas Lorente and M Persson. Theory of single molecule vibrational spectroscopy and microscopy. *Physical review letters*, 85(14):2997–3000, 2000.

[100] B. Bhushan. *Handbook of Micro/Nano Tribology, Second Edition*. The Mechanics and materials science series. Taylor & Francis, 2010.

[101] Nancy A Burnham, Dawn D Dominguez, Robert L Mowery, and Richard J Colton. Probing the surface forces of monolayer films with an atomic-force microscope. *Physical review letters*, 64(16):1931–1934, 1990.

[102] O. Marti, B. Drake, and P. K. Hansma. Atomic force microscopy of liquid-covered surfaces: Atomic resolution images. *Applied Physics Letters*, 51(7):484–486, 1987.

[103] B. Drake, C. B. Prater, A. L. Weisenhorn, S. A. C. Gould, T. R. Albrecht, C. F. Quate, D. S. Cannell, H. G. Hansma, and P. K. Hansma. Imaging crystals, polymers, and processes in water with the atomic force microscope. *Science*, 243(4898):1586–1589, 1989.

[104] M. Binggeli, R. Christoph, H.-E. Hintermann, J. Colchero, and O. Marti. Friction force measurements on potential controlled graphite in an electrolytic environment. *Nanotechnology*, 4(2):59, 1993.

[105] Gerhard Meyer and Nabil M. Amer. Novel optical approach to atomic force microscopy. *Applied Physics Letters*, 53(12):1045–1047, 1988.

[106] J. H. Coombs and J. B. Pethica. Properties of vacuum tunneling currents: Anomalous barrier heights. *j-IBM-JRD*, 30(5):455–459, September 1986.

[107] M. D. Kirk, T. R. Albrecht, and C. F. Quate. Low-temperature atomic force microscopy. *Review of scientific instruments*, 59(6):833–835, 1988.

[108] Giessibl Franz J. Giessibl, Ch. Gerber, and Gerd Binnig. A low-temperature atomic force/scanning tunneling microscope for ultrahigh vacuum. *Journal of Vacuum Science & Technology B: Microelectronics and Nanometer Structures*, 9(2):984–988, 1991.

[109] T. R. Albrecht, P. Grütter, D. Rugar, and D. P. E. Smith. Low-temperature force microscope with all-fiber interferometer. *Ultramicroscopy*, 42:1638–1646, 1992.

[110] Charlotte Basire and Dimitri A. Ivanov. Evolution of the lamellar structure during crystallization of a semicrystalline-amorphous poly-

mer blend: time-resolved hot-stage spm study. *Physical review letters*, 85(26):5587–5590, 2000.

[111] Huiwen Liu and Bharat Bhushan. Investigation of nanotribological properties of self-assembled monolayers with alkyl and biphenyl spacer chains. *Ultramicroscopy*, 91(1):185–202, 2002.

[112] T. R. Albrecht, P. Grütter, D. Horne, and D. Rugar. Frequency modulation detection using high-q cantilevers for enhanced force microscope sensitivity. *Journal of Applied Physics*, 69(2):668–673, 1991.

[113] John E. Sader and Suzanne P. Jarvis. Accurate formulas for interaction force and energy in frequency modulation force spectroscopy. *Applied Physics Letters*, 84(10):1801, 2004.

[114] Franz J. Giessibl. Advances in atomic force microscopy. *Rev. Mod. Phys.*, 75:949–983, Jul 2003.

[115] Franz J. Giessibl. High-speed force sensor for force microscopy and profilometry utilizing a quartz tuning fork. *Applied Physics Letters*, 73(26):3956–3958, 1998.

[116] F. J. Giessibl. *Principles and Applications of the qPlus Sensor*, page 121. 2009.

[117] John E. Sader and Yoshiaki Sugimoto. Accurate formula for conversion of tunneling current in dynamic atomic force spectroscopy. *Applied Physics Letters*, 97(4):043502, 2010.

[118] C. Weiss, C. Wagner, C. Kleimann, M. Rohlfing, F. S. Tautz, and R. Temirov. Imaging pauli repulsion in scanning tunneling microscopy. *Phys. Rev. Lett.*, 105:086103, Aug 2010.

[119] Christian Weiss. *STM beyond vacuum tunnelling: scanning tunnelling hydrogen microscopy as a route to ultra-high resolution*. Universitätsbibliothek, 2012.

[120] Yu. G. Ptushinskiĭ. Low-temperature adsorption of gases on metal surfaces (review). *Low Temperature Physics*, 30(1):1–26, 2004.

[121] S. Duhm, A. Gerlach, I. Salzmann, B. Broker, R.L. Johnson, F. Schreiber, and N. Koch. Ptcda on au(111), ag(111) and cu(111): Correlation of interface charge transfer to bonding distance. *Organic Electronics*, 9:111–118, 2008.

[122] Nicoleta Nicoara, Elisa Román, José M Gómez-Rodríguez, José A Martín-Gago, and Javier Méndez. Scanning tunneling and photoemis-

sion spectroscopies at the ptcda/au (111) interface. *Organic electronics*, 7(5):287–294, 2006.

[123] P. Fenter, F. Schreiber, L. Zhou, P. Eisenberger, and S. R. Forrest. In situ studies of morphology, strain, and growth modes of a molecular organic thin film. *Physical Review B*, 56(6):3046, 1997.

[124] T. Schmitz-Hübsch, T. Fritz, F. Sellam, R. Staub, and K. Leo. Epitaxial growth of 3, 4, 9, 10-perylene-tetracarboxylic-dianhydride on au (111): A stm and rheed study. *Physical Review B*, 55(12):7972, 1997.

[125] F. S. Tautz, S. Sloboshanin, V. Shklover, R. Scholz, M. Sokolowski, J. A. Schaefer, and E. Umbach. Substrate influence on the ordering of organic submonolayers: a comparative study of ptcda on ag (110) and ag (111) using hreels. *Applied surface science*, 166(1):363–369, 2000.

[126] F. S. Tautz, S. Sloboshanin, J. A. Schaefer, R. Scholz, V. Shklover, M. Sokolowski, and E. Umbach. Vibrational properties of ultrathin ptcda films on ag (110). *Physical Review B*, 61(24):16933, 2000.

[127] V. Shklover, F. S. Tautz, R. Scholz, S. Sloboshanin, M. Sokolowski, J. A. Schaefer, and E. Umbach. Differences in vibronic and electronic excitations of ptcda on ag (111) and ag (110). *Surface science*, 454:60–66, 2000.

[128] F. S. Tautz, M. Eremtchenko, J. A. Schaefer, M. Sokolowski, V. Shklover, and E. Umbach. Strong electron-phonon coupling at a metal/organic interface: Ptcda/ag (111). *Physical Review B*, 65(12):125405, 2002.

[129] K. Glöckler, C. Seidel, A. Soukopp, M. Sokolowski, E. Umbach, M. Böhringer, R Berndt, and W-D Schneider. Highly ordered structures and submolecular scanning tunnelling microscopy contrast of ptcda and dm-pbdci monolayers on ag (111) and ag (110). *Surface science*, 405(1):1–20, 1998.

[130] J. V. Barth, H. Brune, G. Ertl, and R. J. Behm. Scanning tunneling microscopy observations on the reconstructed au(111) surface: Atomic structure, long-range superstructure, rotational domains, and surface defects. *Phys. Rev. B*, 42:9307–9318, Nov 1990.

[131] I. Chizhov, A. Kahn, and G. Scoles. Initial growth of 3, 4, 9, 10-perylenetetracarboxylic-dianhydride (ptcda) on au (111): a scanning tunneling microscopy study. *Journal of crystal growth*, 208(1):449–458, 2000.

[132] S. R. Forrest and Y. Zhang. Ultrahigh-vacuum quasiepitaxial growth of model van der waals thin films. i. theory. *Phys. Rev. B*, 49:11297–11308, Apr 1994.

[133] L. Kilian, E. Umbach, and M. Sokolowski. A refined structural analysis of the ptcda monolayer on the reconstructed au (111) surface – "rigid or distorted carpet?". *Surface science*, 600(13):2633–2643, 2006.

[134] S. Mannsfeld, M. Toerker, T. Schmitz-Hübsch, F. Sellam, T. Fritz, and K. Leo. Combined {LEED} and {STM} study of {PTCDA} growth on reconstructed au(111) and au(100) single crystals. *Organic Electronics*, 2(3–4):121–134, 2001.

[135] Michael Rohlfing, Ruslan Temirov, and Frank Stefan Tautz. Adsorption structure and scanning tunneling data of a prototype organic-inorganic interface: Ptcda on ag(111). *Phys. Rev. B*, 76:115421, Sep 2007.

[136] D. M. Eigler and E. K. Schweizer. Positioning single atoms with a scanning tunnelling microscope. *Nature*, 344:524–526, April 1990.

[137] D. M. Eigler, P. S. Weiss, E. K. Schweizer, and N. D. Lang. Imaging xe with a low-temperature scanning tunneling microscope. *Phys. Rev. Lett.*, 66:1189–1192, Mar 1991.

[138] N. D. Lang. Theory of single-atom imaging in the scanning tunneling microscope. *Phys. Rev. Lett.*, 56:1164–1167, Mar 1986.

[139] Ali Yazdani, D. M. Eigler, and N. D. Lang. Off-resonance conduction through atomic wires. *Science*, 272(5270):1921–1924, 1996.

[140] N. D. Lang. Density-functional studies of metal surfaces and metal-adsorbate systems. *Surface science*, 299:284–297, 1994.

[141] L. A. Zotti, M. Bürkle, Y. J. Dappe, F. Pauly, and J. C. Cuevas. Electronic transport through single noble gas atoms. *Phys. Rev. B*, 84:193404, Nov 2011.

[142] Christian Weiss, Christian Wagner, Ruslan Temirov, and F. S. Tautz. Direct imaging of intermolecular bonds in scanning tunneling microscopy. *Journal of the American Chemical Society*, 132(34):11864–11865, 2010.

[143] Shiwu Gao, M. Persson, and B. I. Lundqvist. Theory of atom transfer with a scanning tunneling microscope. *Phys. Rev. B*, 55:4825–4836, Feb 1997.

[144] M. Böhringer, W.-D. Schneider, K. Glöckler, E. Umbach, and R. Berndt. Adsorption site determination of ptcda on ag (110) by manipulation of adatoms. *Surface science*, 419(1):L95–L99, 1998.

[145] C. Seidel, C. Awater, X. D. Liu, R. Ellerbrake, and H. Fuchs. A combined stm, leed and molecular modelling study of ptcda grown on ag (110). *Surface science*, 371(1):123–130, 1997.

[146] C. Seidel, J. Poppensieker, and H. Fuchs. Real-time monitoring of phase transitions of vacuum deposited organic films by molecular beam deposition leed. *Surface science*, 408(1):223–231, 1998.

[147] Afshin Abbasi and Reinhard Scholz. Ab initio calculation of the dispersion interaction between a polyaromatic molecule and a noble metal substrate: Ptcda on ag(110). *The Journal of Physical Chemistry C*, 113(46):19897–19904, 2009.

[148] M. Wiessner, J. Ziroff, F. Forster, M. Arita, K. Shimada, P. Puschnig, A. Schöll, and F. Reinert. Substrate-mediated band-dispersion of adsorbate molecular states. *Nat Commun*, 4:1514–, 2 2013.

[149] Leo Gross, Fabian Mohn, Nikolaj Moll, Peter Liljeroth, and Gerhard Meyer. The chemical structure of a molecule resolved by atomic force microscopy. *Science*, 325(5944):1110–1114, 2009.

[150] Dimas G. de Oteyza, Patrick Gorman, Yen-Chia Chen, Sebastian Wickenburg, Alexander Riss, Duncan J. Mowbray, Grisha Etkin, Zahra Pedramrazi, Hsin-Zon Tsai, Angel Rubio, Michael F. Crommie, and Felix R. Fischer. Direct imaging of covalent bond structure in single-molecule chemical reactions. *Science*, 340(6139):1434–1437, 2013.

[151] L. Bartels, G. Meyer, and K.-H. Rieder. Controlled vertical manipulation of single co molecules with the scanning tunneling microscope: A route to chemical contrast. *Applied Physics Letters*, 71(2):213–215, 1997.

[152] L. Bartels, G. Meyer, K.-H. Rieder, D. Velic, E. Knoesel, A. Hotzel, M. Wolf, and G. Ertl. Dynamics of electron-induced manipulation of individual co molecules on cu(111). *Phys. Rev. Lett.*, 80:2004–2007, Mar 1998.

[153] Zhixiang Sun, Mark P. Boneschanscher, Ingmar Swart, Daniël Vanmaekelbergh, and Peter Liljeroth. Quantitative atomic force microscopy with carbon monoxide terminated tips. *Phys. Rev. Lett.*, 106:046104, Jan 2011.

[154] Saw-Wai Hla and Karl-Heinz Rieder. Stm control of chemical reactions: Single-molecule synthesis. *Annual review of physical chemistry*, 54(1):307–330, 2003.

[155] Leo Gross, Fabian Mohn, Nikolaj Moll, Bruno Schuler, Alejandro Criado, Enrique Guitián, Diego Peña, André Gourdon, and Gerhard Meyer. Bond-order discrimination by atomic force microscopy. *Science*, 337(6100):1326–1329, 2012.

[156] J. M. Gottfried, K. J. Schmidt, S. L. M. Schroeder, and K. Christmann. Adsorption of carbon monoxide on au (1 1 0)-(1× 2). *Surface science*, 536(1-3):206–224, 2003.

[157] Linda A. Bruce and Margaret H. Sheridan. Adsorption of xenon on films of gold, aluminium and silver. *J. Chem. Soc., Faraday Trans. 1*, 68:997–1009, 1972.

[158] Joachim Welker and Franz J. Giessibl. Revealing the angular symmetry of chemical bonds by atomic force microscopy. *Science*, 336(6080):444–449, 2012.

[159] Nikolaj Moll, Leo Gross, Fabian Mohn, Alessandro Curioni, and Gerhard Meyer. A simple model of molecular imaging with noncontact atomic force microscopy. *New Journal of Physics*, 14(8):083023, 2012.

[160] Georg Hermann Simon, Markus Heyde, and Hans-Peter Rust. Recipes for cantilever parameter determination in dynamic force spectroscopy: spring constant and amplitude. *Nanotechnology*, 18(25):255503, 2007.

[161] Markus Ternes, Christopher P. Lutz, Cyrus F. Hirjibehedin, Franz J. Giessibl, and Andreas J. Heinrich. The force needed to move an atom on a surface. *Science*, 319(5866):1066–1069, 2008.

[162] Martin Ondráífmmode čelse čfiek, Pablo Pou, Vít Rozsíval, Cesar González, Pavel Jelínek, and Rubén Pérez. Forces and currents in carbon nanostructures: Are we imaging atoms? *Phys. Rev. Lett.*, 106:176101, Apr 2011.

[163] C. Toher, R. Temirov, A. Greuling, F. Pump, M. Kaczmarski, G. Cuniberti, M. Rohlfing, and F. S. Tautz. Electrical transport through a mechanically gated molecular wire. *Phys. Rev. B*, 83:155402, Apr 2011.

[164] Georgy Kichin, Christian Weiss, Christian Wagner, F. Stefan Tautz, and Ruslan Temirov. Single molecule and single atom sensors for atomic resolution imaging of chemically complex surfaces. *Journal of the American Chemical Society*, 133(42):16847–16851, 2011.

[165] M. Mirnezhad, R. Ansari, M. Seifi, H. Rouhi, and M. Faghihnasiri. Mechanical properties of graphene under molecular hydrogen physisorption: An ab initio study. *Solid State Communications*, 152(10):842–845, 2012.

[166] Geunseop Lee and E. W. Plummer. Interaction of hydrogen with the ag(111) surface. *Phys. Rev. B*, 51:7250–7261, Mar 1995.

[167] X. -. Zhou, J. M. White, and B. E. Koel. Chemisorption of atomic hydrogen on clean and cl-covered ag(111). *Surface Science*, 218(1):201–210, 1989. Cited By (since 1996): 43.

[168] H. Iwai, K. Fukutani, and Y. Murata. Behavior of atomic hydrogen on au(001). *Surface Science*, 357-358:663–666, 1996. Cited By (since 1996): 6.

[169] A. G. Sault, R. J. Madix, and C. T. Campbell. Adsorption of oxygen and hydrogen on au(110)-(1 × 2). *Surface Science*, 169(2-3):347–356, 1986. Cited By (since 1996): 139.

[170] M. van der Maas, S. Vasnyov, B. L. M. Hendriksen, O. I. Shklyarevskii, and S. Speller. Electron scattering effects at physisorbed hydrogen molecules on break-junction electrodes and nanowires formation in hydrogen environment. *Low Temperature Physics*, 38(6):517–522, 2012.

[171] B. C. Stipe, M. A. Rezaei, and W. Ho. Inducing and viewing the rotational motion of a single molecule. *Science*, 279(5358):1907–1909, 1998.

[172] B. C. Stipe, M. A. Rezaei, and W. Ho. Coupling of vibrational excitation to the rotational motion of a single adsorbed molecule. *Phys. Rev. Lett.*, 81:1263–1266, Aug 1998.

[173] T. Komeda, Y. Kim, Maki Kawai, B. N. J. Persson, and H. Ueba. Lateral hopping of molecules induced by excitation of internal vibration mode. *Science*, 295(5562):2055–2058, 2002.

[174] A. Halbritter, P. Makk, Sz. Csonka, and G. Mihály. Huge negative differential conductance in $au - h_2$ molecular nanojunctions. *Phys. Rev. B*, 77(7):075402, Feb 2008.

[175] P. Makk, Sz. Csonka, and A. Halbritter. Effect of hydrogen molecules on the electronic transport through atomic-sized metallic junctions in the superconducting state. *Phys. Rev. B*, 78:045414, Jul 2008.

[176] Sz. Csonka, A. Halbritter, and G. Mihály. Pulling gold nanowires with a hydrogen clamp: Strong interactions of hydrogen molecules with gold nanojunctions. *Phys. Rev. B*, 73:075405, Feb 2006.

[177] J. Gaudioso, L. J. Lauhon, and W. Ho. Vibrationally mediated negative differential resistance in a single molecule. *Phys. Rev. Lett.*, 85:1918–1921, Aug 2000.

[178] W. Thijssen, D. Djukic, a. Otte, R. Bremmer, and J. van Ruitenbeek. Vibrationally induced two-level systems in single-molecule junctions. *Physical Review Letters*, 97(22):226806, December 2006.

[179] D. Djukic, K. S. Thygesen, C. Untiedt, R. H. M. Smit, K. W. Jacobsen, and J. M. van Ruitenbeek. Stretching dependence of the vibration modes of a single-molecule $Pt-h_2-Pt$ bridge. *Phys. Rev. B*, 71:161402, Apr 2005.

[180] J. A. Gupta, C. P. Lutz, A. J. Heinrich, and D. M. Eigler. Strongly coverage-dependent excitations of adsorbed molecular hydrogen. *Phys. Rev. B*, 71:115416, Mar 2005.

[181] Isaac F. Silvera. The solid molecular hydrogens in the condensed phase: Fundamentals and static properties. *Rev. Mod. Phys.*, 52:393–452, Apr 1980.

[182] D. Y. Sun, J. W. Liu, X. G. Gong, and Zhi-Feng Liu. Empirical potential for the interaction between molecular hydrogen and graphite. *Phys. Rev. B*, 75:075424, Feb 2007.

[183] J. S. Arellano, L. M. Molina, A. Rubio, and J. A. Alonso. Density functional study of adsorption of molecular hydrogen on graphene layers. *The Journal of Chemical Physics*, 112(18):8114–8119, 2000.

[184] Matteo Bonfanti, Rocco Martinazzo, Gian Franco Tantardini, and Alessandro Ponti. Physisorption and diffusion of hydrogen atoms on graphite from correlated calculations on the h-coronene model system. *The Journal of Physical Chemistry C*, 111(16):5825–5829, 2007.

[185] M. C. Gordillo and J. Boronat. Second layer of h_2 and d_2 adsorbed on graphene. *Phys. Rev. B*, 87:165403, Apr 2013.

[186] M. C. Gordillo and J. Boronat. Phase diagram of h_2 adsorbed on graphene. *Phys. Rev. B*, 81:155435, Apr 2010.

[187] C. Carbonell-Coronado and M. C. Gordillo. Phase diagram of d_2 adsorbed on graphene and graphite. *Phys. Rev. B*, 85:155427, Apr 2012.

[188] Robert N. Barnett, Hannu Häkkinen, Andrew G. Scherbakov, and Uzi Landman. Hydrogen welding and hydrogen switches in a monatomic gold nanowire. *Nano Letters*, 4(10):1845–1852, 2004.

[189] V. Shklover, S. Schmitt, E. Umbach, F.S. Tautz, M. Eremtchenko, Y. Shostak, J.A. Schaefer, and M. Sokolowski. Strong k-induced changes in perylene-tetracarboxylic-dianhydride films on ag(110) studied by hreels and leed. *Surface Science*, 482–485, Part 2(0):1241–1248, 2001.

[190] Dimas G. de Oteyza, Patrick Gorman, Yen-Chia Chen, Sebastian Wickenburg, Alexander Riss, Duncan J Mowbray, Grisha Etkin, Zahra Pedramrazi, Hsin-Zon Tsai, Angel Rubio, et al. Direct imaging of covalent bond structure in single-molecule chemical reactions. *Science (New York, NY)*, 2013.

Acknowledgement

Publications

1. **Single Molecule and Single Atom Sensors for Atomic Resolution Imaging of Chemically Complex Surfaces**.
   G. Kichin, C. Weiss, C. Wagner, F. S. Tautz, R. Temirov.
   Journal of the American Chemical Society, 2011

2. **Mit atomaren Sensoren Moleküle erkennen**.
   G. Kichin, R. Temirov, C. Wagner, F. S. Tautz.
   Nachrichten aus der Chemie, 2012

3. **Calibrating atomic-scale force sensors installed at the tip apex of the scanning tunneling microscope**.
   G. Kichin, C. Wagner, F. S. Tautz, R. Temirov.
   Physical Review B, 2013

4. **Commensurate Registry and Chemisorption at a Hetero-organic Interface**.
   B. Stadtmüller, T. Sueyoshi, **G. Kichin**, I. Kröger, S. Soubatch, R. Temirov, F. S. Tautz, C. Kumpf.
   Physical Review Letters, 2012

Conference contributions

1. Local surface spectroscopy with STHM junction.
   G. Kichin, C. Weiss, C. Wagner, F. S. Tautz, R. Temirov.
   Poster presentation.
   DPG (Deutsche Physikalische Gesellschaft), Dresden, Germany, April 2011.

2. Local surface spectroscopy with STHM junction.
   G. Kichin, C. Weiss, C. Wagner, F. S. Tautz, R. Temirov.
   Poster presentation.
   ELECMOL, Grenoble, France, December 2010.

3. Single-atom sensors for high resolution force imaging.
   G. Kichin, C. Weiss, C. Wagner, F. S. Tautz, R. Temirov.
   Poster presentation.
   ESPMI IV, Karlsruhe, Germany, September 2011.

4. Single molecule and single-atom sensors for Atomic Resolution.
   G. Kichin, C. Wagner, F. S. Tautz, R. Temirov.

Oral presentation.
DPG (Deutsche Physikalische Gesellschaft), Berlin, Germany, March 2012.

5. STM tip modification for high resolution force imaging.
   G. Kichin, C. Weiss, C. Wagner, F. S. Tautz, R. Temirov.
   Poster presentation.
   WE-Heraeus-Seminar on Latest Developments in Scanning Probe Techniques focused on Nanotechnology, Bad Honnef, Germany, November 2011.

6. New type of surface investigation using scanning tunneling microscope with tip decorated with H_2 or D_2.
   G. Kichin, C. Wagner, F. S. Tautz, R. Temirov.
   Poster presentation.
   Workshop on controlled Atomic Dynamics on Solid Surfaces: Atom and Molecular Manipulation, Donostia-San Sebastian, Spain, May 2013.

7. Mapping the surface adsorption potential with the scanning tunneling microscope.
   G. Kichin, C. Wagner, F. S. Tautz, R. Temirov.
   Oral presentation.
   DPG (Deutsche Physikalische Gesellschaft), Regensburg, Germany, February 2013.

Curriculum Vitae

Georgy Kichin
born on November 14th, 1985 in Moscow, Russia.
Nationality: Russian.

Education:

1999–2003: Physics and Mathematics Lyceum, Moscow, Russia.

2003–2007: BSc study at Faculty of Problems of Physics and Power Engineering, Moscow Institute of Physics and Technology (State University), Moscow, Russia.

2007: BSc degree with honours in applied mathematics and applied physics. BSc thesis title: "Study of the losses in the metal-dielectric photonic crystals with S-matrix method". Scientific adviser S.G. Tikhodeev.

2007–2009: MSc study at Faculty of Problems of Physics and Power Engineering, Moscow Institute of Physics and Technology (State University), Moscow, Russia.

2009: MSc degree with honours in applied mathematics and applied physics. MSc thesis title: "Optical properties of complex metal-dielectric photonic crystal structures". Scientific adviser S.G. Tikhodeev.

2009–2010: researcher in Prokhorov General Physics Institute, Russian Academy of Sciences, Moscow, Russia.

2010–2014: PhD student at Peter Grünberg Institute 3, Forschungszentrum Jülich. PhD thesis title "Submolecular imaging with atomic force sensor from single molecule or atom". Scientific adviser S.F. Tautz.

Band / Volume 75
Aberrationskorrigierte Photoemissionsmikroskopie an magnetischen Systemen: Von statischer Charakterisierung zu zeitaufgelöster Abbildung
F. Nickel (2013), x, 99 pp
ISBN: 978-3-89336-913-3

Band / Volume 76
Temperature-Induced Metamagnetic Transition and Domain Structures of Single-Crystalline FeRh Thin Films on MgO(100)
X. Zhou (2013), xi, 104 pp
ISBN: 978-3-89336-919-5

Band / Volume 77
Interplay between Magnetism and Superconductivity in Iron Based High Temperature Superconductors
S. Price (2013), 196 pp
ISBN: 978-3-89336-921-8

Band / Volume 78
Magnetoresistance and transport in carbon nanotube-based devices
C. Morgan (2013), viii, 131 pp
ISBN: 978-3-89336-926-3

Band / Volume 79
Development of a relativistic full-potential first-principles multiple scattering Green function method applied to complex magnetic textures of nano structures at surfaces
D. Bauer (2014), 193 pp
ISBN: 978-3-89336-934-8

Band / Volume 80
Identifizierung von artifiziellen Liganden eines in Nanodiscs inkorporierten integralen Membranproteins
M. Pavlidou (2014), 106 pp
ISBN: 978-3-89336-942-3

Band / Volume 81
Interdomain Functional Dynamics of Phosphoglycerate Kinase Studied by Single-Molecule FRET
M. Gabba (2014), v, 179 pp
ISBN: 978-3-89336-943-0

Band / Volume 82

Schriften des Forschungszentrums Jülich
Reihe Schlüsseltechnologien / Key Technologies

Weitere ***Schriften des Verlags im Forschungszentrum Jülich*** unter
http://wwwzb1.fz-juelich.de/verlagextern1/index.asp

JÜLICH
FORSCHUNGSZENTRUM